First double-differential cross-section measurements in proton multiplicity and kinematics for mesonless ν_μ charged-current interactions on argon using the MicroBooNE detector

MICROBOONE-NOTE-1135-PUB

The MicroBooNE Collaboration*

We present the first double-differential cross-section measurements of muon neutrino charged-current interactions on argon with no pions and one or more protons ($N_p \geq 1$) in the final state as a function of proton multiplicity and kinematics. The analysis uses the full Booster Neutrino Beam dataset collected by the MicroBooNE detector at Fermi National Accelerator Laboratory, corresponding to a total of 1.30×10^{21} protons on target. We measure the proton multiplicity as a function of the momenta and muon-proton opening angles of the leading and subleading protons, as well as the total kinetic energy of the hadronic system. The treatment of the statistical and systematic uncertainties includes correlations between the different distributions extracted. The measured cross sections are compared to predictions from several event generators using different primary and final-state interaction models. The results reveal strong sensitivity to the modeling of final-state interactions, and none of the generators tested provides a fully adequate description of the data. Significant disagreement between data and predictions is observed in the proton multiplicity distributions, particularly at backward opening angles and for subleading proton kinematics.

CONTENTS

* microboone_info@fnal.gov

I. INTRODUCTION

Accelerator-based neutrino experiments are poised to address several of the most significant open questions in neutrino physics in the near future. The Deep Underground Neutrino Experiment (DUNE) [1] aims to make precision measurements of neutrino oscillation parameters, including the determination of the neutrino mass ordering and the search for leptonic Charge-Parity (CP) violation [2, 3]. The Short-Baseline Neutrino (SBN) program [4] will investigate the short-baseline anomalies that may indicate the existence of sterile neutrino species [5, 6]. Both of these programs use liquid argon time projection chambers (LArTPCs) [7, 8] as their primary detector technology, which provide detailed imaging of neutrino interaction final states. The success of both experiments relies on the accurate modeling of neutrino-argon interactions, as the associated uncertainties are among the leading sources of systematic error in their analyses. Correct reconstruction of the hadronic system in neutrino interactions, in particular the number and kinematics of final-state protons, is essential for accurate neutrino energy estimation and event classification. However, these are notoriously challenging to predict, especially for subleading protons. Among the relevant interaction channels, charged-current muon neutrino scattering producing no mesons and one or more protons (denoted as CC0πNp) is one of the dominant topologies at neutrino energies around 1 GeV. The absence of pions in the final state makes this channel particularly well-suited for direct measurements of the proton kinematics.

The final-state proton multiplicity in CC0πNp events is determined by several physics processes. Different primary interaction mechanisms, such as quasi-elastic scattering (QE), resonance production (RES), and deep inelastic scattering (DIS), lead to different initial proton multiplicities. Multi-nucleon emission mechanisms, such as meson-exchange currents (MEC), lead to correlated nucleon knockouts. The initial multiplicities are further modified by final-state interactions (FSI), which govern how protons and other hadrons propagate through the nuclear medium. Differences in the modeling of these mechanisms across event generators can lead to significant discrepancies in predicted proton multiplicities. Previous measurements of this channel on argon have revealed tension between data and generator predictions, particularly when looking at correlations between kinematic distributions [9]. However, the measurements did not distinguish between different proton multiplicities, leaving the role of FSI and multi-nucleon processes in shaping the hadronic final state largely unexplored.

We present the first double-differential cross-section measurements of CC0πNp interactions on argon as a function of proton multiplicity and leading and subleading proton kinematics using the full MicroBooNE dataset of 1.30×10^{21} protons on target (POT) collected from the Booster Neutrino Beam (BNB) [10]. The analysis targets observables directly sensitive to proton production mechanisms, including the momenta and opening angles of up to and including the fourth-leading proton, as well as the total hadronic available energy. Compared to the previous MicroBooNE CC0πNp measurement [9], this work introduces proton multiplicity as the primary observable, uses less stringent requirements on the outgoing muon that result in higher selection efficiency, and benefits from nearly double the beam exposure. The unfolded cross sections are compared to predictions from several generators, including multiple FSI model variations within GENIE, to directly probe the sensitivity to the cascade treatment. These measurements provide a unique benchmark for testing and refining the modeling of final-state interactions and multi-nucleon processes in neutrino event generators, with direct relevance for the DUNE and SBN physics programs.

II. EXPERIMENTAL SETUP

A. Detector and beamline

The MicroBooNE detector [11] is a surface LArTPC that operated at Fermilab from 2015 to 2021. It is situated on-axis relative to the BNB [10] 463 m downstream of the target. The detector has a fiducial mass of 85 metric tons of liquid argon within its field cage. It is instrumented with a three-plane wire anode with a 3 mm pitch. Two induction planes are placed at an angle $\pm 60^\circ$ from the vertical, while a third collection plane is vertically oriented. Behind the wire planes, an array of photomultiplier tubes with fast timing resolution serves as the light collection system.

Neutrinos from the BNB are produced by colliding an 8 GeV proton beam with a beryllium target. The generated charged mesons are focused by means of a magnetic horn and subsequently decay in flight, producing neutrinos. After the decay region, a hadron absorber made of concrete and steel removes the undecayed particles. The flux at the

MicroBooNE detector is dominated by muon neutrinos, with a mean energy of 800 MeV. The beam also has a small muon antineutrino component, corresponding to 5.9% of the beam content, as well as a combined 0.6% of electron neutrinos and antineutrinos. Over the course of its operation, MicroBooNE collected data corresponding to 1.30×10^{21} POT from the BNB.

B. Simulation

Monte Carlo (MC) simulations are used in MicroBooNE to develop the event selection, efficiency estimation, background characterization, and systematic uncertainty evaluation.

The process starts with the BNB flux prediction [12], which is based on Geant4 beamline simulations [13–15] developed for the MiniBooNE experiment and adapted to the MicroBooNE location. Neutrino interactions in the MicroBooNE detector are simulated using the GENIE neutrino event generator [16], version 3.0.6. The baseline interaction model used is based on the `G18_10a_02_11a` configuration of GENIE. This model configuration is tuned to external CC0π data from the T2K experiment [17]. The simulated events are reweighted to adjust four cross-section model parameters not well constrained by theory or data, resulting in a model that agrees better with the MicroBooNE dataset. Further details on the GENIE MicroBooNE tune can be found in Ref. [18].

The events generated with GENIE according to the predicted BNB flux are propagated through the MicroBooNE detector geometry using Geant4 [13–15]. LArSoft [19] is the event-processing framework adopted by MicroBooNE for its readout simulation and reconstruction. A number of custom modules in LArSoft simulate the response of the electronics to the ionizing particles exiting the neutrino interaction. Effects such as light attenuation, electron diffusion, and electric field distortions caused by positive ions are included here [20–25].

All the generated MC samples employ an overlay technique, in which simulated neutrino events from GENIE are superimposed onto actual beam-off data samples taken when the BNB was not in operation [26]. This method ensures that event-by-event fluctuations in cosmic backgrounds and noise levels are realistically represented in the analysis. These beam-off samples are also used to estimate the rate of cosmic ray and other non-beam correlated backgrounds.

C. Reconstruction

The reconstruction paradigm used for this analysis is the Pandora multi-algorithm pattern-recognition toolkit [27, 28]. It uses topological and calorimetric information to reconstruct particles in the detector and identify neutrino interaction candidates. It aggregates the reconstructed hits from the waveforms in each of the wire planes into 2D clusters, which are then correlated across planes to form 3D particle candidates. These particles are grouped into slices, clusters of spatially and temporally correlated activity. Timing information is used to select neutrino candidates from coincidence with the BNB beam window.

The Pandora outputs include a reconstructed neutrino vertex and a particle hierarchy associated with it. Particles are assigned a track score that distinguishes shower-like from track-like objects. This is used to help reject background events containing electromagnetic showers, such as those from neutral pion decays. The reconstruction is complemented with additional algorithms for calorimetric calibration [29], a log-likelihood ratio particle identification (PID) score used to separate muons from protons [30], and muon momentum estimation based on multiple Coulomb scattering (MCS) [31].

III. ANALYSIS METHODS

A. Signal definition

This analysis focuses on muon neutrino interactions on argon producing one or more protons and no mesons in the final state. We require the momentum of the primary muon to be above 0.10 GeV/c. The momentum of the leading final-state proton must lie within the interval [0.25, 1.00] GeV/c. Subleading protons are considered detectable if their momentum is above the 0.25 GeV/c threshold.

These phase-space limits are applied to select regions with good signal purity and resolution. The muon threshold of 0.10 GeV/c is motivated by a 10.0 cm track length requirement for the efficient selection of muon candidates. The 0.25 GeV/c lower threshold for the proton follows selection efficiency and energy reconstruction bias considerations. The 1.00 GeV/c upper limit on the proton momentum ensures their reliable identification, as high-momentum protons tend to be misclassified as muon-like.

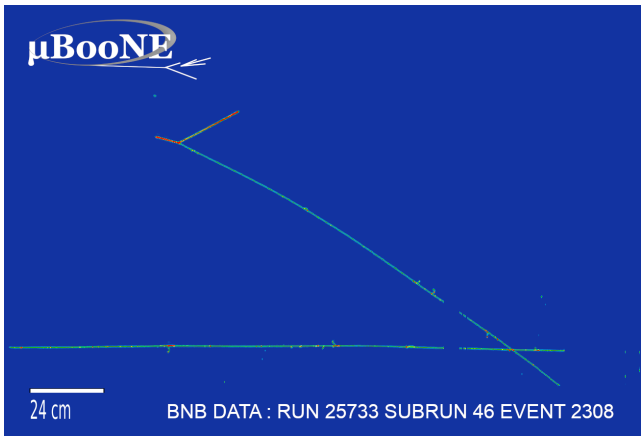

(a)

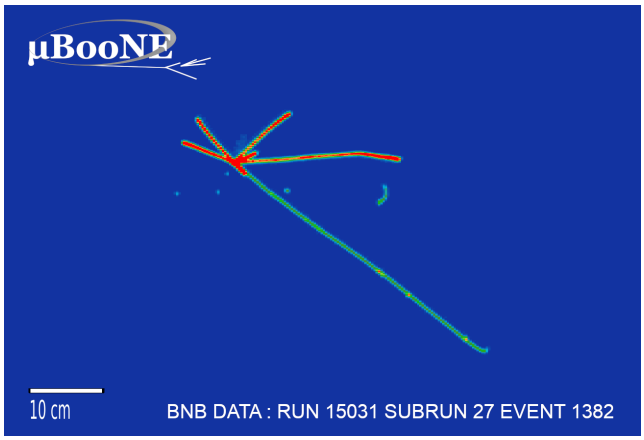

(b)

FIG. 1. Event displays for two selected events: (a) candidate event with 2 reconstructed protons, and (b) candidate event with 6 reconstructed protons.

The signal definition closely follows that of previous MicroBooNE CC0πNp analyses [9, 32]. However, since we do not report cross sections as a function of muon momentum, we accept events with exiting muons despite their reduced momentum resolution compared to contained ones. Therefore, an upper limit on muon momentum is not used.

In the following, simulated events are divided into different categories based on their generator-level information:

- **Signal**: Events satisfying all signal requirements, with a neutrino vertex contained within the fiducial volume (FV) defined in Sec. III B. Signal events are further subdivided either by their true topology (i.e., the number of protons within the momentum range [0.25, 1.00] GeV/c in the final state) into $1p$, $2p$, or Mp with $M \geq 3$, or by the primary interaction mode: QE, MEC, RES, or other. The last subcategory is dominated by DIS events.

- **Out FV**: Events with a true interaction vertex outside the FV. This category includes events from all different topologies which fail the FV cut.

- **ν_μ CC0π0p**: Muon neutrino charged-current interaction events with no leading proton within the required momentum limits. Events with no protons at all, or leading protons below or above the specified range, are included.

- **ν_μ CC$N\pi$**: Muon neutrino charged-current interaction events with any number of charged or neutral pions in the final state.

- **Other ν_μ CC**: Any other muon neutrino charged-current interaction events. This includes events containing mesons other than pions, or with a primary muon momentum below 0.10 GeV/c.

- **ν_e CC**: Electron neutrino charged-current interaction events.

- **NC**: Neutral-current neutrino or antineutrino interaction events.

- **Beam-off**: Background events induced by cosmic rays.

- **Other**: Any background events which do not fall into another category.

B. Event selection

The selection of signal events uses the products of the automated Pandora reconstruction framework. It consists of two main steps: an inclusive ν_μ CC preselection [33] and the specific CC0πNp selection part. The event selection strategy is shared with the previous CC0πNp analysis from Ref. [9]. However, because this analysis focuses on proton multiplicity and kinematics instead of muon-proton correlations, muon containment and quality cuts (the latter requiring agreement within 25% between range-based and MCS-based muon momentum estimates [9]) are not applied, consistent with the relaxed muon momentum requirements described in Sec. III A. This choice results in a significantly higher selection efficiency. The same selection criteria are applied to both data and simulated events.

The preselection tries to classify valid neutrino events through the identification of a primary muon candidate. First, the reconstructed neutrino vertex is required to be contained within the fiducial volume. The fiducial volume in the analysis is a rectangular prism, chosen in such a way that all of its sides are 21.5 cm inward of the active volume edges, except for the downstream z direction where this distance is increased to 70.0 cm. Next, all the primary neutrino interaction products are required to have their starting points inside a looser containment volume, 10.0 cm inward with respect to the active volume.

Additional cosmic rejection is achieved by applying a cut on the topological score, an event-level variable computed by a support-vector machine trained to classify neutrino interaction candidates as neutrino-like or cosmic-like [33]. Events with a topological score below 0.1 are rejected.

The final step in the preselection is identifying a viable muon candidate. This is achieved in four steps, starting from all the direct products of the neutrino interaction in the events passing the previous selection cuts. The following particle-level selection requirements are applied sequentially to identify the muon candidates:

1. The track score must be higher than 0.8 to reject shower-like particles.
2. Discard particles with a distance between the neutrino vertex and their start position greater than 4.0 cm.
3. Require a track length greater than 10.0 cm, excluding short tracks such as low-energy protons and cosmic rays.
4. Proton- and muon-like particles are separated by requiring the log-likelihood ratio PID score [30] to be greater than 0.2.

For each event, the particle passing all the selections and with the highest PID score is taken to be the muon candidate.

In order to isolate the desired topology, namely one or more protons and no mesons in the final state, a number of additional requirements are applied. To match the phase-space limit imposed on the signal definition, the reconstructed muon candidate momentum must be greater than 0.1 GeV/c. The muon momentum is estimated either from range or the MCS method, depending on whether the muon is contained or not.

Events containing shower-like particles are rejected by requiring all reconstructed particles to have a track score greater than 0.5, suppressing backgrounds from primary electrons and neutral pions. All particles passing this requirement, excluding the muon candidate, are considered proton candidates. At least one proton candidate must be present, and all proton candidate endpoints must lie within the containment volume defined above.

An additional log-likelihood ratio PID score cut is applied to the proton candidates. A value less than 0.2 allows for good acceptance of low-energy protons, which tend to have PID scores near zero. Finally, the leading proton candidate's momentum, estimated using a range-based kinetic energy reconstruction, must lie within the range [0.25, 1.00] GeV/c.

Events passing the inclusive ν_μ CC preselection and the additional selection criteria are taken to be CC0πNp candidates, the signal event category for this measurement.

TABLE I. Evolution of the number of selected events, efficiency, and purity as the selection criteria are applied to the simulation sample.

Selection cut	Events	Efficiency	Purity
No cuts	5365313	1.000	0.026
In FV	477172	0.789	0.230
Start points contained	437360	0.729	0.231
Topological cut	274544	0.654	0.330
ν_μ CC incl.	210832	0.591	0.389
μ phase-space limits	210793	0.591	0.389
No showers	157058	0.522	0.461
Has p candidate	126591	0.473	0.518
p contained	113051	0.449	0.552
p PID cut	73149	0.398	0.755
p phase-space limits	71342	0.393	0.764

Using this selection, we obtain a purity of 76.4% and a selection efficiency of 39.3%. A step-by-step summary of the number of selected events, the selection efficiency and purity achieved is presented in Table I. Figure 1 shows two signal candidate events selected from the MicroBooNE BNB dataset, with 2 and 6 reconstructed protons.

Compared to the previous MicroBooNE CC0πNp analysis from Ref. [9] the selection efficiency of 39.3% is significantly higher than the 12.3% obtained in that work, as a result of the more relaxed muon requirements described above. In addition, the present analysis benefits from the full MicroBooNE dataset of 1.30×10^{21} POT, compared to the 6.79×10^{20} POT used in the previous measurement.

C. Measurement strategy

We focus on observables related to the proton multiplicity and kinematics. The proton multiplicity is defined as the number of protons in the event with momentum above the 250 MeV/c threshold, consistent with the lower momentum threshold in the signal definition. For the kinematic variables, we study the magnitude of the momentum for the leading and subleading protons up to the 4th-leading, which we denote $p_{p_i} \equiv |\mathbf{p}_{p_i}|$ where $i = 1, 2, 3, 4$ indicates the momentum-ordered ranking of the proton. In addition, the opening angles between the muon and the protons are computed as

$$\cos\theta_{\mu p_i} = \frac{\mathbf{p}_\mu \cdot \mathbf{p}_{p_i}}{p_\mu\, p_{p_i}}, \tag{1}$$

where $\mathbf{p}_\mu$ is the muon three-momentum. We also measure the total hadronic available energy

$$E_{\text{avail}} = \sum_{j=1}^{N_p} T_{p_j}, \tag{2}$$

where N_p is the proton multiplicity, and T_{p_j} denotes the kinetic energy of the jth-leading proton in the event. The combination of these observables with proton multiplicity is directly sensitive to FSI and multi-nucleon processes.

The aim of the analysis is measuring double-differential cross sections in combinations of proton multiplicity, (sub)leading proton momentum, proton-muon opening angles, and available energy. This gives a total of 11 distributions. We adopt the approach proposed in Ref. [9] to report the correlations between the different measurements. By doing this we exploit the full power of the MicroBooNE multivariable dataset. This approach requires grouping all the bins representing the same kinematic distribution in bin blocks. These blocks are unfolded independently, following the procedure described in Sec. III E, while keeping the off-block-diagonal entries in the covariance for the final measurement. A detailed discussion about this blockwise method can be found in Ref. [34]. The first 3 blocks in the analysis represent bins of proton multiplicity sliced in leading proton momentum, opening angle, and available energy. The next 4 bin blocks contain distributions of leading, subleading, 3rd-, and 4th-leading proton momenta in proton multiplicity slices. The remaining 4 blocks contain the corresponding distributions for the proton opening angles.

The binning scheme used in the analysis is tabulated in Appendix A. This binning is used to build histograms for the observables of interest both in reconstructed and true space. The estimated mapping between the reconstructed- and true-level variables is given by the detector response matrix, which accounts for selection efficiency and reconstruction smearing effects. It is defined as

$$\Delta_{i\mu} \equiv \frac{\varphi_{i\mu}}{\varphi_\mu}, \tag{3}$$

where $\varphi_{i\mu}$ is the number of expected selected signal events simultaneously falling in reconstructed bin i and true bin μ, while φ_μ is the total number of signal events in true bin μ. The detector response matrix can be factorized to separate the efficiency and smearing contributions

$$\Delta_{i\mu} = \epsilon_\mu\, M_{i\mu}, \tag{4}$$

with ϵ_μ representing the selection efficiency for true bin μ, and $M_{i\mu}$, the migration matrix, describing the probability that an event generated in true bin μ is reconstructed in bin i. The efficiency histogram and migration matrix for each of the bin blocks are included in Sec. I of the supplemental materials.

D. Uncertainty estimation

We consider the contributions of multiple sources of systematic uncertainty. Many of these are evaluated by repeatedly estimating the expected number of selected events in each bin using varied simulation parameters, under

a multi-universe approach. This leads to a covariance matrix in reconstructed space given by

$$\mathrm{Cov}(n_i,\, n_j) = \frac{1}{N_{\mathrm{univ}}} \sum_{u=0}^{N_{\mathrm{univ}}} (n_i - n_i^u)\,(n_j - n_j^u), \tag{5}$$

where n_i is the number of selected events in bin i according to our nominal simulation, and n_i^u is the corresponding quantity obtained in the uth alternate universe. Here, the number of selected events per bin includes the true signal events and both beam-correlated and beam-off background events. The number of universes N_{univ} considered depends on the systematic effect.

A reweighting scheme based on the approach developed by the MiniBooNE collaboration [12] is adopted to estimate the systematic uncertainties related to the BNB neutrino flux prediction. The alternate universes can be divided in two groups: single-universe variations affecting the geometry in the beam simulation, and hadron production modeling uncertainties.

The systematic uncertainties related to the neutrino-nucleus interaction modeling are included via a reweighting of our baseline interaction model, as described in Ref. [18]. Since the GENIE systematic variations do not cover all relevant sources of modeling uncertainty, an extra systematic uncertainty is created to span the difference between the MicroBooNE GENIE tune and the NuWro event generator [35] in the analysis variables. Other MicroBooNE cross-section analyses [9, 36, 37] include this additional uncertainty when working with similar mesonless signal definitions.

The contribution of these interaction systematic uncertainties enters through both the signal and background event rate estimations. For signal events, only the response matrix defined in Eq. (3) is varied and not the predicted distribution in true kinematics, as these uncertainties modify the efficiency and smearing estimates used in the final cross-section extraction. The detector response matrix is reevaluated in each alternate universe and applied to the truth-level signal events φ_μ in the central-value universe to calculate the varied number of expected selected signal events.

Reinteraction uncertainties account for the effects related to particle propagation in the detector medium. The Geant4Reweight package [38] is used to calculate the corresponding weights from varying the hadronic total cross-section models. This treatment includes proton and pion reinteraction uncertainties.

The systematic uncertainties on the modeling of the detector response are calculated using dedicated MC simulation samples, where different aspects of the LArTPC and light collection system simulations are varied. The LArTPC response variations change the electron–ion recombination model [39], the space-charge effects, and the wire response applying data-driven transformations [40]. Light system variations account for the uncertainties related to the response of the photomultiplier tubes, including light yield mismodeling and decline over the operational period, and the uncertainty in the Rayleigh scattering length [41].

To account for the uncertainty on the beam exposure and the number of target nuclei in the fiducial volume, two additional normalization uncertainties are introduced. These are flat, fully-correlated 2% and 1% uncertainties, respectively, affecting only the signal and beam-correlated background events. Beam-off background events, being directly measured from data, are not affected by these normalization uncertainties.

Because we measure different kinematic distributions simultaneously, the statistical covariance is not a combination of independent Poisson distributions resulting in a diagonal matrix. In this case, a single event belongs to more than one reconstructed bin at the same time, as it appears in multiple distributions within the blockwise scheme. The general prescription to calculate the statistical covariance is

$$\mathrm{Cov}(n_i,\, n_j) = \sum_{k=0}^{n_{ij}} w_k^2, \tag{6}$$

where n_{ij} is the number of selected events which simultaneously belong to the reconstructed bins i and j and w_k are the event weights. For beam data and beam-off background events, $w_k = 1$, and the covariance reduces to n_{ij}. Reference [34] discusses this approach to the statistical uncertainty estimation.

The covariance matrices are calculated for each individual source of uncertainty, and then summed to obtain the total covariance matrix.

E. Cross-section extraction

The observed data consists of reconstructed event counts that have been distorted by detector inefficiencies and resolution effects, as discussed in Sec. III C. These distortions cause some selected events to migrate from the true kinematic bins in which they were generated to different bins in reconstructed space. To recover the underlying

true distribution of events, one must correct for these detector effects through a procedure called unfolding. This is typically written in terms of a matrix multiplication

$$\hat{\varphi}_\mu = \sum_i U_{\mu i}\, d_i, \tag{7}$$

where $\hat{\varphi}_\mu$ is an estimator of the signal event counts in true bin μ, d_i are the background-subtracted reconstructed event counts in reconstructed bin i, and $U_{\mu i}$ is the unfolding matrix. The background-subtracted events counts are calculated by subtracting the beam-correlated and beam-off expected number of background events from the total number of measured events in each reconstructed bin.

The covariance matrix between the estimated signal event counts can be computed via the unfolding matrix as

$$\mathrm{Cov}(\hat{\varphi}_\mu,\, \hat{\varphi}_\nu) = \sum_{a,b} U_{\mu a}\, \mathrm{Cov}(d_a,\, d_b)\, U^{\mathsf{T}}_{b,\nu}, \tag{8}$$

using the covariance matrix between the background-subtracted events counts in reconstructed space. This is estimated from the expected number of selected events

$$\mathrm{Cov}(d_a,\, d_b) \approx \mathrm{Cov}(n_a,\, n_b), \tag{9}$$

following the approach described in Sec. III D.

The unfolding problem is fundamentally ill-posed. Naively, the unfolding matrix could be constructed by directly inverting the response matrix from Eq. (3). However, in most cases the direct inversion is not viable because the response matrix is ill-conditioned. Small fluctuations in measured data lead to large, unstable fluctuations in the inferred true distribution. To address this, the analysis must introduce additional assumptions or constraints, a process known as regularization. These constraints help stabilize the solution, for example, by favoring distributions that are smooth or consistent with physical expectations.

The effects introduced by the regularization methods can be encapsulated in an additional smearing matrix A_C, which relates the regularized and direct-inversion unfolding matrices. It is defined as the product of the unfolding matrix U and the detector response matrix Δ:

$$A_C \equiv U\, \Delta. \tag{10}$$

In the limit of direct matrix inversion, A_C reduces to the identity matrix. This formulation was proposed in Ref. [42] for an unfolding scheme based on a Wiener filter, although the relation in Eq. (10) allows the calculation of the additional smearing matrix for any unfolding method and regularization scheme. In this work, all the theoretical predictions are multiplied by the A_C matrix when checking for goodness-of-fit with the unfolded results, to account for the regularization bias. However, the predictions are shown unaltered in the plots. The elements of the additional smearing matrix for each block are included in Sec. V of the supplemental materials.

In the present analysis, we use the unfolding method proposed by G. D'Agostini [43], which applies Bayes' theorem iteratively. Starting from an arbitrary prior, each iteration refines the estimate in successive steps using the measured data and the detector response matrix. In the many iterations limit, this method approaches the direct inversion result. Regularization is introduced by limiting the number of iterations, avoiding overfitting statistical fluctuations and retaining only the dominant features of the distribution. In the calculation, the selection efficiency ϵ_μ and response matrix $\Delta_{i\mu}$ are kept constant. Each iteration updates the conditional probability to assign a signal event belonging in true bin μ to reconstructed bin i according to Bayes' theorem. The unfolding matrix is obtained from this probability, and then used in Eq. (7) to produce the updated estimate for the next iteration.

The number of iterations used in the unfolding is fixed using the average fractional difference between iterations

$$\mathfrak{F} \equiv \frac{1}{N_{\mathrm{true}}} \sum_\mu \frac{|\hat{\varphi}_\mu^{(n+1)} - \hat{\varphi}_\mu^{(n)}|}{\hat{\varphi}_\mu^{(n+1)}}, \tag{11}$$

where N_{true} is the total number of true bins. We stop iterating when this fractional difference between consecutive iterations falls below 2.5%.

The unfolding procedure described above is applied to each of the bin blocks in the analysis independently. In the blockwise approach adopted, the total unfolding matrix is constructed as the direct sum of all the block-level unfolding matrices

$$U = \bigoplus_b U_b = \begin{pmatrix} U_1 & 0 & \dots \\ 0 & U_2 & \dots \\ \vdots & \vdots & \ddots \end{pmatrix}, \tag{12}$$

resulting in a block diagonal matrix. This total unfolding matrix is used to compute the unfolded covariance matrix according to Eq. (8).

The nominal-flux-integrated [44] differential cross section is derived from the unfolded event counts as

$$\sigma_\mu \equiv \left\langle \frac{\mathrm{d}^n\sigma}{\mathrm{d}\mathbf{x}} \right\rangle_\mu = \frac{\hat{\varphi}_\mu}{\Phi\ \mathcal{N}_{\mathrm{Ar}}\ \Delta\mathbf{x}_\mu}, \tag{13}$$

where Φ is the integrated ν_μ flux over all neutrino energies for the corresponding exposure, $\mathcal{N}_{\mathrm{Ar}}$ is the number of argon nuclei in the FV, and $\Delta\mathbf{x}_\mu$ is the product of the bin widths in each differential variable for true bin μ. Similarly, the covariance in cross-section units is given by

$$\mathrm{Cov}(\sigma_\mu, \sigma_\nu) = \frac{\mathrm{Cov}(\hat{\varphi}_\mu, \hat{\varphi}_\nu)}{\Phi^2\ \mathcal{N}_{\mathrm{Ar}}^2\ \Delta\mathbf{x}_\mu\ \Delta\mathbf{x}_\nu}. \tag{14}$$

The integrated muon neutrino flux is obtained from the BNB flux prediction [12] yielding $\Phi = 9.596 \times 10^{11}\ \nu_\mu/\mathrm{cm}^2$. The number of argon nuclei is computed to be $\mathcal{N}_{\mathrm{Ar}} = 7.992 \times 10^{29}$, using the pure argon density and the FV defined in Sec. III B.

F. Validation studies

The outcome of the unfolding is sensitive to the choice of prior and to the modeling of the detector response. For this reason, it is essential to validate the cross-section extraction method using closure tests and fake data studies, which check whether the unfolding procedure can recover a known input distribution from simulated data.

We perform a fake data study for which we replace the beam-on data with the NuWro single-universe variation samples, described in Sec. III D. In this test, the underlying true distributions are different from the GENIE MicroBooNE tune predictions. Therefore, it assesses the model-independence of the cross-section extraction method, testing whether the procedure can recover the underlying NuWro cross section despite using the MicroBooNE tune prior. Here, MC statistical and neutrino interaction model uncertainties are considered. The unfolded fake data distributions are shown in Sec. II A of the supplemental materials. For all blocks, the distributions show better agreement with the NuWro prediction than with the MicroBooNE tune prediction.

TABLE II. Goodness-of-fit for the comparison between fake data unfolded with the data- and MC-derived resimulated response matrices for each block, computed using the response matrix statistical covariance.

Block	χ^2/ndof	p-value
1: (p_{p_1}, N_p)	1.92 / 27	1.00
2: ($\cos\theta_{\mu p_1}$, N_p)	0.88 / 20	1.00
3: (E_{avail}, N_p)	0.49 / 12	1.00
4: (N_p, p_{p_1})	1.33 / 33	1.00
5: (N_p, p_{p_2})	0.74 / 15	1.00
6: (N_p, p_{p_3})	0.40 / 8	1.00
7: (N_p, p_{p_4})	0.31 / 2	0.86
8: (N_p, $\cos\theta_{\mu p_1}$)	2.34 / 32	1.00
9: (N_p, $\cos\theta_{\mu p_2}$)	0.83 / 20	1.00
10: (N_p, $\cos\theta_{\mu p_3}$)	2.09 / 6	0.91
11: (N_p, $\cos\theta_{\mu p_4}$)	1.98 / 2	0.37

A separate data-driven validation study is performed to assess the sensitivity of the response matrix to potential mismodeling of the subleading proton kinematics near the reconstruction threshold. Selected data and MC events are resimulated using their reconstructed momenta as inputs to the full simulation and reconstruction chain, and the resulting samples are used to construct alternative response matrices. These are then used to unfold central-value fake data, and the two sets of unfolded results are compared. Table II summarizes the χ^2 values for the comparison between the data- and MC-derived results. The two are compatible across all blocks, indicating no evidence of bias from this source. Good closure is also achieved individually for both response matrices. The individual distributions can be found in Sec. II B of the supplemental materials, and the full procedure is described in Appendix B.

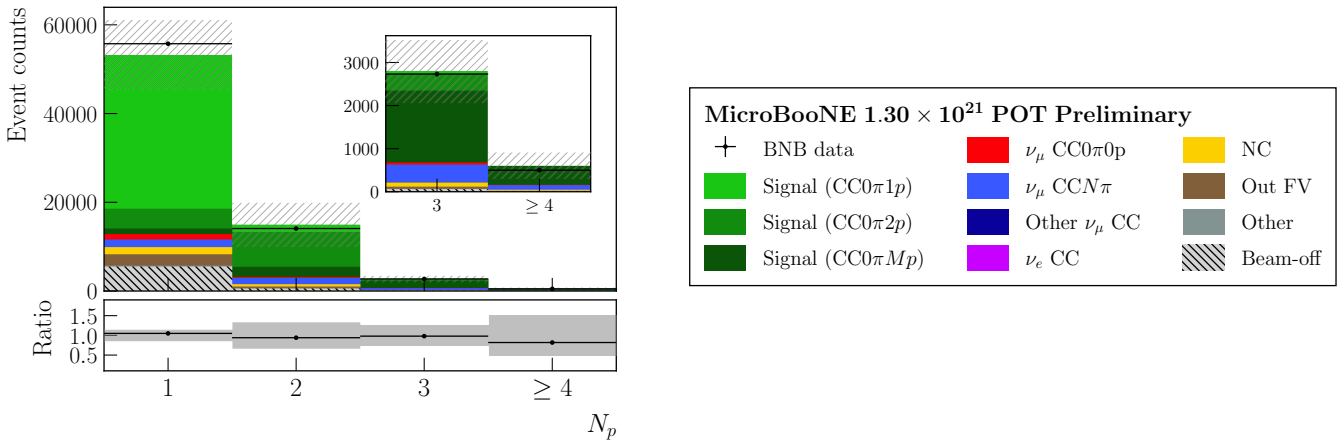

FIG. 2. Reconstructed proton multiplicity event rate distribution. The total uncertainty on the prediction is indicated by the hatched boxes. The bottom panel shows the ratio of the observed data to the central-value prediction, with the gray band indicating the fractional uncertainty. The inset shows an enlarged view of the $N_p = 3$ and $N_p \geq 4$ bins.

IV. RESULTS

A. Event rate distributions

We compare the GENIE MicroBooNE tune predictions to the collected BNB data for a total beam exposure of 1.30×10^{21} POT. The selected data sample contains 73058 events, comprising 55740 $1p$, 14087 $2p$, 2732 $3p$, and 499 $\geq 4p$ events. Figure 2 shows the reconstructed proton multiplicity distribution. The data points include only statistical uncertainties. The hatched boxes indicate the total uncertainty on the prediction (MC simulation and beam-off statistical plus systematic contributions). The different event categories shown are described in Sec. III A.

The event rate distributions comparing the central-value predictions to the data for bin blocks 1, 2, and 3 are shown in Figs. 3, 4, and 5. Figure 6 shows blocks 4, 5, 6, and 7, corresponding to the proton momenta distributions in slices of fixed proton multiplicity. Similarly, Fig. 7 contains the distributions for blocks 8, 9, 10, and 11, showing proton opening angles for the different multiplicity slices. The corresponding distributions with the signal component decomposed by primary interaction mode can be found in Sec. III of the supplemental materials.

TABLE III. Goodness-of-fit between the observed data and the central-value prediction for the reconstructed event rate distributions in each block computed using the total covariance (statistical plus systematic).

Block	χ^2/ndof	p-value
1: (p_{p_1}, N_p)	20.59 / 27	0.81
2: ($\cos\theta_{\mu p_1}$, N_p)	45.39 / 20	0.00
3: (E_{avail}, N_p)	7.30 / 12	0.84
4: (N_p, p_{p_1})	28.41 / 33	0.69
5: (N_p, p_{p_2})	17.12 / 15	0.31
6: (N_p, p_{p_3})	8.14 / 8	0.42
7: (N_p, p_{p_4})	2.15 / 2	0.34
8: (N_p, $\cos\theta_{\mu p_1}$)	45.87 / 32	0.05
9: (N_p, $\cos\theta_{\mu p_2}$)	8.74 / 20	0.99
10: (N_p, $\cos\theta_{\mu p_3}$)	3.53 / 6	0.74
11: (N_p, $\cos\theta_{\mu p_4}$)	0.23 / 2	0.89

Good agreement between data and the central-value prediction is observed for most bin blocks. Table III shows a per-block goodness-of-fit summary. The leading proton opening angle distributions (blocks 2 and 8) are a notable exception, showing significant tension between data and MC. Similar discrepancies in this observable have been

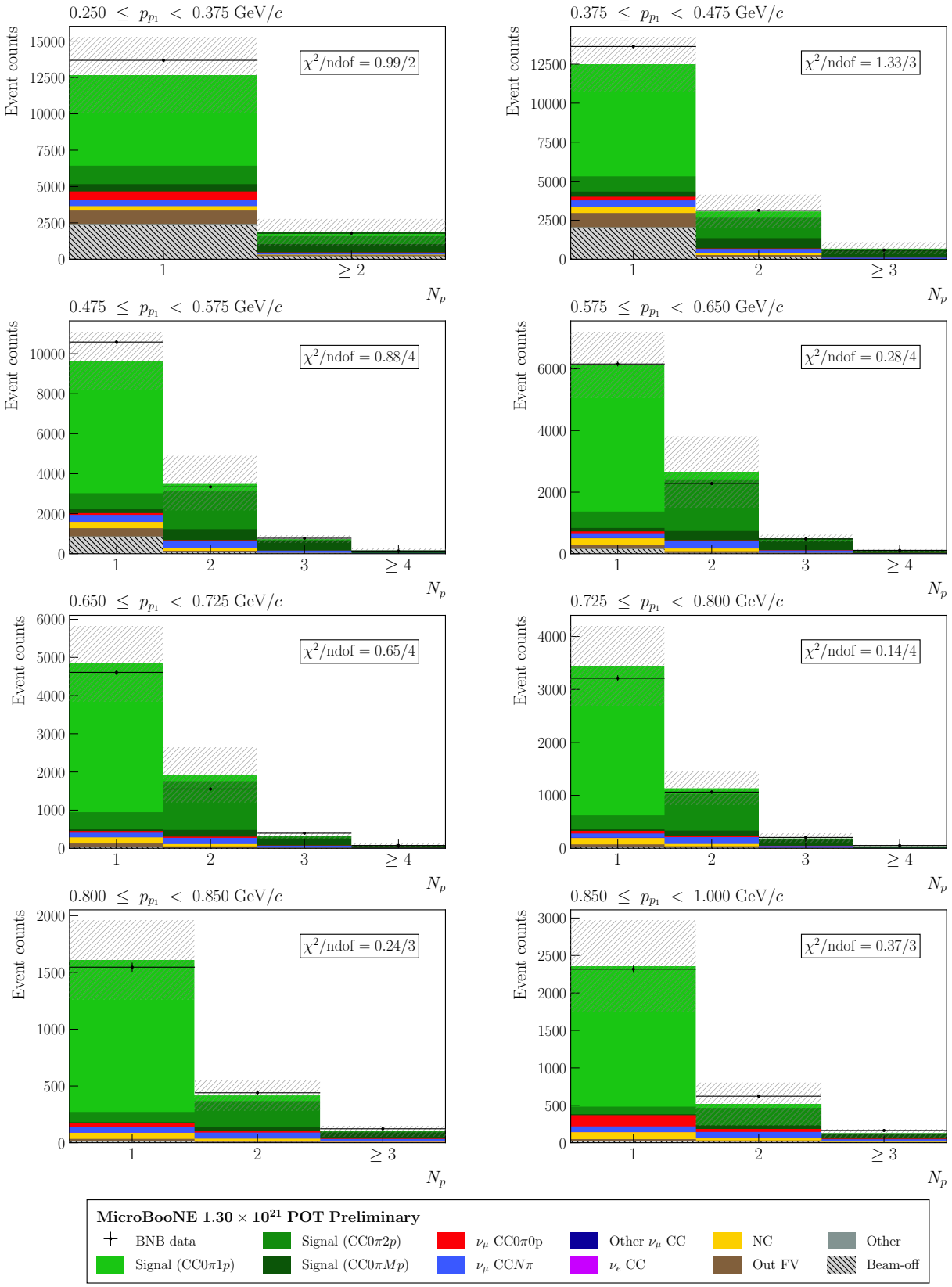

FIG. 3. Reconstructed event rate distributions for block 1, corresponding to the double-differential measurement (p_{p_1}, N_p). The total uncertainty on the prediction is indicated by the hatched boxes. The per-slice χ^2/ndof for the central-value prediction is shown in each individual panel.

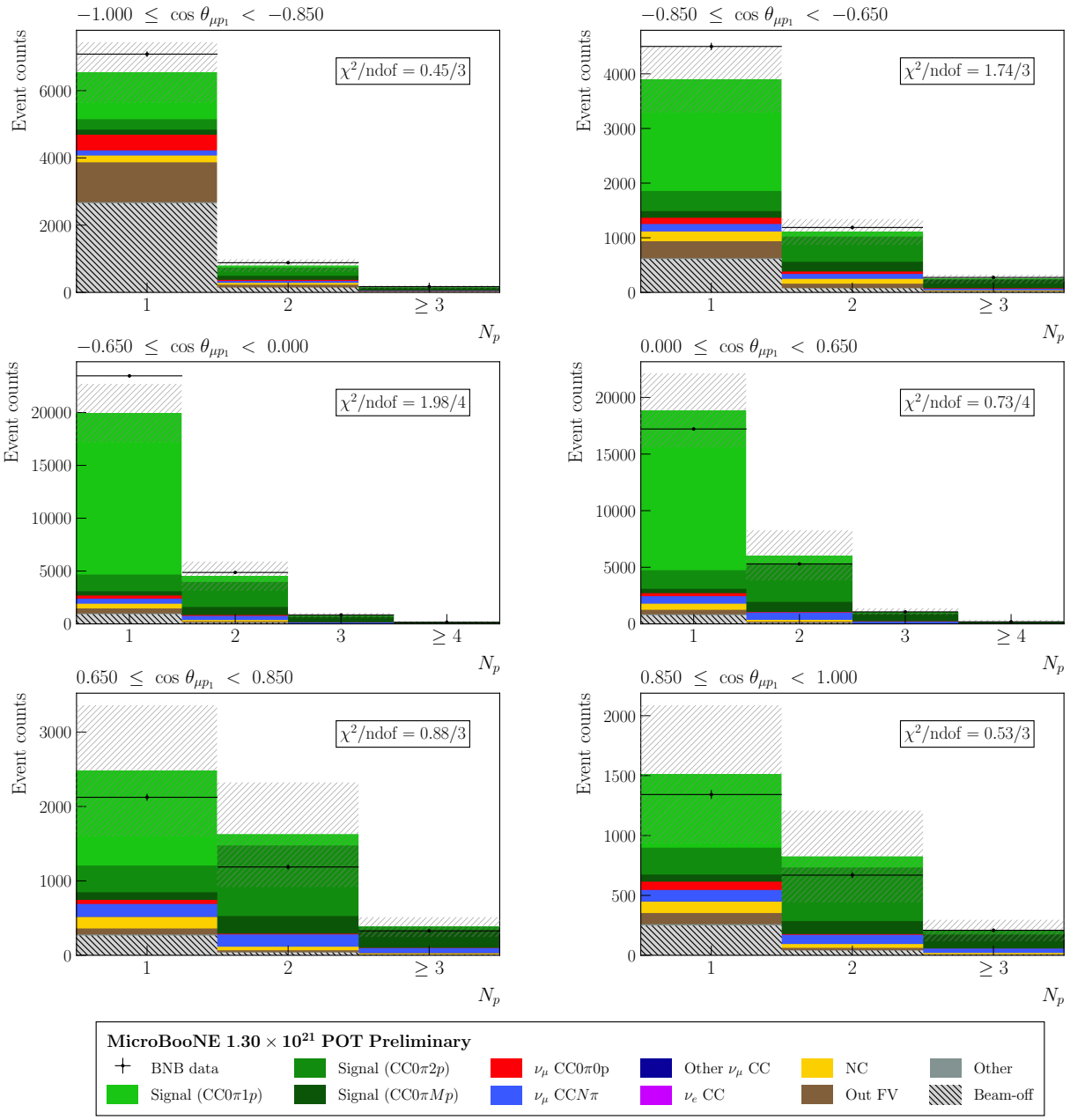

FIG. 4. Reconstructed event rate distributions for block 2, corresponding to the double-differential measurement ($\cos\theta_{\mu p_1}$, N_p). The total uncertainty on the prediction is indicated by the hatched boxes. The per-slice χ^2/ndof for the central-value prediction is shown in each individual panel.

reported in previous MicroBooNE CC0πNp measurements [9].

The adequacy of the background modeling is assessed through a sideband study. A combined sideband selection is formed merging the contributions from the three main background components in the analysis. The background-enhanced selections are defined by inverting some of the selection cuts:

- Out FV: events with a reconstructed vertex outside the fiducial volume.

- NC: events for which a muon candidate could not be identified.

- CC$N\pi$: events with some proton candidates failing the log-likelihood ratio PID score cut.

Events passing any of these three selection criteria are accepted by the combined sideband selection.

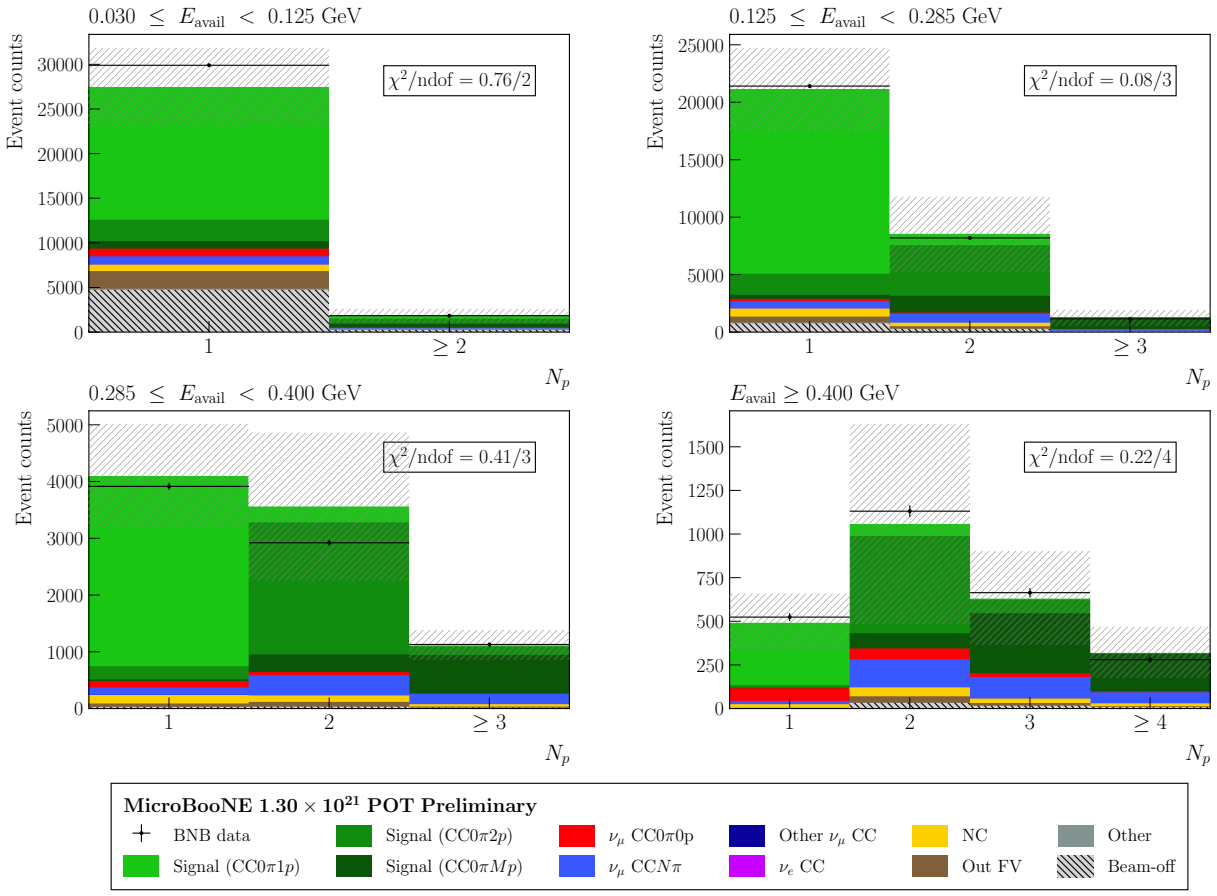

FIG. 5. Reconstructed event rate distributions for block 3, corresponding to the double-differential measurement (E_{avail}, N_p). The total uncertainty on the prediction is indicated by the hatched boxes. The per-slice χ^2/ndof for the central-value prediction is shown in each individual panel.

The combined sideband study shows overall good agreement between data and prediction for most bin blocks. The event rate distributions for the different blocks can be found in Sec. IV of the supplemental materials. A dedicated study is performed to investigate the discrepancy in the leading proton opening angle distributions, in which bin-by-bin signal and background correction factors are simultaneously extracted from the selection and sideband distributions. The null hypothesis that the background is correctly modeled cannot be rejected (p-values of 0.98 and 0.77 for blocks 2 and 8, respectively), indicating that the observed disagreement is consistent with signal mismodeling. This confirms that the background subtraction is not affected by this discrepancy. The procedure followed is described in Appendix C.

A second concern is whether the signal mismodeling could bias the response matrix used in the cross-section extraction. The data-driven response matrix validation described in Sec. III F directly addresses this. The resimulated data and MC response matrices produce compatible unfolded results for blocks 2 and 8, confirming that the response matrix is not significantly biased by the observed differences in proton kinematics between data and simulation.

Together, these two results demonstrate that the cross-section extraction method remains reliable for these distributions despite the lack of agreement between data and MC at the event-rate level.

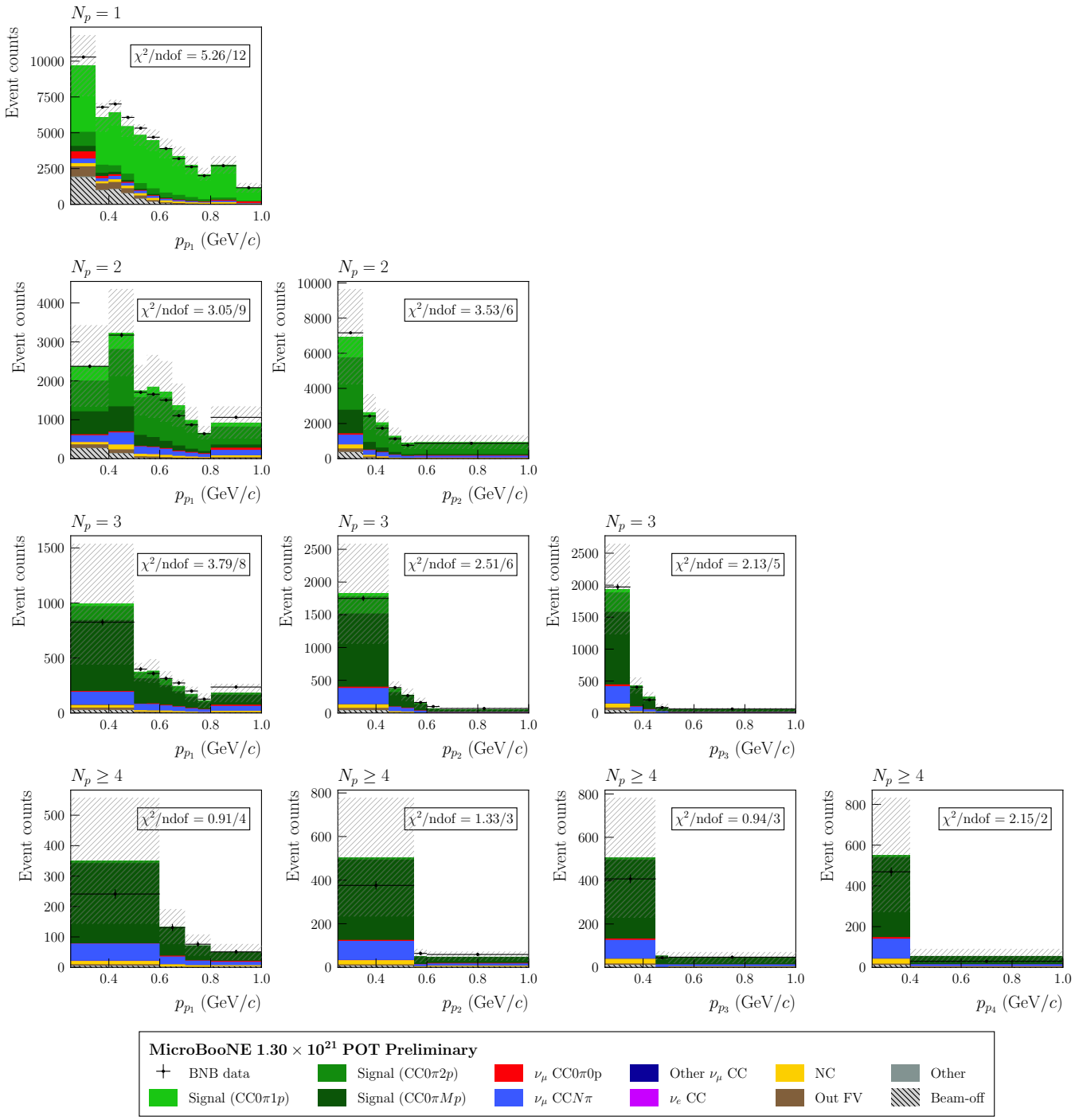

FIG. 6. Reconstructed event rate distributions for blocks 4, 5, 6, and 7, corresponding to the double-differential measurements (N_p, p_{p_i}). The total uncertainty on the prediction is indicated by the hatched boxes. The per-slice χ^2/ndof for the central-value prediction is shown in each individual panel.

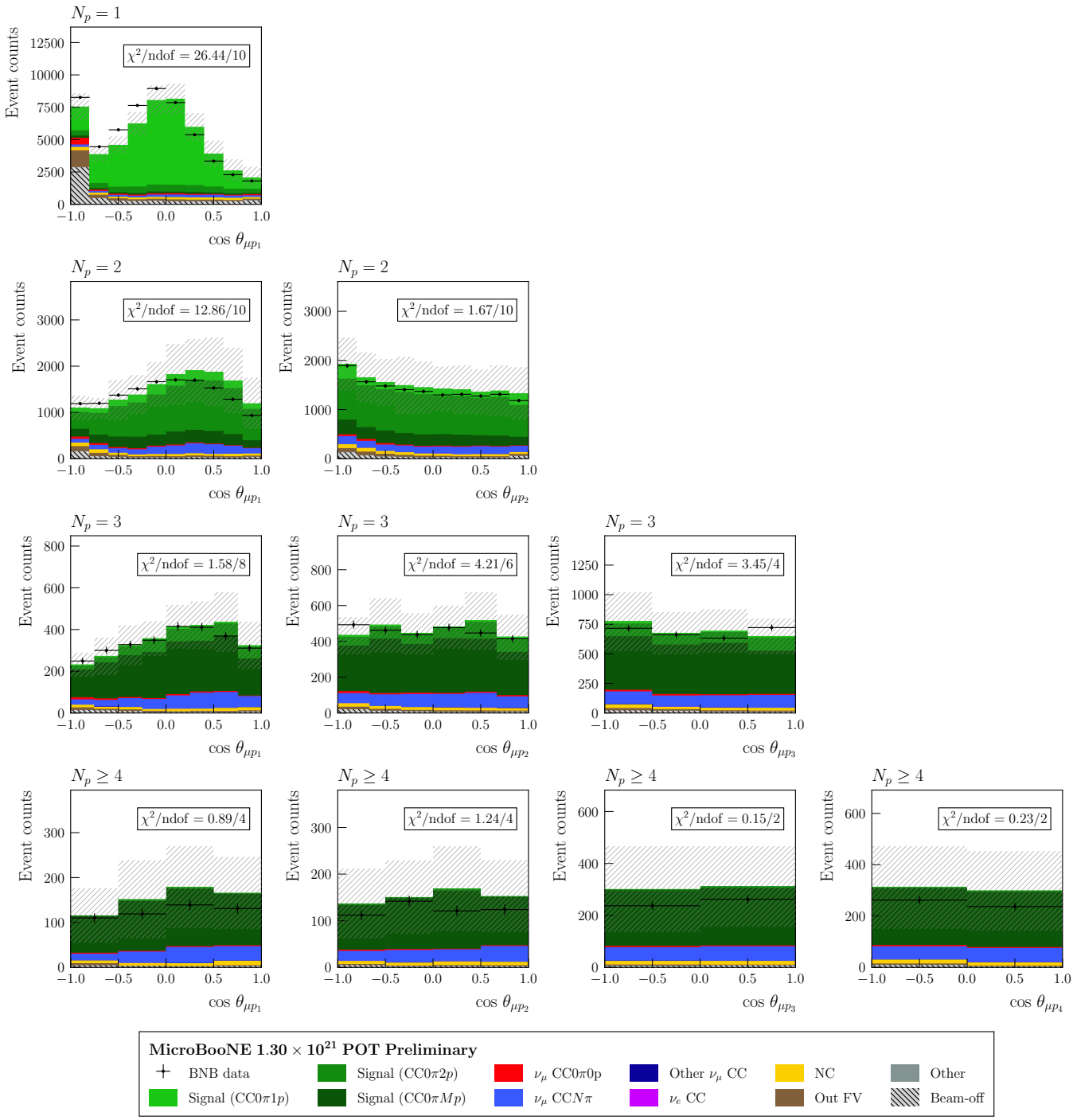

FIG. 7. Reconstructed event rate distributions for blocks 8, 9, 10, and 11, corresponding to the double-differential measurements (N_p, cos θ_{p_i}). The total uncertainty on the prediction is indicated by the hatched boxes. The per-slice χ^2/ndof for the central-value prediction is shown in each individual panel.

B. Generator configurations

The nominal generator prediction used in this analysis is the GENIE MicroBooNE tune. It uses the local Fermi gas (LFG) model [45] as a description of the nucleus. The Valencia model describes the QE and MEC CC interactions [46, 47]. The Kuzmin-Lyubushkin-Naumov and Berger-Sehgal (KLN-BS) model [48–50] is used to simulate the resonant pion production. DIS interactions are described by the Bodek-Yang (BY) model [51, 52], together with PYTHIA [53] for the hadronization. The FSI are simulated using the effective intranuclear transport model (hA2018) included in GENIE [54]. Additionally, this prediction includes some MicroBooNE-specific tuning of the model parameters [18].

The unfolded cross sections are compared to predictions from several alternative event generators widely used in the neutrino scattering community, including models currently adopted by the SBN and DUNE programs. These generators differ in their treatment of the nuclear structure, interaction dynamics, and final state interactions. The comparisons are performed using the NUISANCE framework [55]. Additional generator configurations exploring further model variations are described and compared in Sec. VI of the supplemental materials.

NuWro `v25.11` uses a spectral function (SF) approach to model the ground state of the argon nucleus in the QE channel [56], while a LFG model is used for all other dynamics. It uses the Llewellyn Smith (LS) model [57] for QE events, and the Valencia 2020 model [58] for MEC. Single pion production is described by the Ghent hybrid model [59], while DIS uses the BY model. For QE events, NuWro applies a convolution scheme which broadens the cross section via a folding function and shifts the energy of the struck nucleon before propagating nucleons through a standard intranuclear cascade [60], while non-QE channels are treated with the cascade alone. An additional NuWro sample with fine-tuned FSI is also included, in which the effective strength of the nucleon cascade is increased by approximately 24% based on fits to MINERvA transverse kinematics data across multiple nuclear targets [61].

NEUT `v5.6.2` uses a LFG model to describe the nuclear state. The Nieves model is used for CCQE interactions, and the Valencia 2p2h model describes the MEC contribution. RES events use the BS model, and the BY model describes DIS. FSI are modeled by a semi-classical cascade model with medium corrections for pions [62].

GiBUU [63] `2025` also includes the LFG model for the initial state of the nucleus. GiBUU uses its own parametrizations for the QE and RES events [64]. MEC interactions are modeled using semi-inclusive electron scattering data [65]. PYTHIA [53] is used for DIS events. Hadrons are propagated through the remnant nucleus by numerically solving the Boltzmann-Uehling-Uhlenbeck (BUU) transport equation, with a nuclear potential consistent with the initial state. An additional GiBUU `2025` sample with in-medium modifications to the nucleon-nucleon cross sections, including a density-dependent lowering of the NN cross section [66], is also studied.

The GENIE `AR23_20i_00_000` configuration [67], generated with `v3.6.2`, was developed for use in the DUNE and SBN programs. It uses a modified LFG model that populates a broader region of missing energy and momentum space compared to the standard LFG. Like the `G18_10a` configurations, it uses the Nieves QE model and the Valencia 2p2h MEC, but employs the z-expansion parameterization of the axial form factor rather than the dipole approximation [68]. Three additional `AR23` variants are produced with alternative FSI models, with all other settings unchanged: `AR23_20j_00_000` uses the hN intranuclear cascade, `AR23_20k_00_000` uses the INCL (Liège) cascade [69, 70], and `AR23_20l_00_000` uses the Geant4 Bertini cascade [71]. The configurations for these FSI variants were prepared for this analysis.

C. Unfolded cross-section results

The unfolded differential cross-section results for all bin blocks are shown in Figs. 8 to 17, presented in pairs for each block. The first figure in each pair compares the data to generator predictions extracted from the GENIE MicroBooNE tune (G18T), NuWro `v25.11` (NuWro), NuWro `v25.11` with fine-tuned FSI [61] (NuWro FSI), NEUT `v5.6.2` (NEUT), GiBUU `2025` (GiBUU), and GiBUU `2025` with in-medium corrections [66] (GiBUU InMed), described above. The second figure in the pair compares the results to the GENIE `AR23` configuration predictions using the hA, hN, INCL, and Geant4 Bertini cascade (G4BC) FSI models. Comparisons of the unfolded cross-section results to additional generator configurations are provided in Sec. VI of the supplemental materials. For each individual slice and prediction, a χ^2 metric describing its agreement with the data is reported in the legend. We use the covariance matrix decomposition described in Appendix D to separate the uncertainties into normalization, shape, and mixed contributions, following the convention of previous MicroBooNE analyses [9, 36, 37, 72–74]. The inner (black) error bars in the data points represent statistical uncertainties, while the outer (red) error bars include shape-only systematic contributions. Normalization and mixed uncertainties are indicated by the gray histograms. The bottom panels contain the ratio of the different predictions to the data. In this case, the data error bars represent the total uncertainty in the measurement. A detailed breakdown of the fractional uncertainty from each systematic source is provided in Sec. VII of the supplemental materials. Tables IV and V summarize the per-block χ^2 values for all generator predictions.

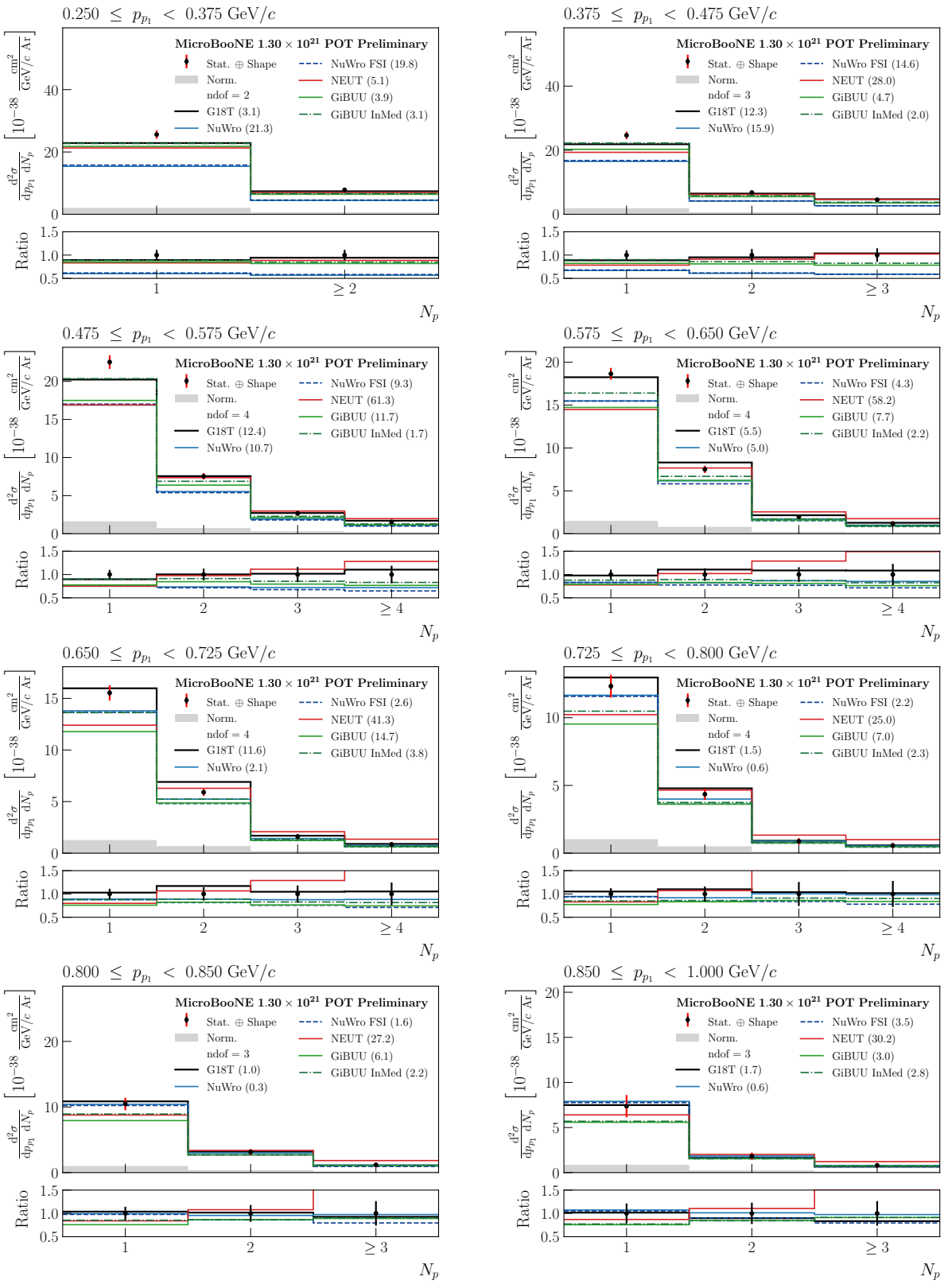

FIG. 8. Flux-integrated double-differential cross sections for block 1 (p_{p_1}, N_p), extracted from the full MicroBooNE BNB dataset (black data points). Error bars indicate statistical and shape-only uncertainties, while the gray band indicates the normalization uncertainty. Predictions from the GENIE MicroBooNE tune, NuWro, NEUT, and GiBUU are overlaid as indicated in the legend. The χ^2 for each prediction is indicated in parentheses. The bottom panels show the ratio of the predictions to the unfolded data.

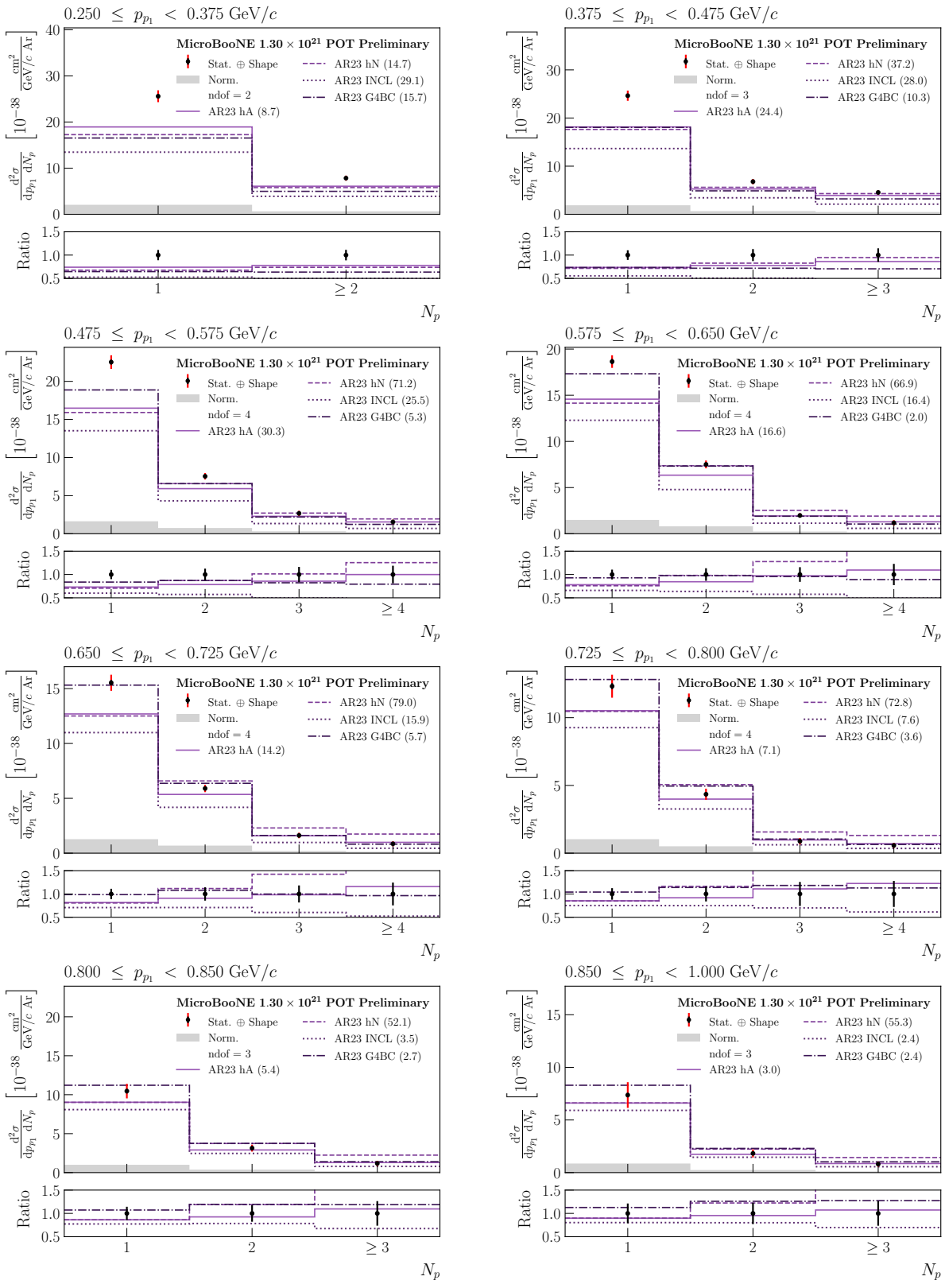

FIG. 9. Flux-integrated double-differential cross sections for block 1 (p_{p_1}, N_p), extracted from the full MicroBooNE BNB dataset (black data points). Error bars indicate statistical and shape-only uncertainties, while the gray band indicates the normalization uncertainty. Predictions from the GENIE `AR23` configuration with the hA, hN, INCL, and G4BC FSI models are overlaid as indicated in the legend. The χ^2 for each prediction is indicated in parentheses. The bottom panels show the ratio of the predictions to the unfolded data.

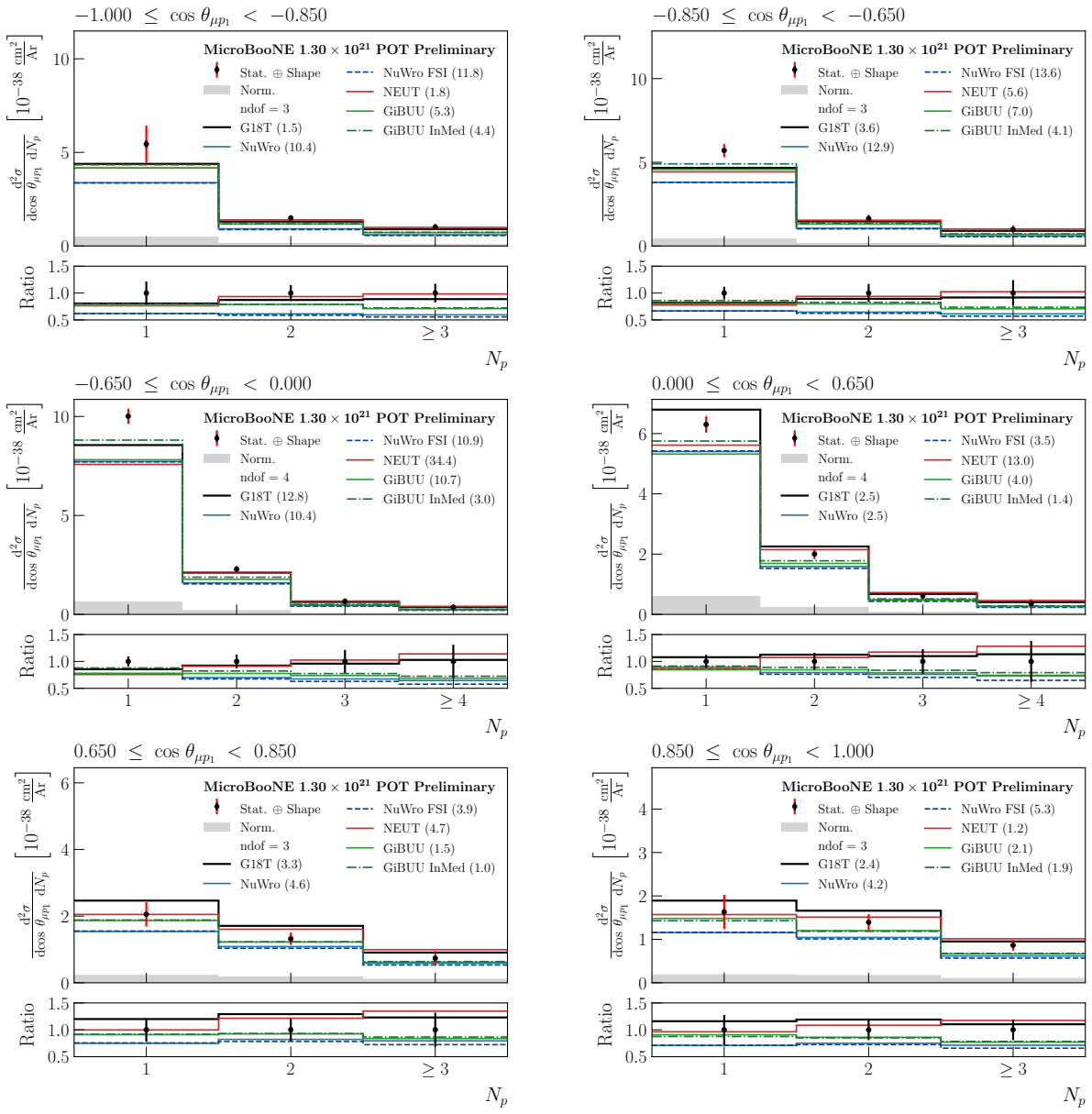

FIG. 10. Flux-integrated double-differential cross sections for block 2 ($\cos\theta_{\mu p_1}$, N_p), extracted from the full MicroBooNE BNB dataset (black data points). Error bars indicate statistical and shape-only uncertainties, while the gray band indicates the normalization uncertainty. Predictions from the GENIE MicroBooNE tune, NuWro, NEUT, and GiBUU are overlaid as indicated in the legend. The χ^2 for each prediction is indicated in parentheses. The bottom panels show the ratio of the predictions to the unfolded data.

Figures 8 and 9 show the double-differential cross-section measurement in leading proton momentum and proton multiplicity. In this case, GiBUU InMed provides the best description of the data across all slices ($\chi^2/\text{ndof} = 25.3/27$ for the full block), being the only generator consistent with the observed distributions at the 1σ level. The default GiBUU prediction is also in good agreement with the data, suggesting that the BUU transport framework captures the essential features of proton production. NEUT exhibits the largest disagreement with the measurement, systematically overpredicting the $N_p \geq 2$ events relative to the $N_p = 1$ cross section. The `AR23` FSI variations span a wide range of χ^2 from 77.2/27 (INCL) to 370.8/27 (hN), underlining the sensitivity of multi-proton observables to the cascade model. NuWro tends to underpredict the cross section across all multiplicities, particularly at low leading proton momentum. The FSI tuning marginally improves the block χ^2; however, it does not resolve the deficit. The MicroBooNE tune shows some discrepancy in the mid-momentum range, slightly overpredicting the $N_p = 2$ events relative to $N_p = 1$ and higher multiplicity events.

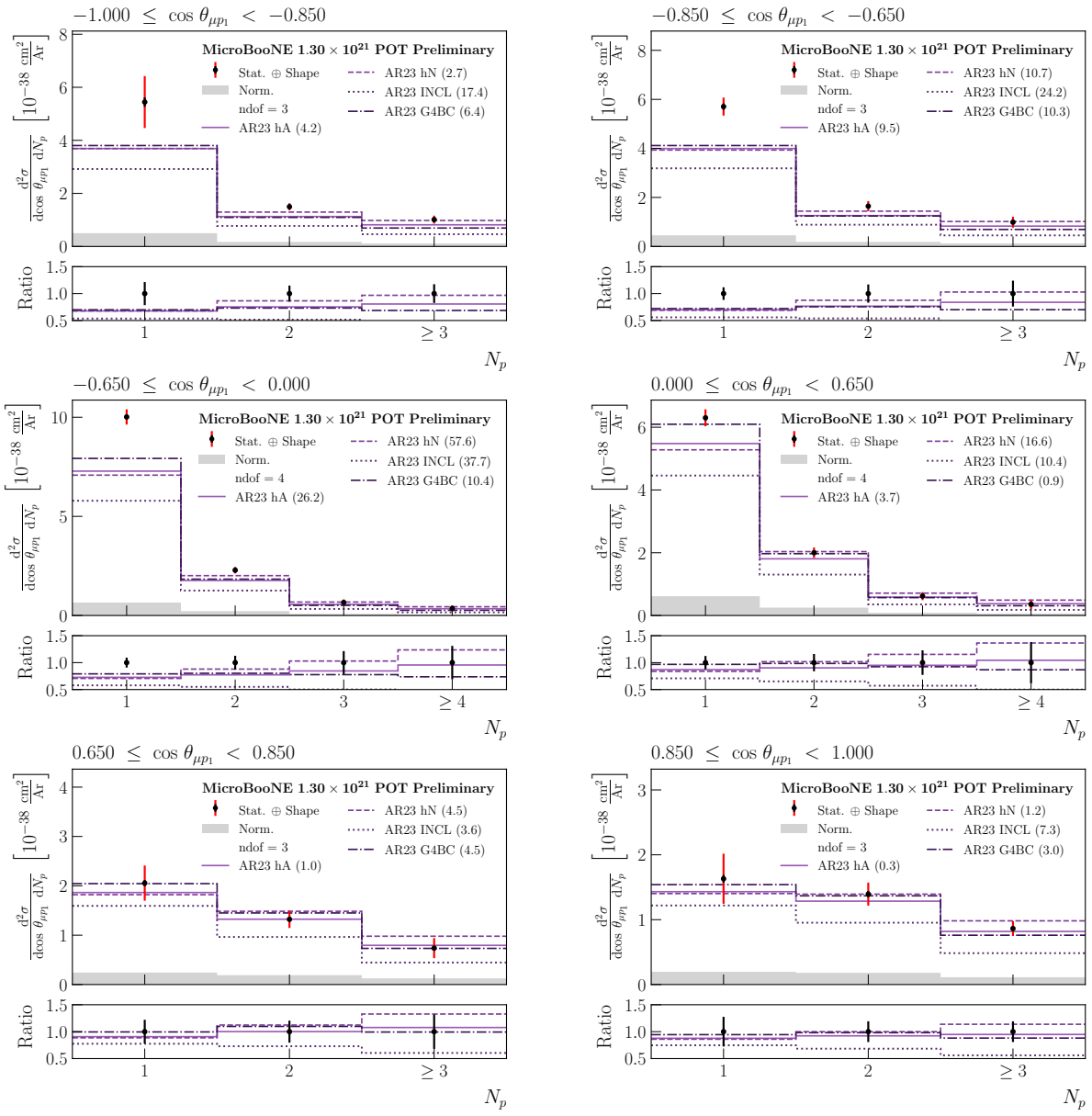

FIG. 11. Flux-integrated double-differential cross sections for block 2 ($\cos\theta_{\mu p_1}$, N_p), extracted from the full MicroBooNE BNB dataset (black data points). Error bars indicate statistical and shape-only uncertainties, while the gray band indicates the normalization uncertainty. Predictions from the GENIE `AR23` configuration with the hA, hN, INCL, and G4BC FSI models are overlaid as indicated in the legend. The χ^2 for each prediction is indicated in parentheses. The bottom panels show the ratio of the predictions to the unfolded data.

The extracted double-differential cross-section values in slices of leading proton opening angle and bins of proton multiplicity are reported in Figs. 10 and 11. Again, GiBUU InMed and the default GiBUU prediction provide the best overall agreement with the measurement. This reinforces the observation from block 1: the BUU approach with in-medium corrections best reproduces the proton multiplicity distributions across kinematic variables. The disagreement between data and models is most pronounced for backward angles, where most generators underpredict the $N_p = 1$ cross section, particularly NuWro. NEUT performs comparatively well in the very backward and forward regions, although it accumulates tension at intermediate angles where it overestimates the multi-proton contribution. The `AR23` hA and G4BC variations describe the measurement well at forward angles, but show increasing disagreement at backward angles where $N_p = 1$ dominates.

Figures 12 and 13 present the double-differential cross sections measured in total available energy and proton multiplicity. GiBUU InMed gives the best overall description of the measured data, followed by the NuWro prediction

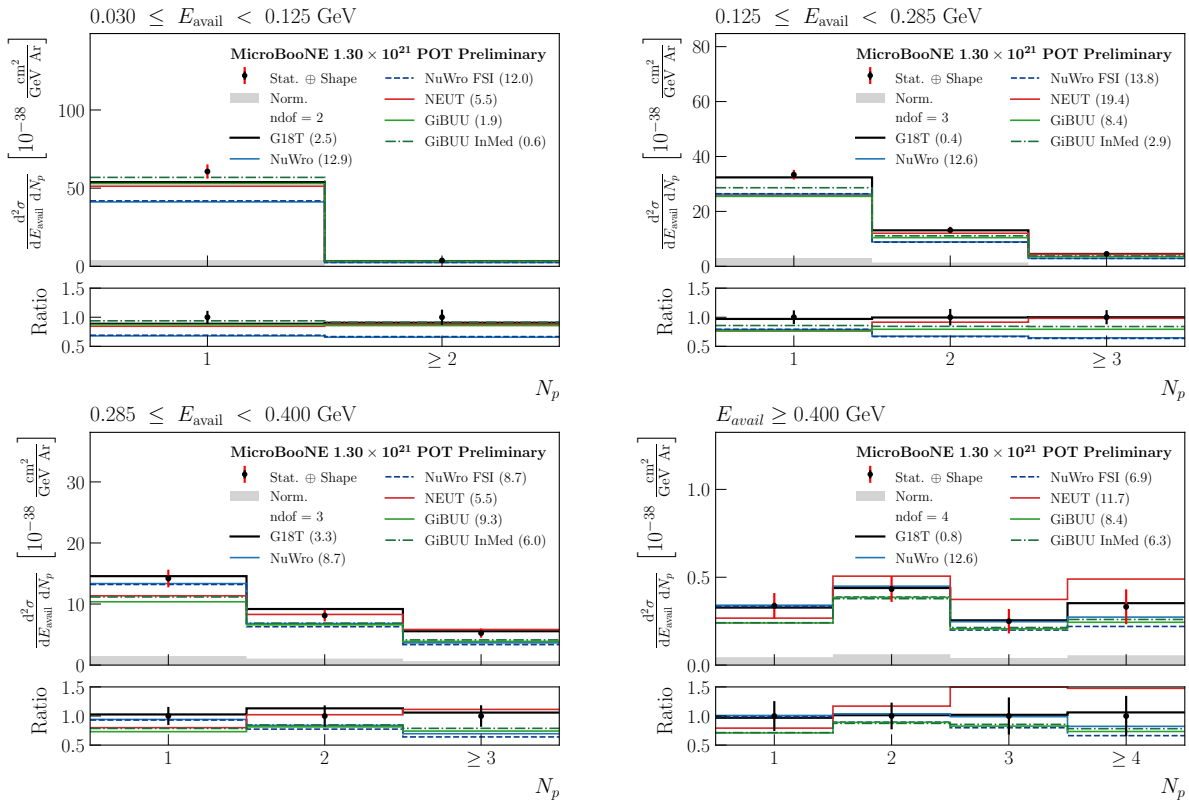

FIG. 12. Flux-integrated double-differential cross sections for block 3 (E_{avail}, N_p), extracted from the full MicroBooNE BNB dataset (black data points). Error bars indicate statistical and shape-only uncertainties, while the gray band indicates the normalization uncertainty. Predictions from the GENIE MicroBooNE tune, NuWro, NEUT, and GiBUU are overlaid as indicated in the legend. The χ^2 for each prediction is indicated in parentheses. The bottom panels show the ratio of the predictions to the unfolded data.

with fine-tuned FSI. However, the two generators perform best in complementary kinematic regimes: GiBUU InMed at low available energies and NuWro FSI in the high-energy region. The MicroBooNE tune achieves good per-slice agreement with the data, yet its block-global χ^2 of 42.2/12 indicates a poor overall fit introduced by cross-slice correlations. Both NuWro configurations underpredict the cross section at low and intermediate energies, consistent with the results from blocks 1 and 2. NEUT again shows a characteristic shape distortion: it overestimates the high-multiplicity events at high energy, similar to what is observed in the leading proton momentum distributions. Among the `AR23` FSI variations, the hN cascade yields the largest disagreement, underpredicting the $N_p = 1$ cross section while overpredicting higher multiplicities, a pattern consistent with excessive rescattering of primary protons through the cascade. INCL and hA are the best-performing variations, although both underpredict the $N_p = 1$ cross section at low energies. Although INCL achieves a comparable χ^2 to hA in this block, this is partly driven by the normalization component of the covariance absorbing its uniform deficit, rather than reflecting a genuine shape agreement.

The measured double-differential cross sections in the leading and subleading proton momenta and slices of fixed proton multiplicity are displayed in Figs. 14 and 15. The GiBUU InMed prediction gives the best agreement for the leading proton momentum block, accurately reproducing the spectral shape across all multiplicity slices. The standard GiBUU also provides an acceptable description of the data. A hierarchy emerges as one moves to the subleading proton distributions: for the 2nd-leading proton all generators yield χ^2/ndof values well above 1. The MicroBooNE tune and GiBUU (both configurations) perform comparably at the block-level, with significant tension concentrated in the $N_p = 2$ slice. The MicroBooNE tune prediction outperforms the rest of the generators in the 3rd-leading proton block. For the 4th-leading proton, GiBUU InMed, `AR23` G4BC, and the MicroBooNE tune all describe the measurement adequately, although the binning limits the discriminating power of this distribution. GiBUU InMed excels for the leading proton but shows reduced agreement at higher proton ranks, suggesting an underestimation of the cross section for the softer, subleading protons produced through secondary rescattering. Conversely, NEUT systematically produces a harder momentum spectrum for the subleading protons, overpredicting the high-momentum tails, particularly for $N_p \geq 3$. NuWro exhibits a persistent deficit at low momenta, indicating an underprediction of

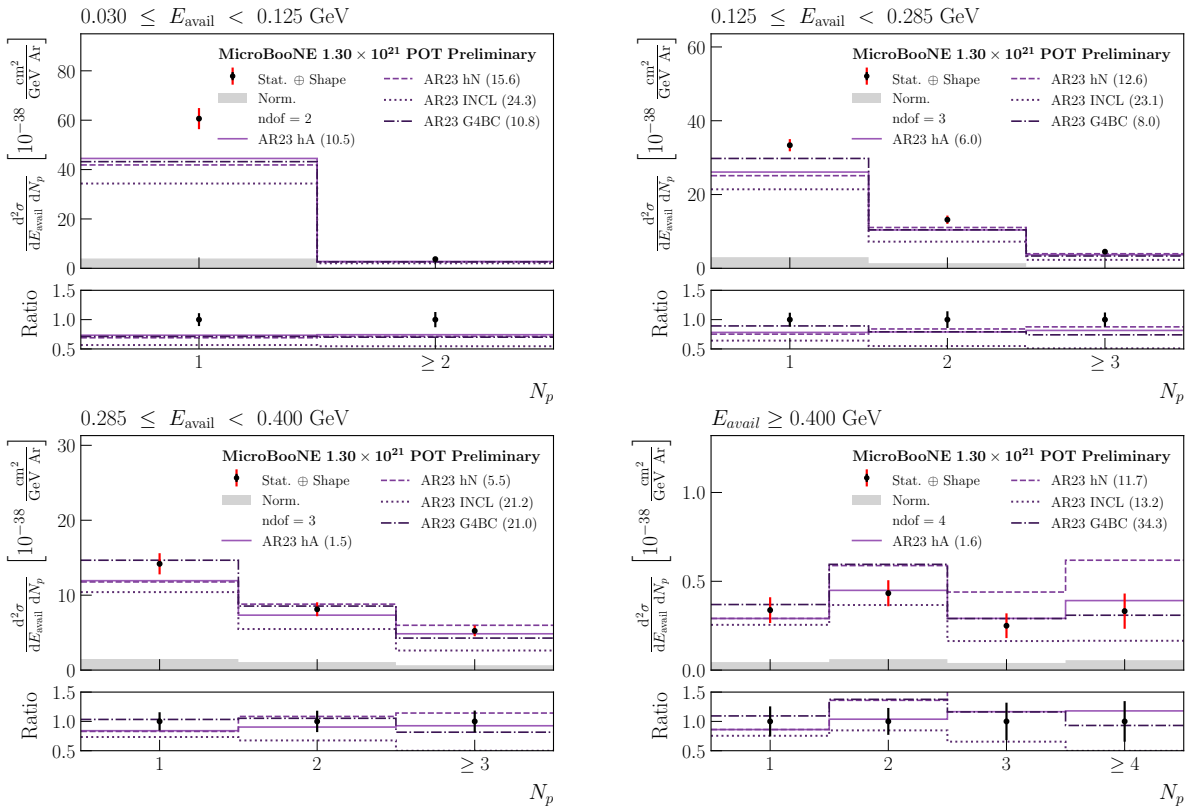

FIG. 13. Flux-integrated double-differential cross sections for block 3 (E_{avail}, N_p), extracted from the full MicroBooNE BNB dataset (black data points). Error bars indicate statistical and shape-only uncertainties, while the gray band indicates the normalization uncertainty. Predictions from the GENIE `AR23` configuration with the hA, hN, INCL, and G4BC FSI models are overlaid as indicated in the legend. The χ^2 for each prediction is indicated in parentheses. The bottom panels show the ratio of the predictions to the unfolded data.

low-momentum secondary protons. The NuWro FSI configuration only partially improves the agreement. The `AR23` INCL configuration consistently underpredicts the cross section across all slices, continuing the pattern observed in the previous blocks. The `AR23` hN prediction shares the underprediction of the leading proton distributions common to all `AR23` configurations at low multiplicities, but additionally overestimates the high-momentum region at higher multiplicities, consistent with the excessive rescattering pattern observed in block 1.

Figures 16 and 17 report the double-differential cross sections measured in the leading and subleading proton opening angles and proton multiplicity. The best description of the leading proton opening angle block is provided by GiBUU InMed, being the only generator with a p-value above 0.05 ($\chi^2/\text{ndof} = 42.7/32$). This is primarily driven by its agreement with the data in the $N_p = 1$ slice, where all other models yield $\chi^2 = 44$–80 for the 10 bins. The tension in this distribution is concentrated at backward angles, $\cos\theta_{\mu p_1} < 0$, where data significantly exceed all predictions. This suggests that single-proton events populate wider opening angles than most generators predict, a feature that the in-medium corrections in GiBUU partially recover. In the $N_p = 2$ slices an informative contrast emerges between the leading and subleading proton angular distributions: the leading proton retains a strongly peaked structure, reflecting its correlation with the momentum-transfer direction, while the 2nd-leading proton distribution is nearly isotropic across the full angular range. The peaked $\cos\theta_{\mu p_1}$ shape in the $N_p = 2$ slice proves difficult to model, with GiBUU InMed and `AR23` hN providing the closest agreement. The isotropy of the subleading protons is well reproduced by all generators regardless of their FSI implementation, suggesting that this is a generic feature of intranuclear rescattering rather than a detail sensitive to a particular cascade model. The 3rd- and 4th-leading proton opening angle blocks offer limited discriminating power due to the reduced number of bins, with most generators providing an adequate description. The `AR23` INCL prediction continues to systematically underpredict the cross section across all proton ranks and angular bins. Together with the results from the previous blocks, this points to a systematic underprediction of the overall proton yield in the INCL cascade model on argon.

When the reconstructed and true binning are identical, as in this analysis, event sharing between blocks introduces structural constraints that reduce the number of independent degrees of freedom in the final measurement. From

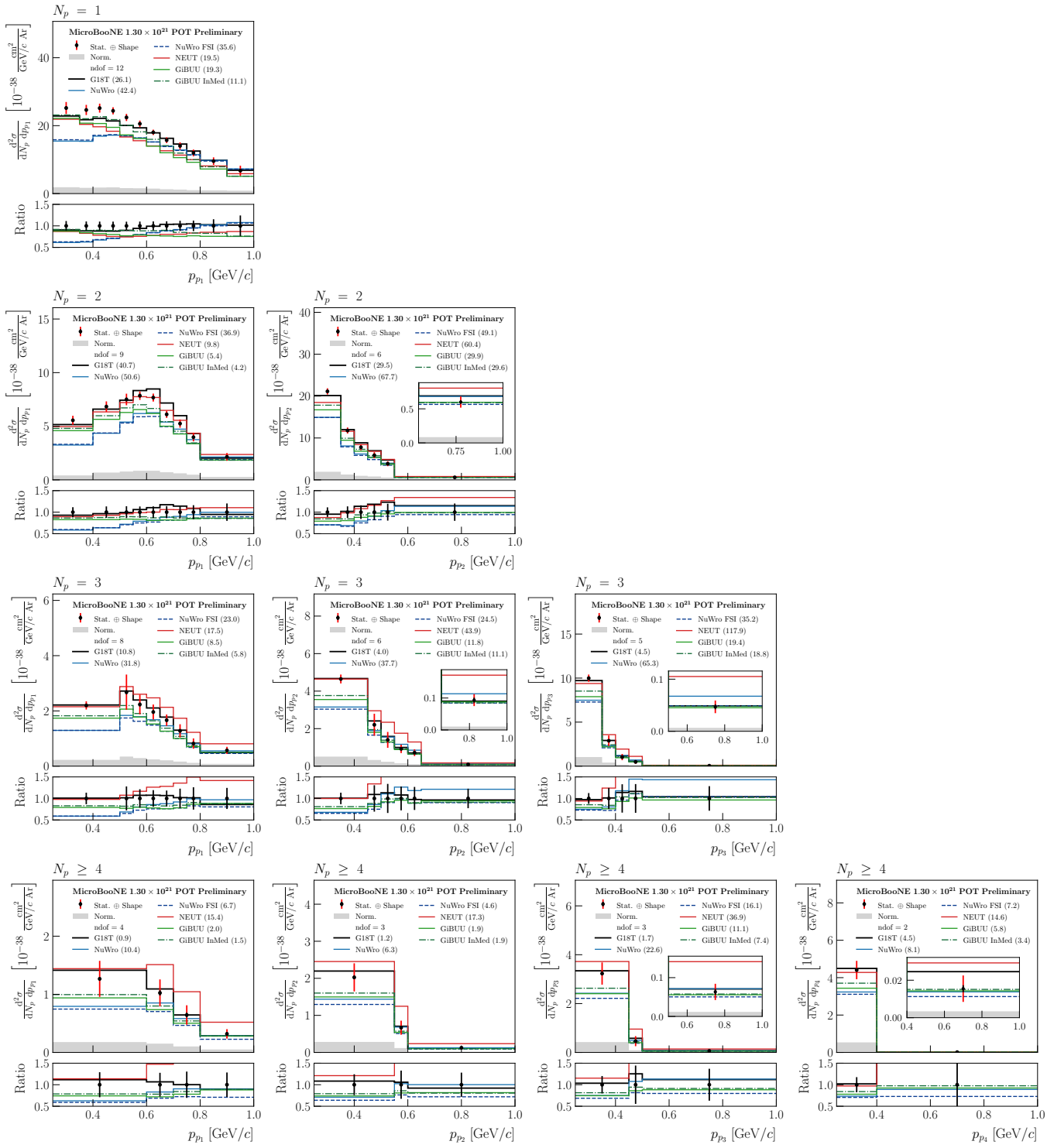

FIG. 14. Flux-integrated double-differential cross sections for blocks 4, 5, 6, and 7 (N_p, p_{p_i}), extracted from the full MicroBooNE BNB dataset (black data points). Error bars indicate statistical and shape-only uncertainties, while the gray band indicates the normalization uncertainty. Predictions from the GENIE MicroBooNE tune, NuWro, NEUT, and GiBUU are overlaid as indicated in the legend. The χ^2 for each prediction is indicated in parentheses. The bottom panels show the ratio of the predictions to the unfolded data.

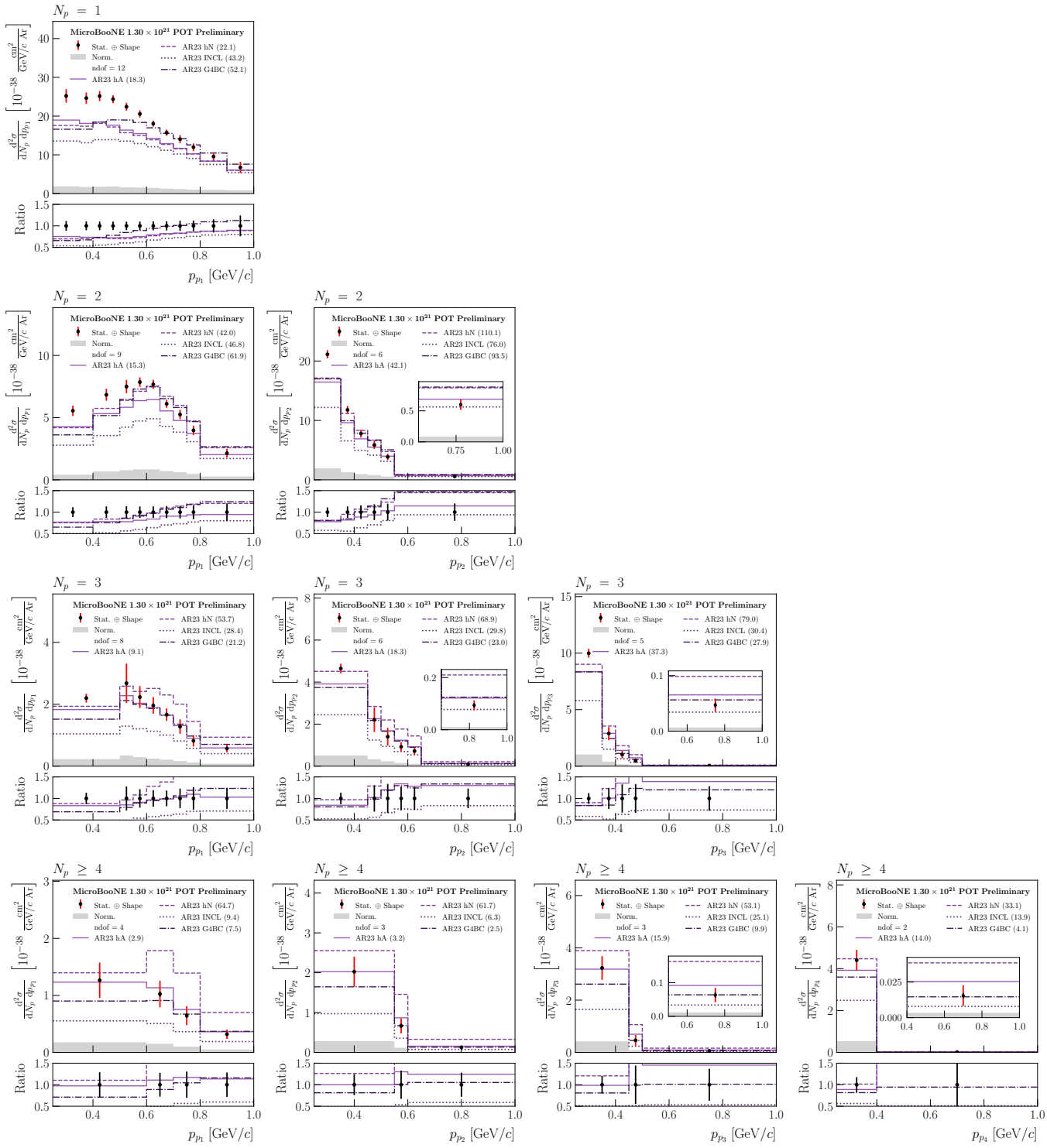

FIG. 15. Flux-integrated double-differential cross sections for blocks 4, 5, 6, and 7 (N_p, p_{p_i}), extracted from the full MicroBooNE BNB dataset (black data points). Error bars indicate statistical and shape-only uncertainties, while the gray band indicates the normalization uncertainty. Predictions from the GENIE `AR23` configuration with the hA, hN, INCL, and G4BC FSI models are overlaid as indicated in the legend. The χ^2 for each prediction is indicated in parentheses. The bottom panels show the ratio of the predictions to the unfolded data.

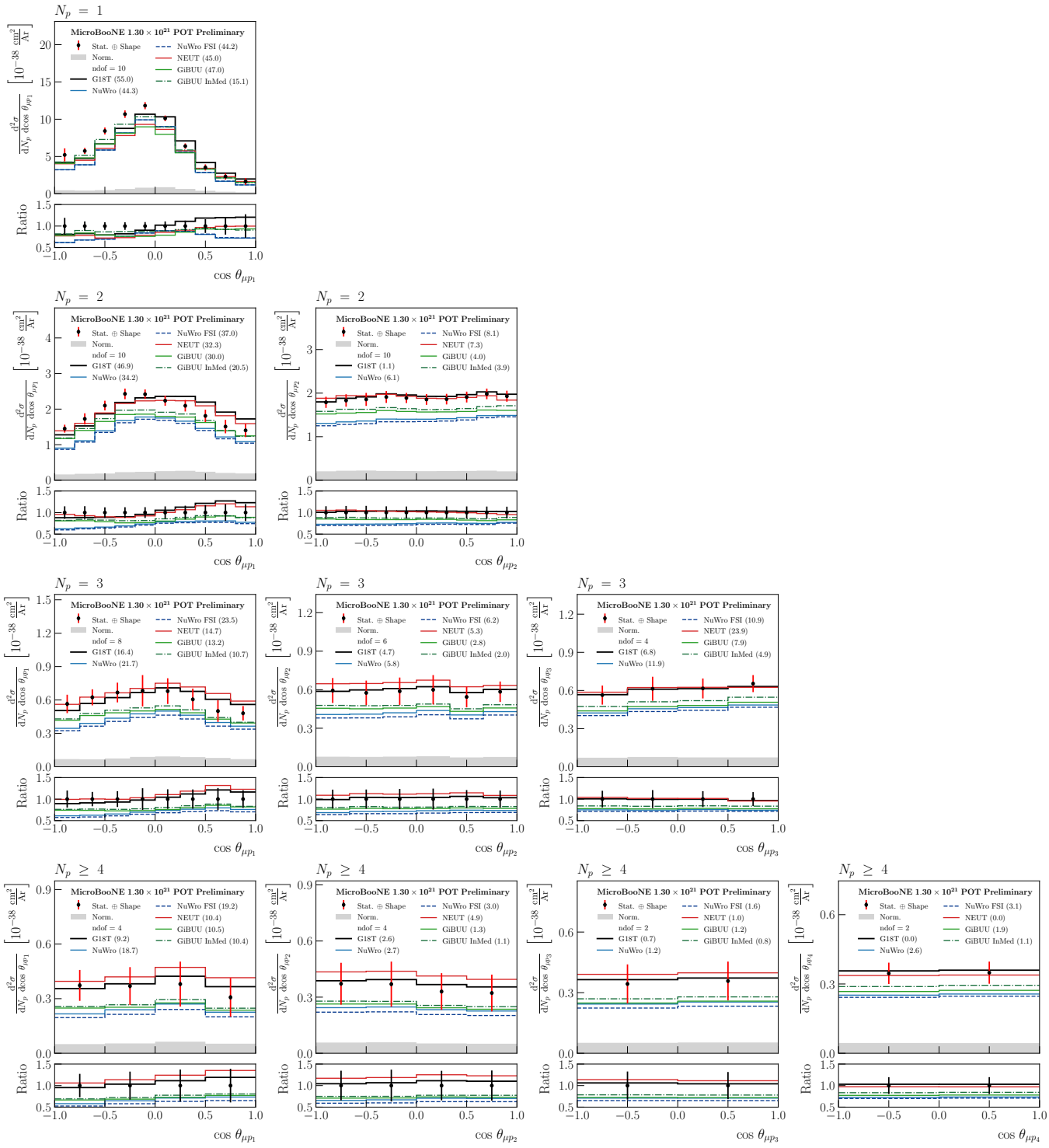

FIG. 16. Flux-integrated double-differential cross sections for blocks 8, 9, 10, and 11 (N_p, $\cos\theta_{\mu p_i}$), extracted from the full MicroBooNE BNB dataset (black data points). Error bars indicate statistical and shape-only uncertainties, while the gray band indicates the normalization uncertainty. Predictions from the GENIE MicroBooNE tune, NuWro, NEUT, and GiBUU are overlaid as indicated in the legend. The χ^2 for each prediction is indicated in parentheses. The bottom panels show the ratio of the predictions to the unfolded data.

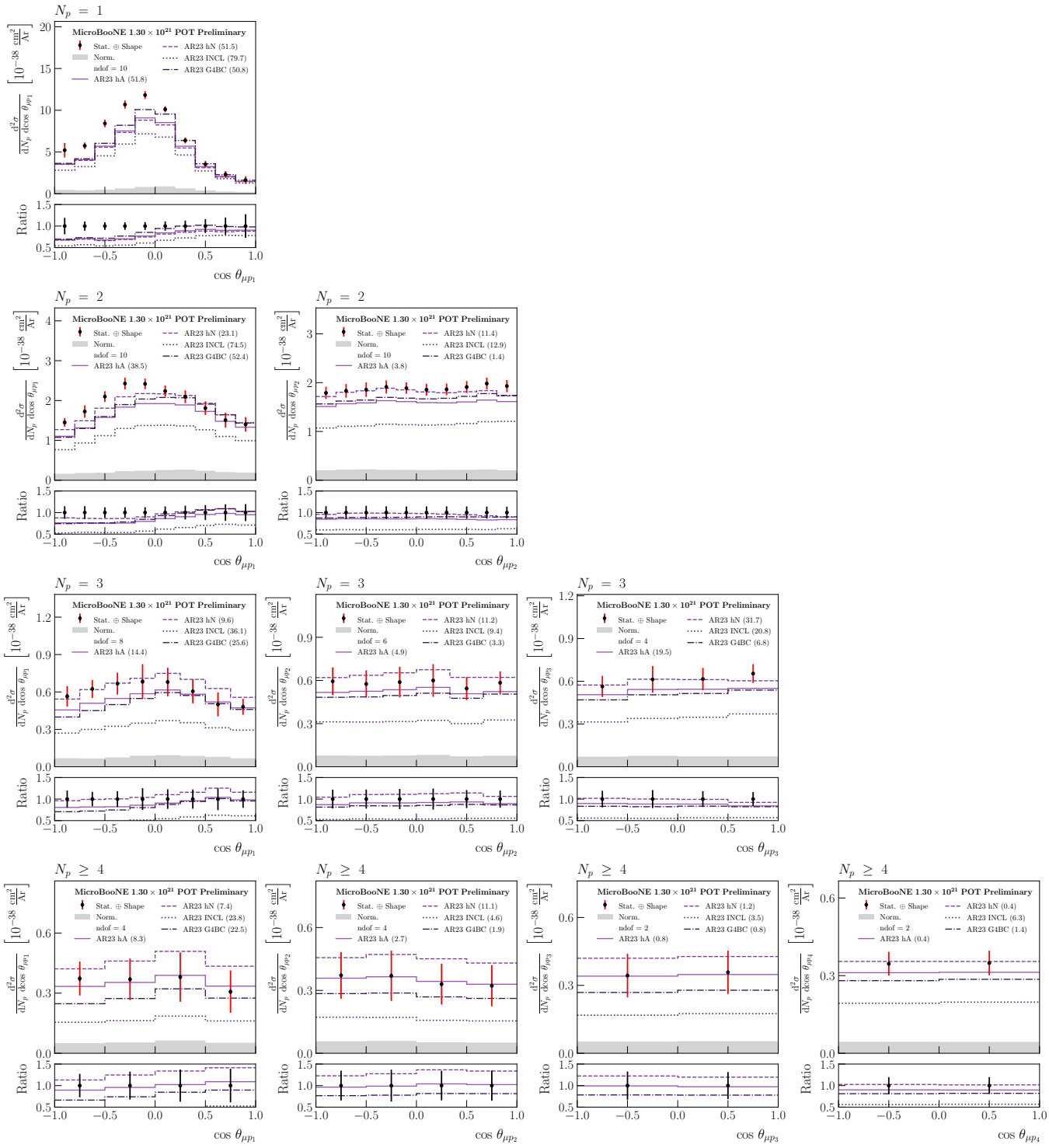

FIG. 17. Flux-integrated double-differential cross sections for blocks 8, 9, 10, and 11 (N_p, $\cos\theta_{\mu p_i}$), extracted from the full MicroBooNE BNB dataset (black data points). Error bars indicate statistical and shape-only uncertainties, while the gray band indicates the normalization uncertainty. Predictions from the GENIE `AR23` configuration with the hA, hN, INCL, and G4BC FSI models are overlaid as indicated in the legend. The χ^2 for each prediction is indicated in parentheses. The bottom panels show the ratio of the predictions to the unfolded data.

TABLE IV. Summary of the χ^2 values obtained for each bin block and globally for the GENIE MicroBooNE tune, NuWro (without and with fine-tuned FSI), NEUT, and GiBUU (without and with in-medium corrections) predictions compared to the unfolded cross-section data.

Block	ndof	GENIE uB Tune	NuWro `v25.11`		NEUT `v5.6.2`	GiBUU `2025`	
			Default	FSI		Default	InMed
1: (p_{p_1}, N_p)	27	121.30	95.30	69.76	206.18	45.88	25.33
2: $(\cos\theta_{\mu p_1}, N_p)$	20	80.20	57.51	63.30	78.41	40.26	27.73
3: (E_{avail}, N_p)	12	42.21	47.26	28.50	133.01	33.51	25.20
4: (N_p, p_{p_1})	33	136.90	81.27	62.78	221.54	48.95	29.96
5: (N_p, p_{p_2})	15	47.62	111.58	74.75	143.05	46.09	47.39
6: (N_p, p_{p_3})	8	7.56	73.93	40.42	120.97	23.06	23.09
7: (N_p, p_{p_4})	2	4.54	8.08	7.17	14.64	5.77	3.38
8: $(N_p, \cos\theta_{\mu p_1})$	32	87.20	88.64	91.59	102.99	68.23	42.66
9: $(N_p, \cos\theta_{\mu p_2})$	20	9.90	12.86	13.44	29.39	9.51	9.29
10: $(N_p, \cos\theta_{\mu p_3})$	6	7.59	12.13	11.14	25.12	8.15	5.36
11: $(N_p, \cos\theta_{\mu p_4})$	2	0.03	2.55	3.11	0.05	1.86	1.14
Global	145	569.9	692.5	585.3	1132.0	480.9	428.8

TABLE V. Summary of the χ^2 values obtained for each bin block and globally for the GENIE `AR23` configuration predictions using the hA, hN, INCL, and G4BC FSI models compared to the unfolded cross-section data.

Block	ndof	`AR23_20i`	`AR23_20j`	`AR23_20k`	`AR23_20l`
1: (p_{p_1}, N_p)	27	97.77	370.76	77.18	142.73
2: $(\cos\theta_{\mu p_1}, N_p)$	20	77.87	103.68	117.52	71.08
3: (E_{avail}, N_p)	12	62.15	243.69	60.78	114.63
4: (N_p, p_{p_1})	33	90.45	388.50	91.07	142.94
5: (N_p, p_{p_2})	15	60.67	236.52	102.95	139.05
6: (N_p, p_{p_3})	8	39.13	91.29	33.59	33.27
7: (N_p, p_{p_4})	2	14.00	33.07	13.88	4.11
8: $(N_p, \cos\theta_{\mu p_1})$	32	88.16	113.59	125.82	93.06
9: $(N_p, \cos\theta_{\mu p_2})$	20	18.85	41.16	18.47	8.49
10: $(N_p, \cos\theta_{\mu p_3})$	6	21.89	36.91	22.33	7.20
11: $(N_p, \cos\theta_{\mu p_4})$	2	0.36	0.37	6.32	1.37
Global	145	488.1	1200.6	685.3	822.0

the bin construction, 38 constrained degrees of freedom are identified, reducing the effective ndof for data-model comparisons from 183 to 145. The range-projected χ^2 test statistic of Ref. [75], described in Appendix E, accounts for these constraints when computing global goodness-of-fit across blocks. The global χ^2 values are reported in Tables IV and V alongside the per-block results. GiBUU InMed achieves the best global agreement ($\chi^2/\text{ndof} = 428.8/145$), followed by the default GiBUU (480.9/145), and the GENIE `AR23` hA configuration (488.1/145). The global ranking is consistent with the block-by-block observations. The predictions using the BUU transport framework provide the most complete description of the data, while NEUT and the hN cascade show the largest overall tension. Among the FSI variants, the global χ^2 spans from 488.1 (hA) to 1200.6 (hN), quantifying the strong FSI model sensitivity observed throughout the individual blocks. Notably, no generator achieves a statistically acceptable description of the full dataset, underscoring the need for continued refinement of hadronic transport models on argon.

V. SUMMARY AND CONCLUSIONS

This analysis presents the first measurement of proton multiplicity and leading and subleading proton kinematics in charged-current ν_μ interactions on argon producing no mesons and one or more protons in the final state. We report flux-integrated double-differential cross-section measurements in proton multiplicity, momenta and opening angles for the first four protons, ordered by momentum, and available energy. The analysis uses the full MicroBooNE Booster Neutrino Beam dataset. The blockwise approach from Ref. [34] is adopted, allowing the simultaneous reporting of all distributions with their full cross-block correlations.

The extracted cross sections are compared to predictions from several neutrino event generators. Overall, GiBUU 2025 with in-medium corrections to the nucleon-nucleon cross sections [66] provides the best description of the data at the block level and globally. However, no generator achieves an adequate description of the full dataset, indicating that significant modeling deficiencies remain. The measurement reveals strong sensitivity to the treatment of intra-nuclear hadron propagation, as demonstrated by the wide spread in χ^2 values across the GENIE AR23 configuration FSI variants. A backward-angle $N_p = 1$ deficit appears to be a persistent feature that challenges all generators, suggesting a common deficiency in modeling single-proton final states at wide muon-proton opening angles. The systematic underprediction at low momenta for NuWro and the overprediction of multi-proton events at high energies seen in NEUT point to complementary deficiencies in the treatment of low-energy proton production and cascade strength.

Using the full MicroBooNE statistics, this study complements and updates the previous CC0πNp measurement [9] focused on muon-proton correlations. Together, they offer a more complete picture of the hadronic final state in neutrino-argon scattering. The reported measurements provide direct input for the interaction modeling needs of the SBN and DUNE programs, and the comprehensive data release enables the generator community to use them for tuning and validation.

VI. ACKNOWLEDGEMENTS

This document was prepared by the MicroBooNE collaboration using the resources of the Fermi National Accelerator Laboratory (Fermilab), a U.S. Department of Energy, Office of Science, Office of High Energy Physics HEP User Facility. Fermilab is managed by Fermi Forward Discovery Group, LLC, acting under Contract No. 89243024CSC000002. MicroBooNE is supported by the following: the U.S. Department of Energy, Office of Science, Offices of High Energy Physics and Nuclear Physics; the U.S. National Science Foundation; the Swiss National Science Foundation; the Science and Technology Facilities Council (STFC), part of United Kingdom Research and Innovation (UKRI); the Royal Society (United Kingdom); the UKRI Future Leaders Fellowship; the NSF AI Institute for Artificial Intelligence and Fundamental Interactions; and the European Union's Horizon 2020 research and innovation programme under the Marie Skłodowska-Curie grant agreement No. 101003460 (PROBES). Additional support for the laser calibration system and cosmic ray tagger was provided by the Albert Einstein Center for Fundamental Physics, Bern, Switzerland. We also acknowledge the contributions of technical and scientific staff to the design, construction, and operation of the MicroBooNE detector as well as the contributions of past collaborators to the development of MicroBooNE analyses, without whom this work would not have been possible. For the purpose of open access, the authors have applied a Creative Commons Attribution (CC BY) public copyright license to any Author Accepted Manuscript version arising from this submission.

Appendix A: Bin definitions

Table VI presents the binning scheme used in the analysis, organized in blocks representing the same kinematic distributions. For each bin, the corresponding selection efficiency and diagonal entry in the migration matrix are also reported.

TABLE VI: Bin definitions used in the analysis.

Block 1: (p_{p_1}, N_p)

Global bin number	$p_{p_1}^{\text{low}}$ (GeV/c)	$p_{p_1}^{\text{high}}$ (GeV/c)	N_p	Efficiency	Migration diagonal
0	0.250	0.375	1	0.747	0.870
1			≥ 2	0.617	0.301
2	0.375	0.475	1	0.678	0.720
3			2	0.495	0.407
4			≥ 3	0.408	0.229
5	0.475	0.575	1	0.712	0.729
6			2	0.534	0.502
7			3	0.393	0.251
8			≥ 4	0.324	0.174
9	0.575	0.650	1	0.728	0.708
10			2	0.562	0.521
11			3	0.372	0.262
12			≥ 4	0.275	0.195
13	0.650	0.725	1	0.699	0.672
14			2	0.522	0.489
15			3	0.329	0.255
16			≥ 4	0.245	0.230
17	0.725	0.800	1	0.677	0.627
18			2	0.447	0.441
19			3	0.263	0.291
20			≥ 4	0.192	0.197
21	0.800	0.850	1	0.659	0.575
22			2	0.353	0.382
23			≥ 3	0.173	0.304
24	0.850	1.000	1	0.646	0.688
25			2	0.246	0.449
26			≥ 3	0.096	0.358

Block 2: ($\cos\theta_{\mu p_1}$, N_p)

Global bin number	$\cos\theta_{\mu p_1}^{\text{low}}$	$\cos\theta_{\mu p_1}^{\text{high}}$	N_p	Efficiency	Migration diagonal
27	-1.000	-0.850	1	0.326	0.714
28			2	0.263	0.459
29			≥ 3	0.174	0.251
30	-0.850	-0.650	1	0.628	0.706
31			2	0.425	0.423
32			≥ 3	0.249	0.253
33	-0.650	0.000	1	0.736	0.834
34			2	0.432	0.485

35			3	0.268	0.232
36			≥ 4	0.159	0.169
37	0.000	0.650	1	0.773	0.808
38			2	0.453	0.545
39			3	0.245	0.254
40			≥ 4	0.133	0.165
41	0.650	0.850	1	0.666	0.592
42			2	0.487	0.483
43			≥ 3	0.219	0.284
44	0.850	1.000	1	0.560	0.534
45			2	0.389	0.412
46			≥ 3	0.168	0.231

Block 3: (E_{avail}, N_p)

Global bin number	$E_{\text{avail}}^{\text{low}}$ (GeV)	$E_{\text{avail}}^{\text{high}}$ (GeV)	N_p	Efficiency	Migration diagonal
47	0.030	0.125	1	0.711	0.939
48			≥ 2	0.632	0.188
49	0.125	0.285	1	0.708	0.783
50			2	0.533	0.482
51			≥ 3	0.465	0.150
52	0.285	0.400	1	0.656	0.623
53			2	0.501	0.473
54			≥ 3	0.355	0.150
55	0.400	10.00	1	0.272	0.546
56			2	0.162	0.457
57			3	0.125	0.328
58			≥ 4	0.105	0.215

Block 4: (N_p, p_{p_1})

Global bin number	N_p	$p_{p_1}^{\text{low}}$ (GeV/c)	$p_{p_1}^{\text{high}}$ (GeV/c)	Efficiency	Migration diagonal
59	1	0.250	0.350	0.760	0.819
60		0.350	0.400	0.701	0.513
61		0.400	0.450	0.677	0.575
62		0.450	0.500	0.679	0.598
63		0.500	0.550	0.714	0.661
64		0.550	0.600	0.731	0.666
65		0.600	0.650	0.724	0.659
66		0.650	0.700	0.706	0.634
67		0.700	0.750	0.686	0.605
68		0.750	0.800	0.669	0.578
69		0.800	0.900	0.662	0.658
70		0.900	1.000	0.627	0.620
71	2	0.250	0.400	0.599	0.282
72		0.400	0.500	0.491	0.438

73		0.500	0.550	0.535	0.436
74		0.550	0.600	0.558	0.463
75		0.600	0.650	0.561	0.477
76		0.650	0.700	0.528	0.458
77		0.700	0.750	0.491	0.433
78		0.750	0.800	0.431	0.404
79		0.800	1.000	0.287	0.465
80	3	0.250	0.500	0.447	0.174
81		0.500	0.550	0.386	0.227
82		0.550	0.600	0.412	0.224
83		0.600	0.650	0.343	0.235
84		0.650	0.700	0.333	0.234
85		0.700	0.750	0.309	0.270
86		0.750	0.800	0.242	0.262
87		0.800	1.000	0.135	0.301
88	≥ 4	0.250	0.600	0.323	0.150
89		0.600	0.700	0.262	0.215
90		0.700	0.800	0.200	0.210
91		0.800	1.000	0.085	0.234

Block 5: (N_p, p_{p_2})

Global bin number	N_p	$p_{p_2}^{\text{low}}$ (GeV/c)	$p_{p_2}^{\text{high}}$ (GeV/c)	Efficiency	Migration diagonal
92	< 2			0.693	0.952
93	2	0.250	0.350	0.560	0.343
94		0.350	0.400	0.446	0.336
95		0.400	0.450	0.387	0.390
96		0.450	0.500	0.382	0.414
97		0.500	0.550	0.394	0.463
98		0.550	1.000	0.203	0.545
99	3	0.250	0.450	0.369	0.202
100		0.450	0.500	0.240	0.227
101		0.500	0.550	0.236	0.280
102		0.550	0.600	0.179	0.328
103		0.600	0.650	0.121	0.287
104		0.650	1.000	0.033	0.325
105	≥ 4	0.250	0.550	0.238	0.174
106		0.550	0.600	0.134	0.215
107		0.600	1.000	0.030	0.275

Block 6: (N_p, p_{p_3})

Global bin number	N_p	$p_{p_3}^{\text{low}}$ (GeV/c)	$p_{p_3}^{\text{high}}$ (GeV/c)	Efficiency	Migration diagonal
108	< 3			0.610	0.990
109	3	0.250	0.350	0.357	0.173
110		0.350	0.400	0.207	0.205

111		0.400	0.450	0.162	0.301
112		0.450	0.500	0.101	0.229
113		0.500	1.000	0.044	0.326
114	≥ 4	0.250	0.450	0.214	0.160
115		0.450	0.500	0.100	0.171
116		0.500	1.000	0.030	0.311

Block 7: (N_p, p_{p_4})

Global bin number	N_p	$p_{p_4}^{\text{low}}$ (GeV/c)	$p_{p_4}^{\text{high}}$ (GeV/c)	Efficiency	Migration diagonal
117	< 4			0.578	0.999
118	≥ 4	0.250	0.400	0.190	0.165
119		0.400	1.000	0.037	0.241

Block 8: (N_p, $\cos\theta_{\mu p_1}$)

Global bin number	N_p	$\cos\theta_{\mu p_1}^{\text{low}}$	$\cos\theta_{\mu p_1}^{\text{high}}$	Efficiency	Migration diagonal
120	1	-1.000	-0.800	0.365	0.764
121		-0.800	-0.600	0.641	0.702
122		-0.600	-0.400	0.682	0.658
123		-0.400	-0.200	0.738	0.659
124		-0.200	0.000	0.776	0.661
125		0.000	0.200	0.788	0.657
126		0.200	0.400	0.784	0.631
127		0.400	0.600	0.737	0.612
128		0.600	0.800	0.678	0.595
129		0.800	1.000	0.587	0.583
130	2	-1.000	-0.800	0.300	0.483
131		-0.800	-0.600	0.427	0.388
132		-0.600	-0.400	0.450	0.400
133		-0.400	-0.200	0.430	0.368
134		-0.200	0.000	0.418	0.370
135		0.000	0.200	0.422	0.399
136		0.200	0.400	0.453	0.427
137		0.400	0.600	0.481	0.457
138		0.600	0.800	0.487	0.472
139		0.800	1.000	0.417	0.440
140	3	-1.000	-0.750	0.226	0.209
141		-0.750	-0.500	0.283	0.200
142		-0.500	-0.250	0.265	0.173
143		-0.250	0.000	0.268	0.196
144		0.000	0.250	0.248	0.204
145		0.250	0.500	0.238	0.194
146		0.500	0.750	0.254	0.236
147		0.750	1.000	0.223	0.225
148	≥ 4	-1.000	-0.500	0.146	0.160

149		-0.500	0.000	0.156	0.152
150		0.000	0.500	0.135	0.156
151		0.500	1.000	0.119	0.169

Block 9: (N_p, $\cos\theta_{\mu p_2}$)

Global bin number	N_p	$\cos\theta^{\text{low}}_{\mu p_2}$	$\cos\theta^{\text{high}}_{\mu p_2}$	Efficiency	Migration diagonal
152	< 2			0.693	0.952
153	2	-1.000	-0.800	0.434	0.484
154		-0.800	-0.600	0.533	0.391
155		-0.600	-0.400	0.511	0.346
156		-0.400	-0.200	0.468	0.337
157		-0.200	0.000	0.426	0.315
158		0.000	0.200	0.393	0.290
159		0.200	0.400	0.395	0.315
160		0.400	0.600	0.400	0.324
161		0.600	0.800	0.420	0.344
162		0.800	1.000	0.379	0.289
163	3	-1.000	-0.666	0.257	0.167
164		-0.666	-0.333	0.327	0.187
165		-0.333	-0.000	0.253	0.164
166		0.000	0.333	0.237	0.179
167		0.333	0.666	0.237	0.171
168		0.666	1.000	0.213	0.166
169	≥ 4	-1.000	-0.500	0.153	0.124
170		-0.500	0.000	0.155	0.120
171		0.000	0.500	0.141	0.136
172		0.500	1.000	0.113	0.130

Block 10: (N_p, $\cos\theta_{\mu p_3}$)

Global bin number	N_p	$\cos\theta^{\text{low}}_{\mu p_3}$	$\cos\theta^{\text{high}}_{\mu p_3}$	Efficiency	Migration diagonal
173	< 3			0.610	0.990
174	3	-1.000	-0.500	0.266	0.226
175		-0.500	0.000	0.268	0.166
176		0.000	0.500	0.251	0.168
177		0.500	1.000	0.217	0.139
178	≥ 4	-1.000	0.000	0.150	0.145
179		0.000	1.000	0.126	0.140

Block 11: (N_p, $\cos\theta_{\mu p_4}$)

Global bin number	N_p	$\cos\theta^{\text{low}}_{\mu p_4}$	$\cos\theta^{\text{high}}_{\mu p_4}$	Efficiency	Migration diagonal
180	< 4			0.578	0.999
181	≥ 4	-1.000	0.000	0.149	0.141

182	0.000	1.000	0.126	0.130

Appendix B: Data-driven response matrix validation

The detector response matrix used in the cross-section extraction depends on the simulated proton kinematics, including those of the subleading protons near the reconstruction threshold. If our simulation mismodels the proton kinematics, the response matrix may be incorrect, potentially biasing the unfolded results. To assess the sensitivity to this effect, a data-driven validation is performed in which alternative response matrices are constructed from resimulated data and MC events.

Selected data and MC events are resimulated using the reconstructed muon and proton momenta as inputs to the full simulation and reconstruction chain. Each event is reprocessed multiple times, with the vertex position randomized within the fiducial volume and the three-momenta rotated about the beam axis to sample the detector response more broadly. Since the resimulated samples are constructed from events that already passed the selection, they are biased towards the reconstructable region of phase space and therefore cannot be used to estimate the selection efficiency. Thus, the resimulated response matrices are built by combining the migration matrices from the resimulation with the efficiency from the central-value MC

$$\Delta_{i\mu}^{\mathrm{resim}} = \epsilon_{\mu}^{\mathrm{CV}}\, M_{i\mu}^{\mathrm{resim}}, \tag{B1}$$

where the resimulated migration matrix is given by

$$M_{i\mu}^{\mathrm{resim}} = \frac{\varphi_{i\mu}^{\mathrm{resim}}}{\sum_j \varphi_{j\mu}^{\mathrm{resim}}}, \tag{B2}$$

with $\varphi_{i\mu}^{\mathrm{resim}}$ being the number of selected events after resimulation simultaneously falling in resimulated reconstructed bin i and original reconstructed bin μ.

The resimulated data and MC response matrices are each used to unfold central-value fake data. The statistical uncertainty on the unfolded result arising from the finite resimulation statistics is propagated through the D'Agostini unfolding via the 3-dimensional Jacobian tensor

$$j_{i\nu}^{\mu\,(n+1)} = \frac{\partial \hat{\varphi}_{\mu}^{(n+1)}}{\partial \Delta_{i\nu}^{\mathrm{resim}}} = \sum_j \frac{\partial U_{j\mu}^{(n)}}{\partial \Delta_{i\nu}^{\mathrm{resim}}}\, d_j. \tag{B3}$$

Since the resimulated response matrix entries follow multinomial statistics, their covariance is

$$\mathrm{Cov}(\Delta_{i\mu}^{\mathrm{resim}},\, \Delta_{j\mu}^{\mathrm{resim}}) = \frac{\delta_{ij}\, \Delta_{i\mu}^{\mathrm{resim}} - \Delta_{i\mu}^{\mathrm{resim}}\, \Delta_{j\mu}^{\mathrm{resim}}}{\varphi_{\mu}^{\mathrm{resim}}}. \tag{B4}$$

The final comparison tests whether the fake data unfolded with the data- and MC-derived response matrices are compatible. The contribution of the response matrix to the statistical covariance between the unfolded event counts in the μ-th and ν-th true bins is given by

$$V_{\mu\nu}^{\mathrm{respmat}} = \sum_{\alpha} \sum_{i,j} j_{i\alpha}^{\mu}\, \mathrm{Cov}(\Delta_{i\alpha}^{\mathrm{resim}},\, \Delta_{j\alpha}^{\mathrm{resim}})\, j_{j\alpha}^{\nu}. \tag{B5}$$

The covariance of the difference is the sum of the individual response matrix uncertainties, $C_{\Delta} = V_{\mathrm{MC}}^{\mathrm{respmat}} + V_{\mathrm{data}}^{\mathrm{respmat}}$. To account for differences in regularization between the two unfoldings, the residuals are corrected using the respective additional smearing matrices

$$\delta_{\mathrm{bias}} = (A_C^{\mathrm{MC}} - A_C^{\mathrm{data}})\, \varphi^{\mathrm{CV}}. \tag{B6}$$

The χ^2 for the comparison is then

$$\chi^2 = (\Delta\hat{\varphi}^{\mathrm{resim}} - \delta_{\mathrm{bias}})^{\mathsf{T}}\, C_{\Delta}^{-1}\, (\Delta\hat{\varphi}^{\mathrm{resim}} - \delta_{\mathrm{bias}}). \tag{B7}$$

It should be noted that the resimulated response matrices represent a mapping between original reconstructed and resimulated reconstructed bins, rather than the usual truth-to-reconstructed transformation. This approximation affects both the data and MC resimulated response matrices equally, so the comparison between the two remains a valid test of sensitivity to differences in proton kinematics between data and simulation.

Appendix C: Sideband-based background validation

Cross-section extraction methods that rely on MC predictions for background subtraction are sensitive to the accuracy of the background model. When a discrepancy between data and prediction is observed in the selected sample, it is important to determine whether it originates from mismodeling of the signal, the background, or both. Here, we outline a general procedure to disentangle these two contributions using a background-enhanced sideband selection. In this analysis, this method is applied to the leading proton opening angle distributions (bin blocks 2 and 8), which show significant tension between data and MC.

In each bin, the data in the selection and sideband regions can be modeled as

$$\begin{aligned} D_i^{\text{sel}} &= \alpha_i \, \varphi_i^{\text{sel}} + \beta_i \, b_i^{\text{sel}}, \\ D_i^{\text{sb}} &= \alpha_i \, \varphi_i^{\text{sb}} + \beta_i \, b_i^{\text{sb}}, \end{aligned} \tag{C1}$$

where α_i and β_i are bin-dependent correction factors for signal and background events respectively, the superscripts denote the region (selection or sideband), D_i is the total number of measured events, φ_i is the expected number of selected signal events, and b_i is the total number of expected background events (both beam-off and beam-correlated backgrounds) for bin i. The key assumption is that the correction factors are properties of the underlying physics modeling and are therefore the same in both regions.

The solution in each bin can be written in matrix form as

$$\begin{pmatrix} \alpha_i - 1 \\ \beta_i - 1 \end{pmatrix} = \begin{pmatrix} \varphi_i^{\text{sel}} & b_i^{\text{sel}} \\ \varphi_i^{\text{sb}} & b_i^{\text{sb}} \end{pmatrix}^{-1} \begin{pmatrix} D_i^{\text{sel}} - n_i^{\text{sel}} \\ D_i^{\text{sb}} - n_i^{\text{sb}} \end{pmatrix}, \tag{C2}$$

where $n_i = \varphi_i + b_i$ denotes the total number of predicted events in bin i. The covariance matrices for α_i and β_i are obtained from the total covariance matrix (data plus prediction) and the Jacobian elements determined by the inverse matrix in the linear system.

The null hypothesis is that the background is correctly modeled, i.e. $\beta_i = 1$ for all bins, and that all observed discrepancy between data and MC is due to signal mismodeling alone. This is tested with a χ^2 statistic

$$\chi^2 = \sum_{i,\,j} (\beta_i - 1) \; \text{Cov}(\beta_i, \, \beta_j)^{-1} \; (\beta_j - 1) \, . \tag{C3}$$

Under the null hypothesis, this statistic follows a χ^2 distribution with N_{bins} degrees of freedom, where N_{bins} is the number of bins in the block.

Appendix D: Covariance matrix decomposition

Given a histogram ϕ with an associated covariance matrix C not including statistical uncertainties, this matrix can be decomposed into separate normalization, shape, and mixed contributions following the decomposition [9]:

$$C_{ij} = C_{ij}^{\text{norm}} + C_{ij}^{\text{shape}} + C_{ij}^{\text{mixed}}, \tag{D1}$$

$$C_{ij}^{\text{norm}} = \frac{\phi_i \, \phi_j}{\phi_{\text{tot}}^2} \sum_{k,l} C_{kl}, \tag{D2}$$

$$C_{ij}^{\text{shape}} = C_{ij} - \frac{\phi_j}{\phi_{\text{tot}}} \sum_k C_{ik} - \frac{\phi_i}{\phi_{\text{tot}}} \sum_k C_{kj} + C_{ij}^{\text{norm}}, \tag{D3}$$

$$C_{ij}^{\text{mixed}} = \frac{\phi_j}{\phi_{\text{tot}}} \sum_k C_{ik} + \frac{\phi_i}{\phi_{\text{tot}}} \sum_k C_{kj} - 2 \, C_{ij}^{\text{norm}}, \tag{D4}$$

where $\phi_{\text{tot}} = \sum_i \phi_i$ is the sum of all the entries in the histogram.

The normalization covariance matrix is related to uncertainties which change the histogram by the same overall factor. The shape matrix is associated with effects that keep the total number of entries constant. The mixed matrix captures the correlation between the overall normalization and the bin-dependent shape variations.

Appendix E: Range-projected χ^2 test statistic

The combined measurement approach proposed in Ref. [34] introduces event sharing between bins across different distribution blocks. This sharing structure can be encoded in a combination matrix Ω that represents all bin configurations allowed by the measurement structure. The null space of Ω defines N_{null} exact linear constraints on the bin counts. These constraints render the statistical covariance matrix rank-deficient. A standard χ^2 test cannot reliably be applied to the full bin vector without addressing these degenerate directions.

The range-projected χ^2 test statistic of Ref. [75] solves this by restricting the test to the subspace where independent statistical information exists. The construction proceeds as follows. The combination matrix Ω is built in reconstructed space from the bin scheme used in the measurement. The eigendecomposition of $\Omega^{\mathsf{T}}\Omega$ yields $r = \text{rank}(\Omega)$ nonzero eigenvalues, whose associated eigenvectors V_r span the non-null subspace. These are the directions along which the measurement has independent statistical sensitivity. The projection is performed in reconstructed space, before unfolding, to avoid contamination from null-space components that would otherwise leak into the range through the non-orthogonal unfolding matrix. Given a reconstructed-space residual vector $r = d - \Delta\,\varphi_{\text{pred}}$ with an associated total covariance matrix C_{total}, the projected χ^2 is computed as

$$\chi^2_{\text{proj}} = \tilde{r}^{\,\mathsf{T}}\,\tilde{C}^{-1}_{\text{total}}\,\tilde{r}, \tag{E1}$$

where $\tilde{r} = V_r^{\mathsf{T}}\,r$ is the projected residual vector and $\tilde{C}_{\text{total}} = V_r^{\mathsf{T}}\,C_{\text{total}}\,V_r$ is the $r \times r$ reduced covariance matrix. The matrix $\tilde{C}_{\text{total}}$ is full-rank and can be inverted with standard methods. Under the null hypothesis, this test statistic follows a χ^2 distribution with r degrees of freedom. This test statistic is invariant under unfolding. The reduced system is full-rank, so the standard χ^2 invariance under invertible linear transformations applies.

[1] B. Abi *et al.* (DUNE Collaboration), Deep Underground Neutrino Experiment (DUNE), Far Detector Technical Design Report, Volume I Introduction to DUNE, J. Instrum. **15**, T08008 (2020), arXiv:2002.02967 [physics.ins-det].

[2] P. F. De Salas, S. Gariazzo, O. Mena, C. A. Ternes, and M. Tórtola, Neutrino Mass Ordering from Oscillations and Beyond: 2018 Status and Future Prospects, Front. Astron. Space Sci. **5**, 36 (2018), arXiv:1806.11051 [hep-ph].

[3] G. C. Branco, R. G. Felipe, and F. R. Joaquim, Leptonic CP Violation, Rev. Mod. Phys. **84**, 515 (2012), arXiv:1111.5332 [hep-ph].

[4] P. A. Machado, O. Palamara, and D. W. Schmitz, The Short-Baseline Neutrino Program at Fermilab, Ann. Rev. Nucl. Part. Sci. **69**, 363 (2019), arXiv:1903.04608 [hep-ex].

[5] M. A. Acero *et al.*, White paper on light sterile neutrino searches and related phenomenology, J. Phys. G **51**, 120501 (2024), arXiv:2203.07323 [hep-ex].

[6] A. Diaz, C. A. Argüelles, G. H. Collin, J. M. Conrad, and M. H. Shaevitz, Where Are We With Light Sterile Neutrinos?, Phys. Rept. **884**, 1 (2020), arXiv:1906.00045 [hep-ex].

[7] C. Rubbia, The Liquid Argon Time Projection Chamber: A New Concept for Neutrino Detectors (1977), CERN-EP-INT-77-08.

[8] K. Majumdar and K. Mavrokoridis, Review of Liquid Argon Detector Technologies in the Neutrino Sector, Appl. Sciences **11**, 2455 (2021), arXiv:2103.06395 [physics.ins-det].

[9] P. Abratenko *et al.* (MicroBooNE Collaboration), Measurement of single- and double-differential cross sections for mesonless charged-current muon neutrino interactions on argon with final-state protons using the MicroBooNE detector, Phys. Rev. D **112**, 112004 (2025), arXiv:2403.19574 [hep-ex].

[10] I. Stancu *et al.*, Technical Design Report for the 8 GeV Beam (2001), FERMILAB-DESIGN-2001-03.

[11] R. Acciarri *et al.* (MicroBooNE Collaboration), Design and Construction of the MicroBooNE Detector, J. Instrum. **12**, P02017 (2017), arXiv:1612.05824 [physics.ins-det].

[12] A. A. Aguilar-Arevalo *et al.* (MiniBooNE Collaboration), The Neutrino Flux Prediction at MiniBooNE, Phys. Rev. D **79**, 072002 (2009), arXiv:0806.1449 [hep-ex].

[13] S. Agostinelli *et al.* (GEANT4 Collaboration), GEANT4 - A Simulation Toolkit, Nucl. Instrum. Meth. A **506**, 250 (2003).

[14] J. Allison *et al.*, Geant4 developments and applications, IEEE Trans. Nucl. Sci. **53**, 270 (2006).

[15] J. Allison *et al.*, Recent developments in Geant4, Nucl. Instrum. Meth. A **835**, 186 (2016).

[16] C. Andreopoulos *et al.*, The GENIE Neutrino Monte Carlo Generator, Nucl. Instrum. Meth. A **614**, 87 (2010), arXiv:0905.2517 [hep-ph].

[17] K. Abe *et al.* (T2K Collaboration), Measurement of double-differential muon neutrino charged-current interactions on C_8H_8 without pions in the final state using the T2K off-axis beam, Phys. Rev. D **93**, 112012 (2016), arXiv:1602.03652 [hep-ex].

[18] P. Abratenko *et al.* (MicroBooNE Collaboration), New CC0π GENIE model tune for MicroBooNE, Phys. Rev. D **105**, 072001 (2022), arXiv:2110.14028 [hep-ex].

[19] E. L. Snider and G. Petrillo, LArSoft: Toolkit for Simulation, Reconstruction and Analysis of Liquid Argon TPC Neutrino Detectors, J. Phys. Conf. Ser. **898**, 042057 (2017).

[20] R. Acciarri *et al.* (MicroBooNE Collaboration), Noise Characterization and Filtering in the MicroBooNE Liquid Argon TPC, J. Instrum. **12**, P08003 (2017), arXiv:1705.07341 [physics.ins-det].

[21] C. Adams *et al.* (MicroBooNE Collaboration), Ionization electron signal processing in single phase LArTPCs. Part I. Algorithm Description and quantitative evaluation with MicroBooNE simulation, J. Instrum. **13**, P07006 (2018), arXiv:1802.08709 [physics.ins-det].

[22] C. Adams *et al.* (MicroBooNE Collaboration), Ionization electron signal processing in single phase LArTPCs. Part II. Data/simulation comparison and performance in MicroBooNE, J. Instrum. **13**, P07007 (2018), arXiv:1804.02583 [physics.ins-det].

[23] C. Adams *et al.* (MicroBooNE Collaboration), A method to determine the electric field of liquid argon time projection chambers using a UV laser system and its application in MicroBooNE, J. Instrum. **15**, P07010 (2020), arXiv:1910.01430 [physics.ins-det].

[24] P. Abratenko *et al.* (MicroBooNE Collaboration), Measurement of space charge effects in the MicroBooNE LArTPC using cosmic muons, J. Instrum. **15**, P12037 (2020), arXiv:2008.09765 [physics.ins-det].

[25] P. Abratenko *et al.* (MicroBooNE Collaboration), Measurement of the longitudinal diffusion of ionization electrons in the MicroBooNE detector, J. Instrum. **16**, P09025 (2021), arXiv:2104.06551 [physics.ins-det].

[26] C. Adams *et al.* (MicroBooNE Collaboration), Rejecting cosmic background for exclusive charged current quasi elastic neutrino interaction studies with Liquid Argon TPCs; a case study with the MicroBooNE detector, Eur. Phys. J. C **79**, 673 (2019), arXiv:1812.05679 [physics.ins-det].

[27] J. S. Marshall and M. A. Thomson, The Pandora Software Development Kit for Pattern Recognition, Eur. Phys. J. C **75**, 439 (2015), arXiv:1506.05348 [physics.data-an].

[28] R. Acciarri *et al.* (MicroBooNE Collaboration), The Pandora multi-algorithm approach to automated pattern recognition of cosmic-ray muon and neutrino events in the MicroBooNE detector, Eur. Phys. J. C **78**, 82 (2018), arXiv:1708.03135 [hep-ex].

[29] C. Adams *et al.* (MicroBooNE Collaboration), Calibration of the charge and energy loss per unit length of the MicroBooNE liquid argon time projection chamber using muons and protons, J. Instrum. **15**, P03022 (2020), arXiv:1907.11736 [physics.ins-det].

[30] P. Abratenko *et al.* (MicroBooNE Collaboration), Calorimetric classification of track-like signatures in liquid argon TPCs using MicroBooNE data, J. High Energy Phys. **12**, 153 (2021), arXiv:2109.02460 [physics.ins-det].

[31] P. Abratenko *et al.* (MicroBooNE Collaboration), Determination of muon momentum in the MicroBooNE LArTPC using an improved model of multiple Coulomb scattering, J. Instrum. **12**, P10010 (2017), arXiv:1703.06187 [physics.ins-det].

[32] P. Abratenko *et al.* (MicroBooNE Collaboration), Measurement of differential cross sections for ν_μ -Ar charged-current interactions with protons and no pions in the final state with the MicroBooNE detector, Phys. Rev. D **102**, 112013 (2020), arXiv:2010.02390 [hep-ex].

[33] W. Van De Pontseele, *Search for Electron Neutrino Anomalies with the MicroBooNE Detector*, Ph.D. thesis, Oxford U. (2020).

[34] S. Gardiner, Mathematical methods for neutrino cross-section extraction, arXiv:2401.04065 [hep-ex] (2024).

[35] T. Golan, J. T. Sobczyk, and J. Zmuda, NuWro: the Wroclaw Monte Carlo Generator of Neutrino Interactions, Nucl. Phys. B Proc. Suppl. **229-232**, 499 (2012).

[36] P. Abratenko *et al.* (MicroBooNE Collaboration), Multidifferential cross section measurements of ν_μ-argon quasielasticlike reactions with the MicroBooNE detector, Phys. Rev. D **108**, 053002 (2023), arXiv:2301.03700 [hep-ex].

[37] P. Abratenko *et al.* (MicroBooNE Collaboration), First Double-Differential Measurement of Kinematic Imbalance in Neutrino Interactions with the MicroBooNE Detector, Phys. Rev. Lett. **131**, 101802 (2023), arXiv:2301.03706 [hep-ex].

[38] J. Calcutt, C. Thorpe, K. Mahn, and L. Fields, Geant4Reweight: a framework for evaluating and propagating hadronic interaction uncertainties in Geant4, J. Instrum. **16**, P08042 (2021), arXiv:2105.01744 [physics.data-an].

[39] R. Acciarri *et al.* (ArgoNeuT Collaboration), A Study of Electron Recombination Using Highly Ionizing Particles in the ArgoNeuT Liquid Argon TPC, J. Instrum. **8**, P08005 (2013), arXiv:1306.1712 [physics.ins-det].

[40] P. Abratenko *et al.* (MicroBooNE Collaboration), Novel approach for evaluating detector-related uncertainties in a LArTPC using MicroBooNE data, Eur. Phys. J. C **82**, 454 (2022), arXiv:2111.03556 [hep-ex].

[41] P. Abratenko *et al.* (MicroBooNE Collaboration), Scintillation light calibrations, systematic uncertainties, and triggering efficiency in the MicroBooNE detector, arXiv:2603.23691 [physics.ins-det] (2026).

[42] W. Tang, X. Li, X. Qian, H. Wei, and C. Zhang, Data Unfolding with Wiener-SVD Method, J. Instrum. **12**, P10002 (2017), arXiv:1705.03568 [physics.data-an].

[43] G. D'Agostini, A Multidimensional unfolding method based on Bayes' theorem, Nucl. Instrum. Meth. A **362**, 487 (1995).

[44] A. V. Butkevich, Analysis of flux-integrated cross sections for quasi-elastic neutrino charged-current scattering off ^{12}C at MiniBooNE energies, Phys. Rev. C **82**, 055501 (2010), arXiv:1006.1595 [nucl-th].

[45] H. C. Chiang, E. Oset, and P. Fernandez de Cordoba, Muon capture revisited, Nucl. Phys. A **510**, 591 (1990).

[46] J. Nieves, J. E. Amaro, and M. Valverde, Inclusive quasi-elastic neutrino reactions, Phys. Rev. C **70**, 055503 (2004), [Erratum: Phys.Rev.C 72, 019902 (2005)], arXiv:nucl-th/0408005.

[47] J. Nieves, I. Ruiz Simo, and M. J. Vicente Vacas, Inclusive Charged–Current Neutrino–Nucleus Reactions, Phys. Rev. C **83**, 045501 (2011), arXiv:1102.2777 [hep-ph].

[48] K. S. Kuzmin, V. V. Lyubushkin, and V. A. Naumov, Lepton polarization in neutrino nucleon interactions, Mod. Phys. Lett. A **19**, 2815 (2004), arXiv:hep-ph/0312107.

[49] C. Berger and L. M. Sehgal, Lepton mass effects in single pion production by neutrinos, Phys. Rev. D **76**, 113004 (2007), arXiv:0709.4378 [hep-ph].

[50] C. Berger and L. M. Sehgal, PCAC and coherent pion production by low energy neutrinos, Phys. Rev. D **79**, 053003 (2009), arXiv:0812.2653 [hep-ph].

[51] A. Bodek and U. K. Yang, Modeling deep inelastic cross-sections in the few GeV region, Nucl. Phys. B Proc. Suppl. **112**, 70 (2002), arXiv:hep-ex/0203009.

[52] A. Bodek, I. Park, and U. K. Yang, Improved low Q^2 model for neutrino and electron nucleon cross sections in few GeV region, Nucl. Phys. B Proc. Suppl. **139**, 113 (2005), arXiv:hep-ph/0411202.

[53] T. Sjostrand, S. Mrenna, and P. Z. Skands, PYTHIA 6.4 Physics and Manual, J. High Energy Phys. **05**, 026 (2006), arXiv:hep-ph/0603175.

[54] S. Dytman, Y. Hayato, R. Raboanary, J. T. Sobczyk, J. Tena Vidal, and N. Vololoniaina, Comparison of validation methods of simulations for final state interactions in hadron production experiments, Phys. Rev. D **104**, 053006 (2021), arXiv:2103.07535 [hep-ph].

[55] P. Stowell *et al.*, NUISANCE: a neutrino cross-section generator tuning and comparison framework, J. Instrum. **12**, P01016 (2017), arXiv:1612.07393 [hep-ex].

[56] R. D. Banerjee, A. M. Ankowski, K. M. Graczyk, B. E. Kowal, H. Prasad, and J. T. Sobczyk, JLab spectral functions of argon in NuWro and their implications for MicroBooNE, Phys. Rev. D **109**, 073004 (2024), arXiv:2312.13369 [hep-ph].

[57] C. H. Llewellyn Smith, Neutrino Reactions at Accelerator Energies, Phys. Rept. **3**, 261 (1972).

[58] J. E. Sobczyk, J. Nieves, and F. Sánchez, Exclusive-final-state hadron observables from neutrino-nucleus multinucleon knockout, Phys. Rev. C **102**, 024601 (2020), arXiv:2002.08302 [nucl-th].

[59] R. González-Jiménez, N. Jachowicz, K. Niewczas, J. Nys, V. Pandey, T. Van Cuyck, and N. Van Dessel, Electroweak single-pion production off the nucleon: from threshold to high invariant masses, Phys. Rev. D **95**, 113007 (2017), arXiv:1612.05511 [nucl-th].

[60] A. M. Ankowski, R. D. Banerjee, J. T. Sobczyk, J. L. Bonilla, K. M. Graczyk, B. E. Kowal, and H. Prasad, Spectral function approach in NuWro: modeling of multinucleon final states in quasielastic scattering, arXiv:2508.10101 [hep-ph] (2025).

[61] H. Prasad, J. T. Sobczyk, R. D. Banerjee, J. L. Bonilla, K. M. Graczyk, B. E. Kowal, and A. M. Ankowski, Fine-tuning final state interactions model in the NuWro Monte Carlo event generator, Phys. Rev. D **113**, 096023 (2026), arXiv:2512.23350 [hep-ph].

[62] L. L. Salcedo, E. Oset, M. J. Vicente-Vacas, and C. Garcia-Recio, Computer Simulation of Inclusive Pion Nuclear Reactions, Nucl. Phys. A **484**, 557 (1988).

[63] O. Buss, T. Gaitanos, K. Gallmeister, H. van Hees, M. Kaskulov, O. Lalakulich, A. B. Larionov, T. Leitner, J. Weil, and U. Mosel, Transport-theoretical Description of Nuclear Reactions, Phys. Rept. **512**, 1 (2012), arXiv:1106.1344 [hep-ph].

[64] T. Leitner, O. Buss, L. Alvarez-Ruso, and U. Mosel, Electron- and neutrino-nucleus scattering from the quasielastic to the resonance region, Phys. Rev. C **79**, 034601 (2009), arXiv:0812.0587 [nucl-th].

[65] P. E. Bosted, An Empirical fit to the nucleon electromagnetic form-factors, Phys. Rev. C **51**, 409 (1995).

[66] B. Bogart, K. Gallmeister, and U. Mosel, In-medium changes of nucleon cross sections tested in neutrino-induced reactions, Phys. Rev. C **110**, 044001 (2024), arXiv:2405.05921 [hep-ex].

[67] L. Alvarez-Ruso *et al.* (GENIE Collaboration), Recent highlights from GENIE v3, Eur. Phys. J. ST **230**, 4449 (2021), arXiv:2106.09381 [hep-ph].

[68] A. S. Meyer, M. Betancourt, R. Gran, and R. J. Hill, Deuterium target data for precision neutrino-nucleus cross sections, Phys. Rev. D **93**, 113015 (2016), arXiv:1603.03048 [hep-ph].

[69] A. Boudard, J. Cugnon, J.-C. David, S. Leray, and D. Mancusi, New potentialities of the Liège intranuclear cascade model for reactions induced by nucleons and light charged particles, Phys. Rev. C **87**, 014606 (2013), arXiv:1210.3498 [nucl-th].

[70] D. Mancusi, A. Boudard, J. Cugnon, J.-C. David, P. Kaitaniemi, and S. Leray, Extension of the Liège intranuclear-cascade model to reactions induced by light nuclei, Phys. Rev. C **90**, 054602 (2014), arXiv:1407.7755 [nucl-th].

[71] A. Heikkinen, N. Stepanov, and J. P. Wellisch, Bertini intranuclear cascade implementation in GEANT4, eConf **C0303241**, MOMT008 (2003), arXiv:nucl-th/0306008.

[72] P. Abratenko *et al.* (MicroBooNE Collaboration), Measurement of nuclear effects in neutrino-argon interactions using generalized kinematic imbalance variables with the MicroBooNE detector, Phys. Rev. D **109**, 092007 (2024), arXiv:2310.06082 [nucl-ex].

[73] P. Abratenko *et al.* (MicroBooNE Collaboration), First study of neutrino angle reconstruction using quasielasticlike interactions in MicroBooNE, Phys. Rev. D **111**, 113007 (2025), arXiv:2504.17758 [hep-ex].

[74] P. Abratenko *et al.* (MicroBooNE Collaboration), Measurement of charged-current muon neutrino-argon interactions without pions in the final state using the MicroBooNE detector, Phys. Rev. D **112**, 072007 (2025), arXiv:2507.00921 [hep-ex].

[75] F. Martínez López, L. Cooper-Troendle, S. Gardiner, P. Green, and T. Mohayai, Goodness-of-fit for multi-distribution neutrino cross-section measurements with shared events, in preparation.

First double-differential cross section measurements in proton multiplicity and kinematics for mesonless ν_μ charged-current interactions on argon using the MicroBooNE detector

Supplemental Materials

CONTENTS

I. EFFICIENCY AND MIGRATION MATRICES

The selection efficiency and migration matrix, introduced in Eq. (4) of the main text, quantify the detector effects on the observables used in this analysis. Figures 1 through 22 show the per-bin selection efficiency and migration matrix for each of the 11 blocks in the analysis.

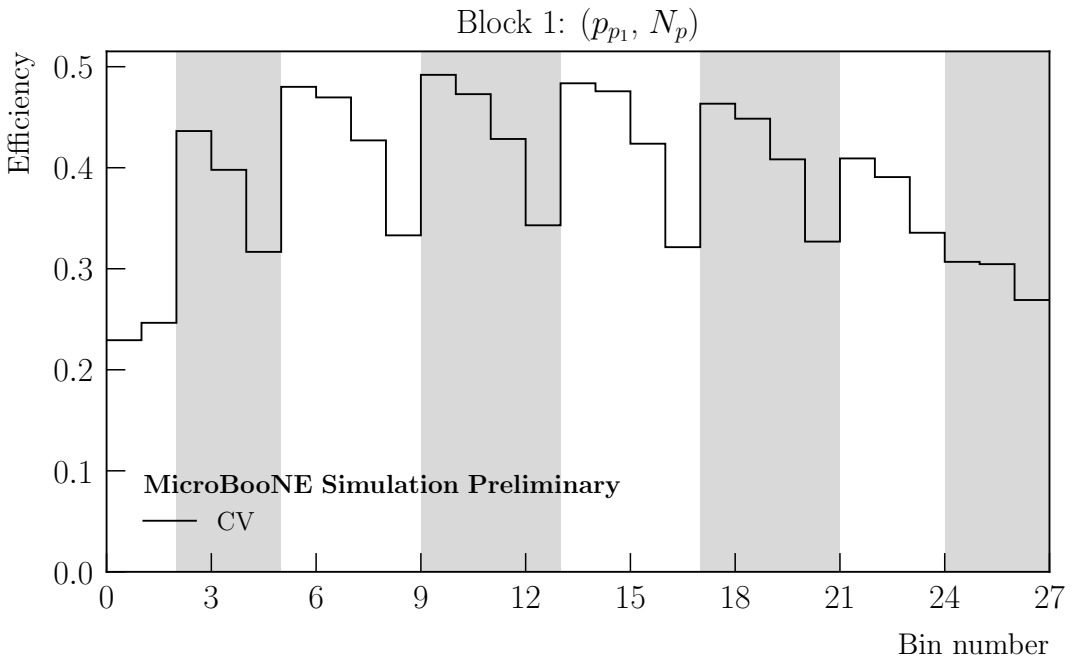

FIG. 1. Selection efficiency for the true bins in block 1, used for the double-differential (p_{p_1}, N_p) measurement.

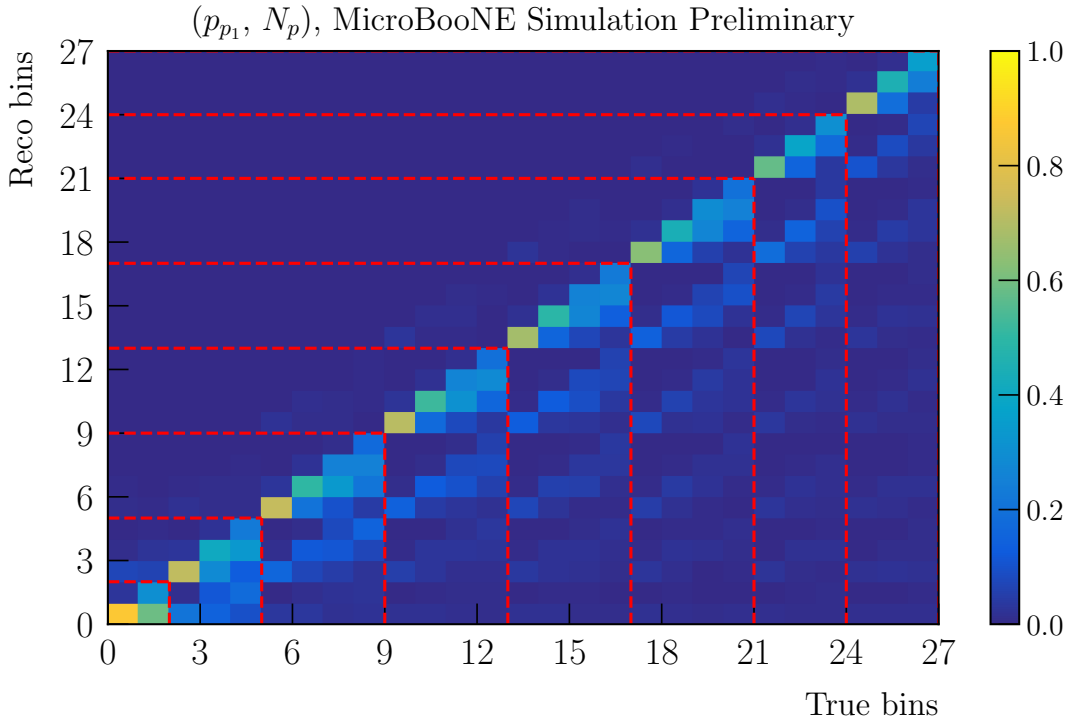

FIG. 2. Migration matrix for block 1, used for the double-differential (p_{p_1}, N_p) measurement. Dashed red lines indicate the slice boundaries.

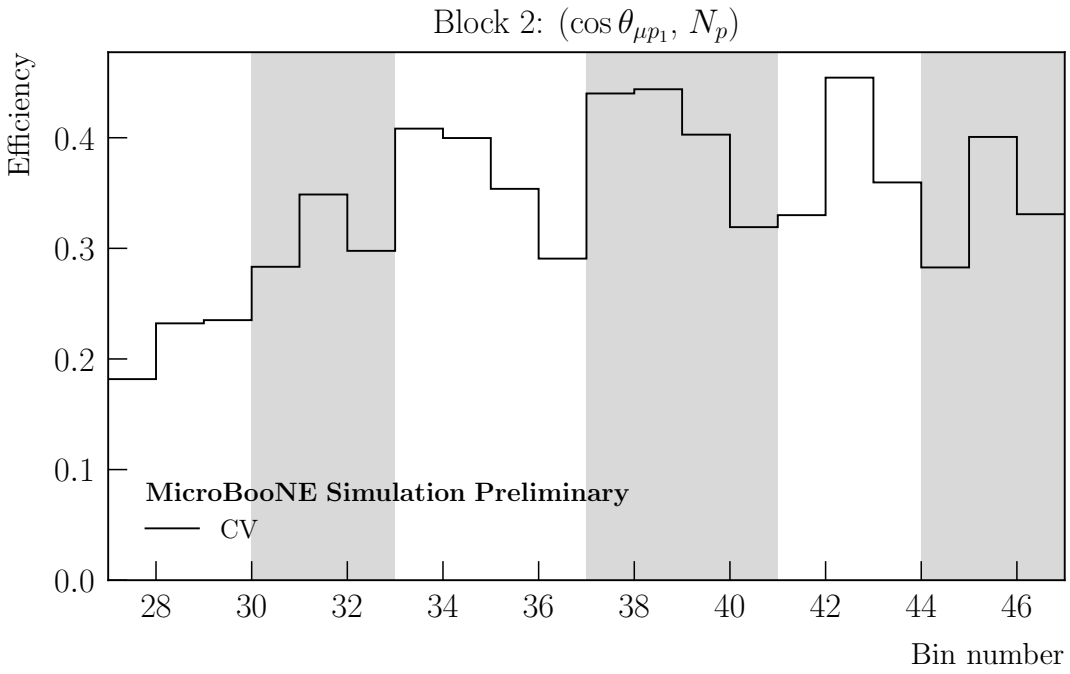

FIG. 3. Selection efficiency for the true bins in block 2, used for the double-differential $(\cos\theta_{\mu p_1}, N_p)$ measurement.

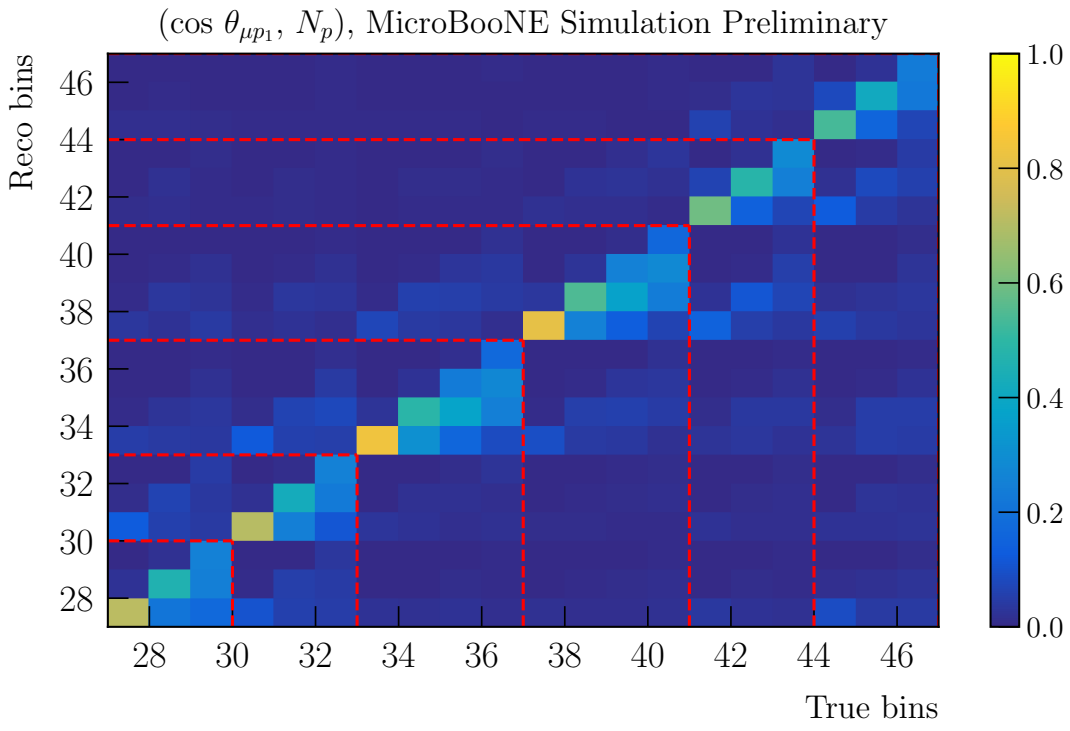

FIG. 4. Migration matrix for block 2, used for the double-differential $(\cos\theta_{\mu p_1}, N_p)$ measurement. Dashed red lines indicate the slice boundaries.

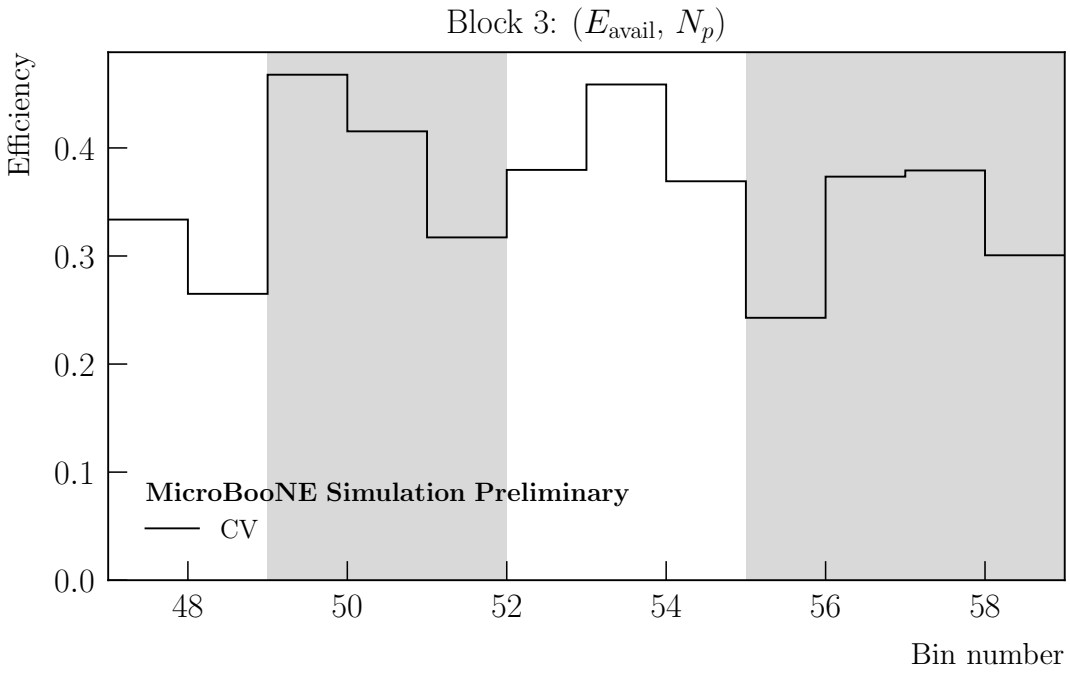

FIG. 5. Selection efficiency for the true bins in block 3, used for the double-differential (E_{avail}, N_p) measurement.

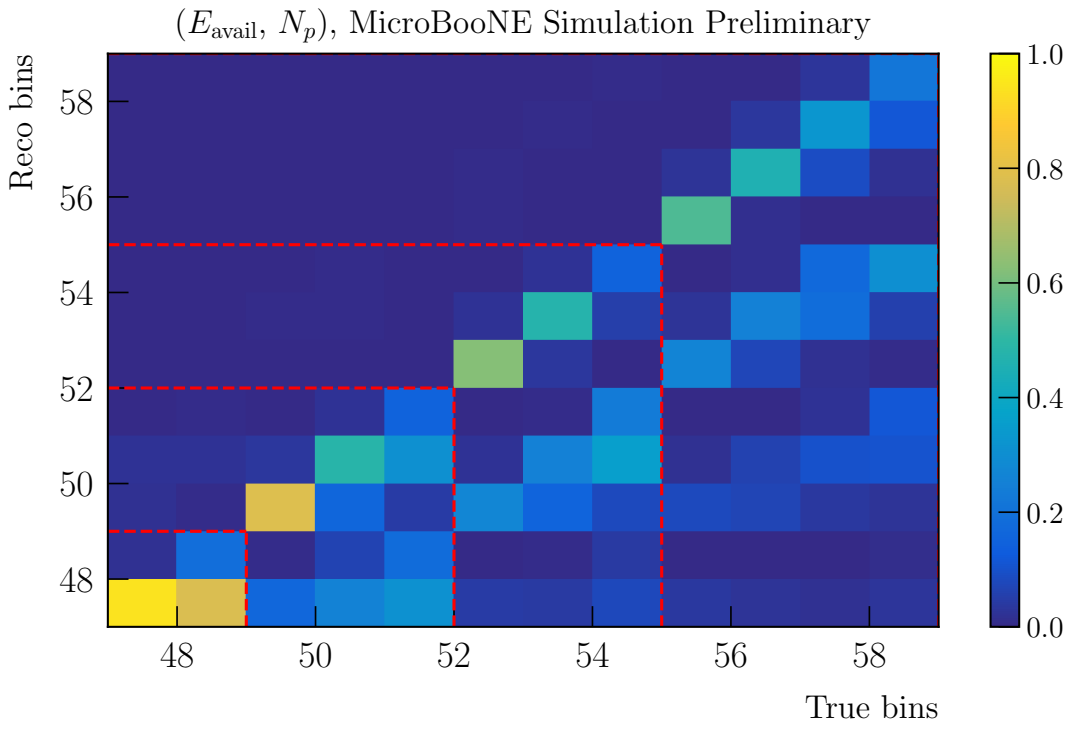

FIG. 6. Migration matrix for block 4, used for the double-differential (E_{avail}, N_p) measurement. Dashed red lines indicate the slice boundaries.

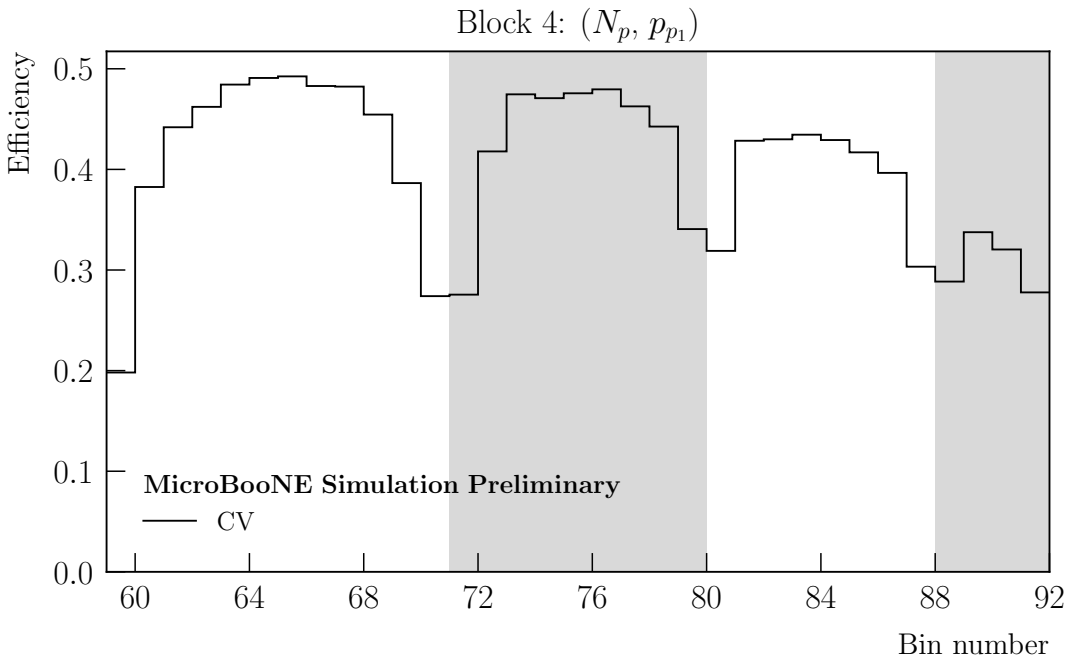

FIG. 7. Selection efficiency for the true bins in block 4, used for the double-differential (N_p, p_{p_1}) measurement.

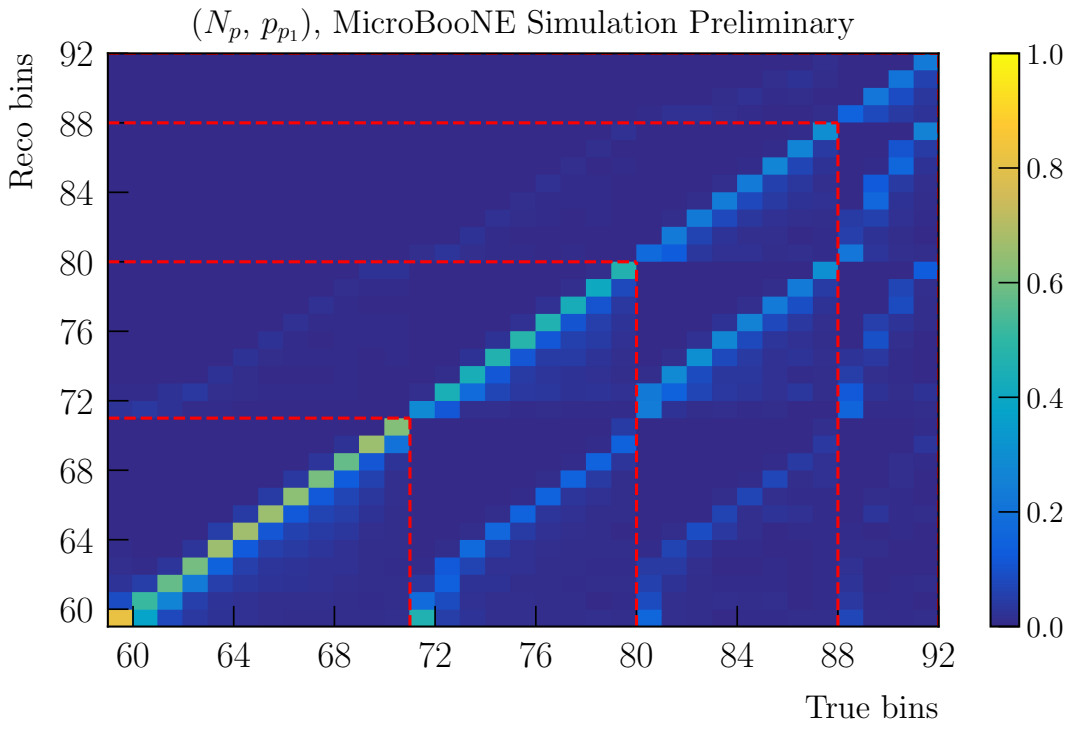

FIG. 8. Migration matrix for block 4, used for the double-differential (N_p, p_{p_1}) measurement. Dashed red lines indicate the slice boundaries.

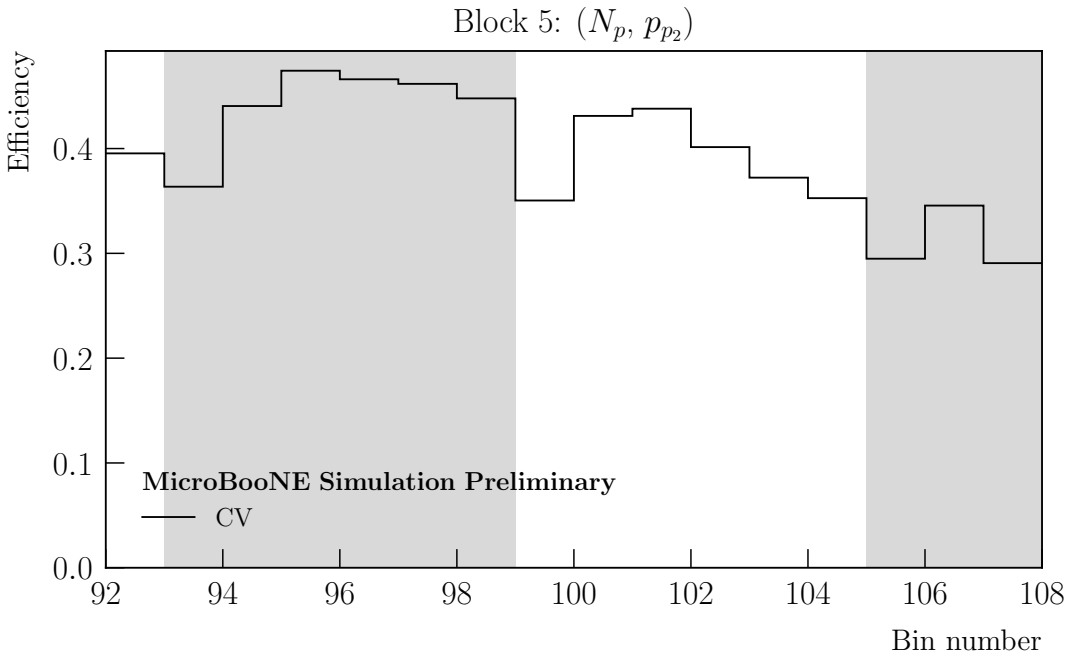

FIG. 9. Selection efficiency for the true bins in block 5, used for the double-differential (N_p, p_{p_2}) measurement.

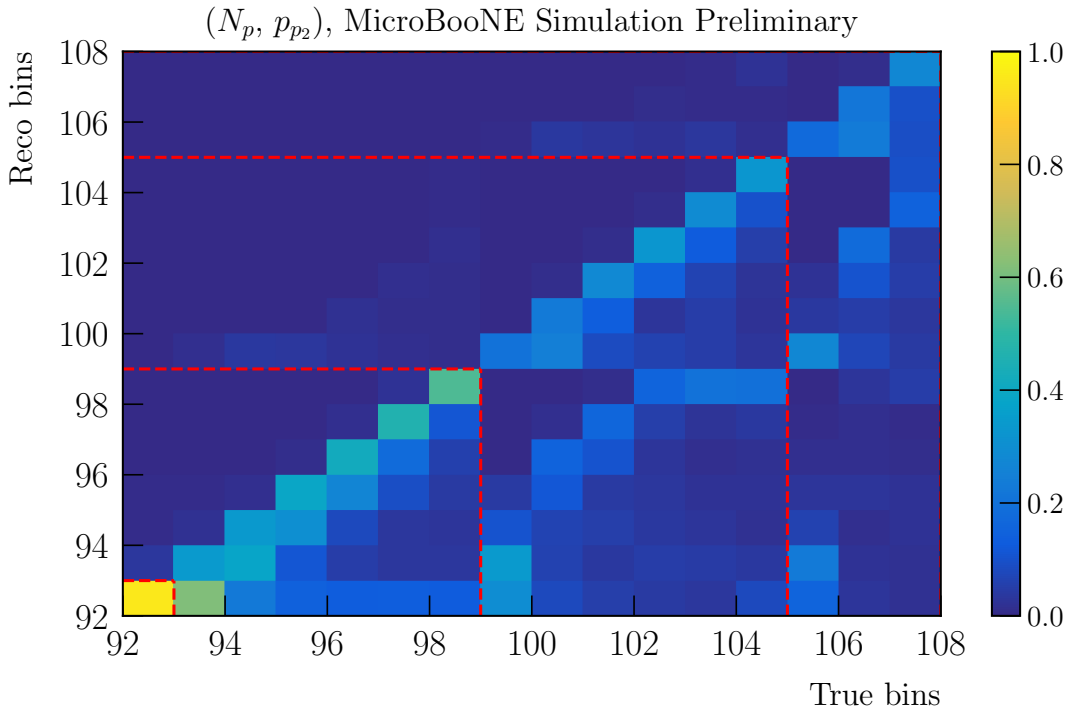

FIG. 10. Migration matrix for block 5, used for the double-differential (N_p, p_{p_2}) measurement. Dashed red lines indicate the slice boundaries.

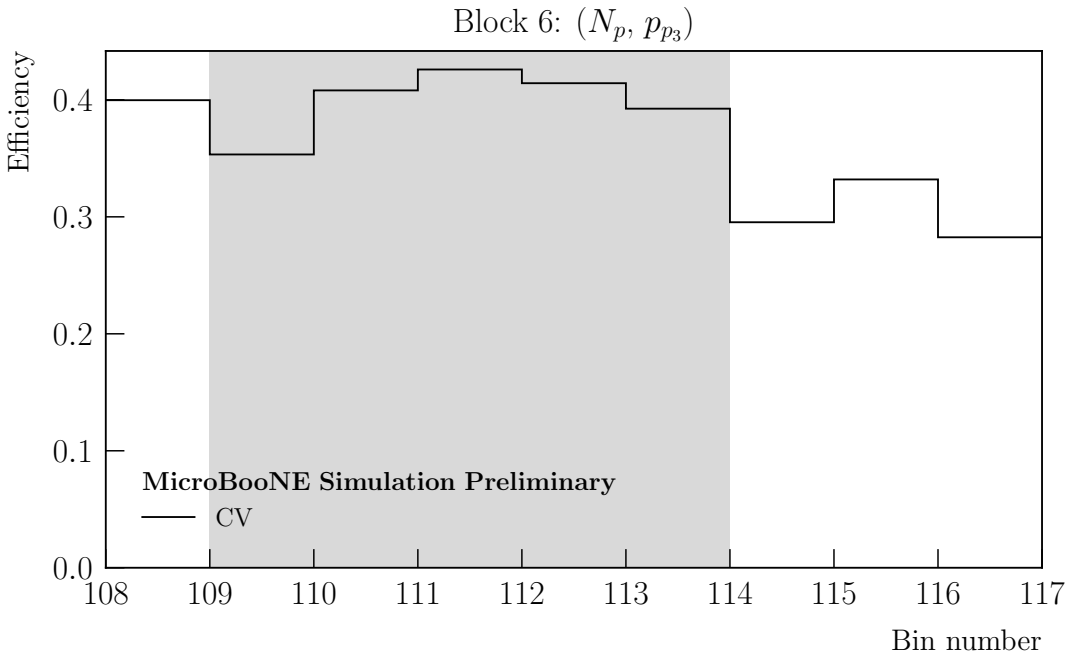

FIG. 11. Selection efficiency for the true bins in block 6, used for the double-differential (N_p, p_{p_3}) measurement.

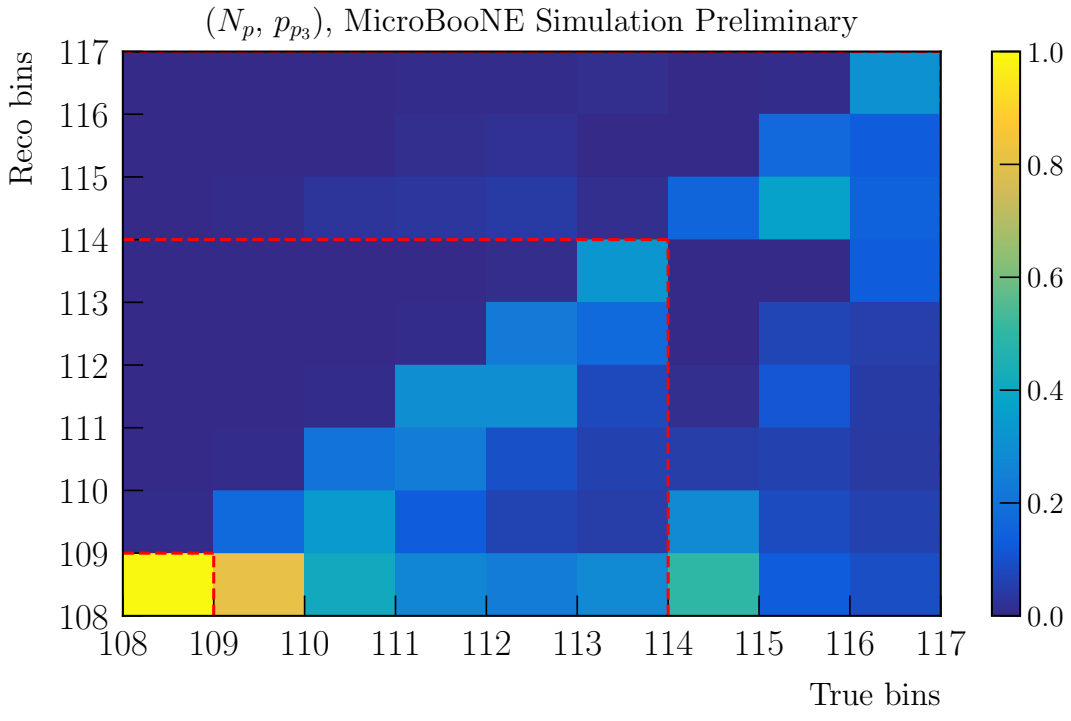

FIG. 12. Migration matrix for block 6, used for the double-differential (N_p, p_{p_3}) measurement. Dashed red lines indicate the slice boundaries.

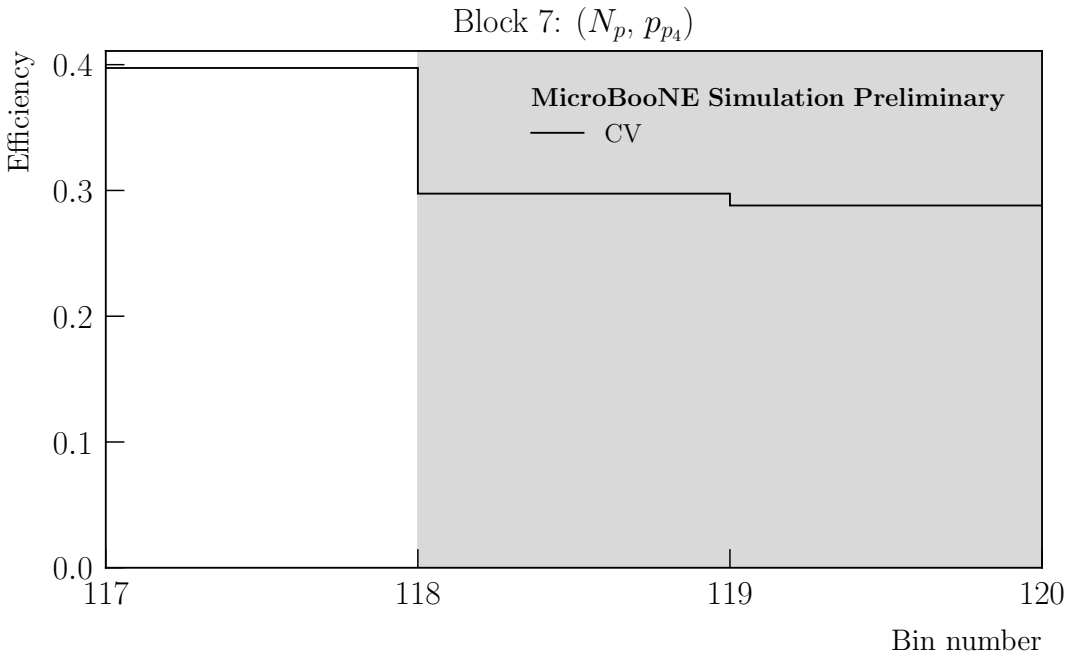

FIG. 13. Selection efficiency for the true bins in block 7, used for the double-differential (N_p, p_{p_4}) measurement.

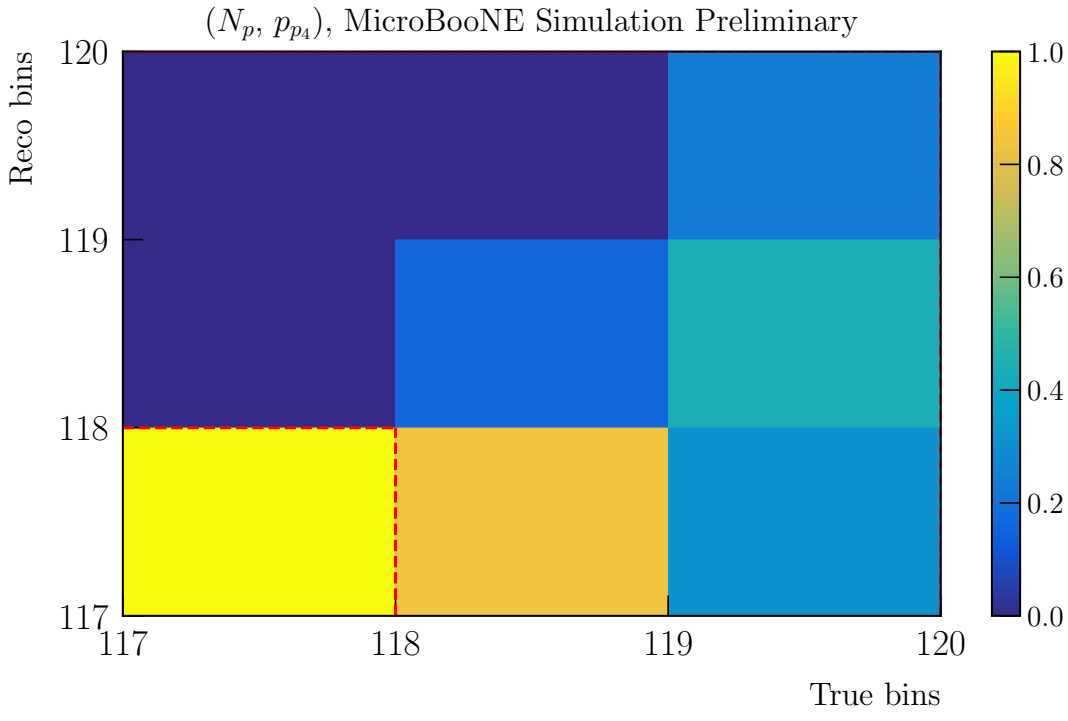

FIG. 14. Migration matrix for block 7, used for the double-differential (N_p, p_{p_4}) measurement. Dashed red lines indicate the slice boundaries.

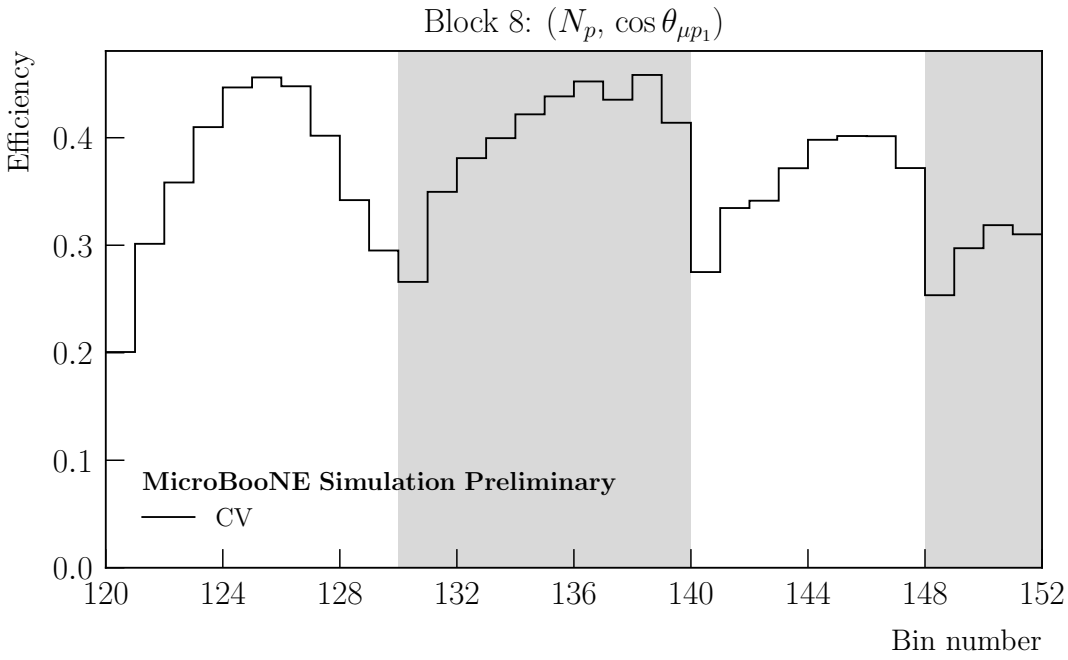

FIG. 15. Selection efficiency for the true bins in block 8, used for the double-differential (N_p, $\cos\theta_{\mu p_1}$) measurement.

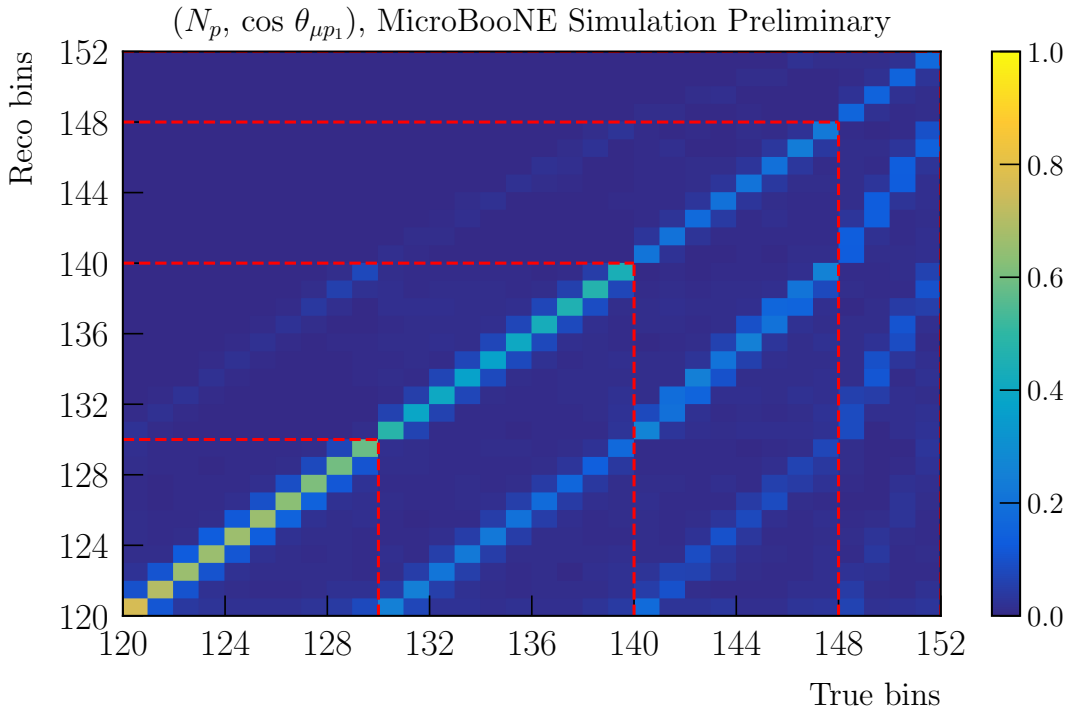

FIG. 16. Migration matrix for block 8, used for the double-differential (N_p, $\cos\theta_{\mu p_1}$) measurement. Dashed red lines indicate the slice boundaries.

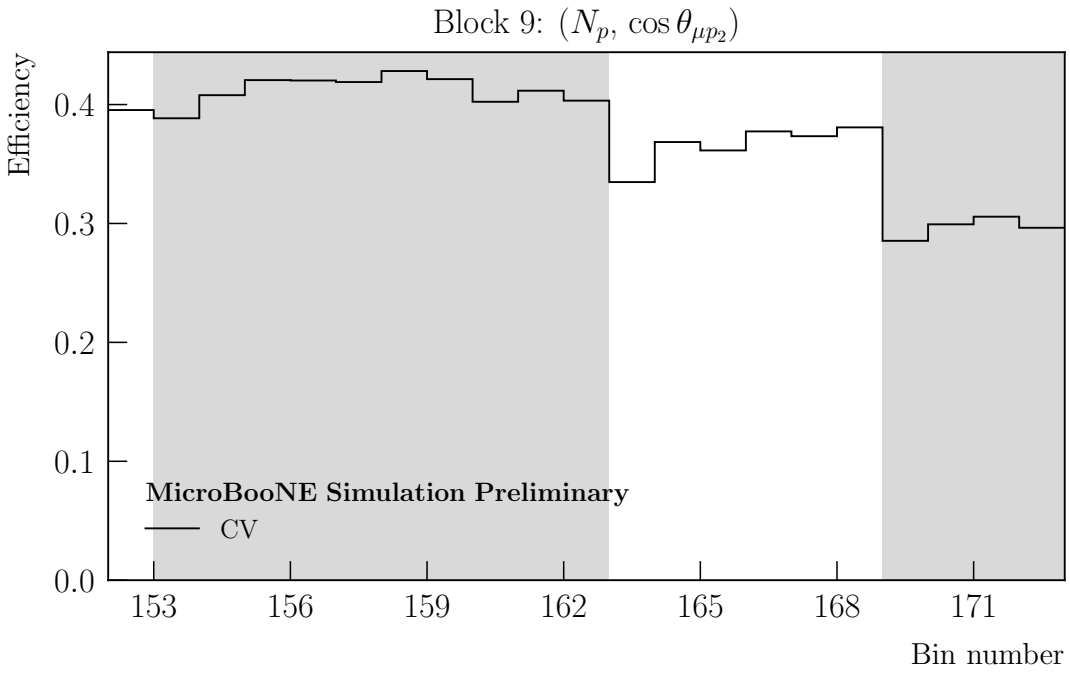

FIG. 17. Selection efficiency for the true bins in block 9, used for the double-differential (N_p, $\cos\theta_{\mu p_2}$) measurement.

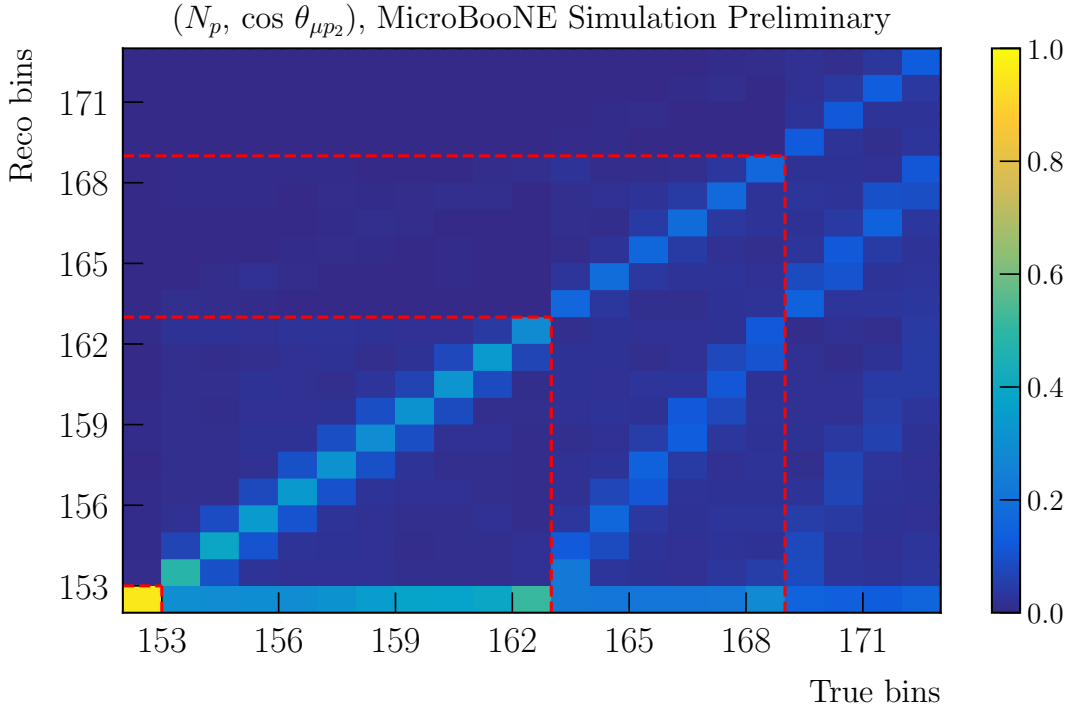

FIG. 18. Migration matrix for block 9, used for the double-differential (N_p, $\cos\theta_{\mu p_2}$) measurement. Dashed red lines indicate the slice boundaries.

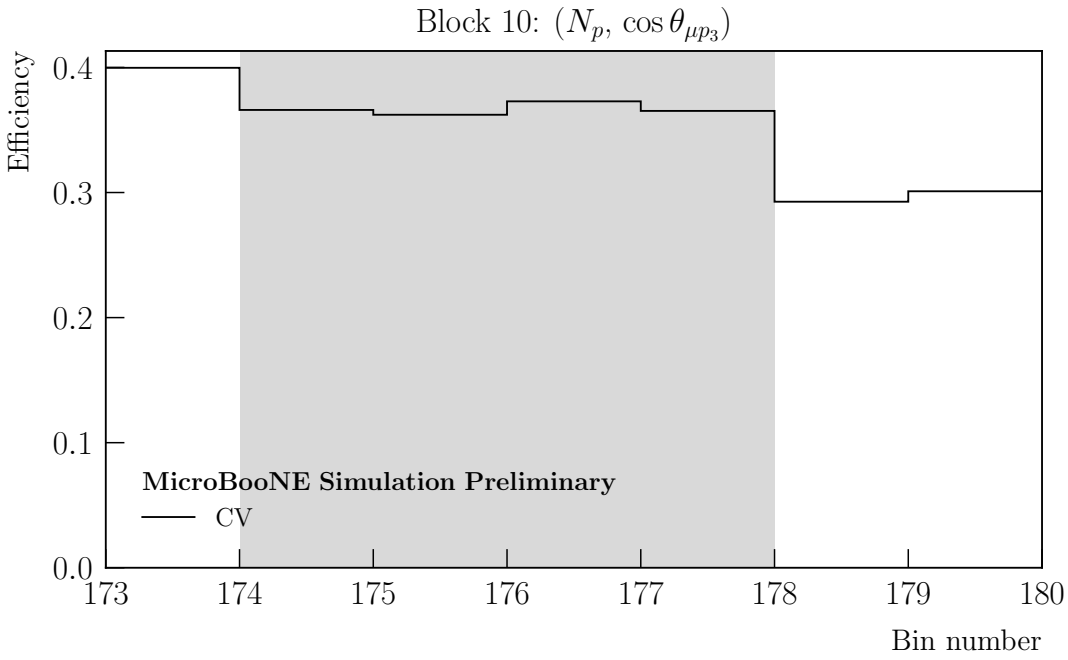

FIG. 19. Selection efficiency for the true bins in block 10, used for the double-differential (N_p, $\cos\theta_{\mu p_3}$) measurement.

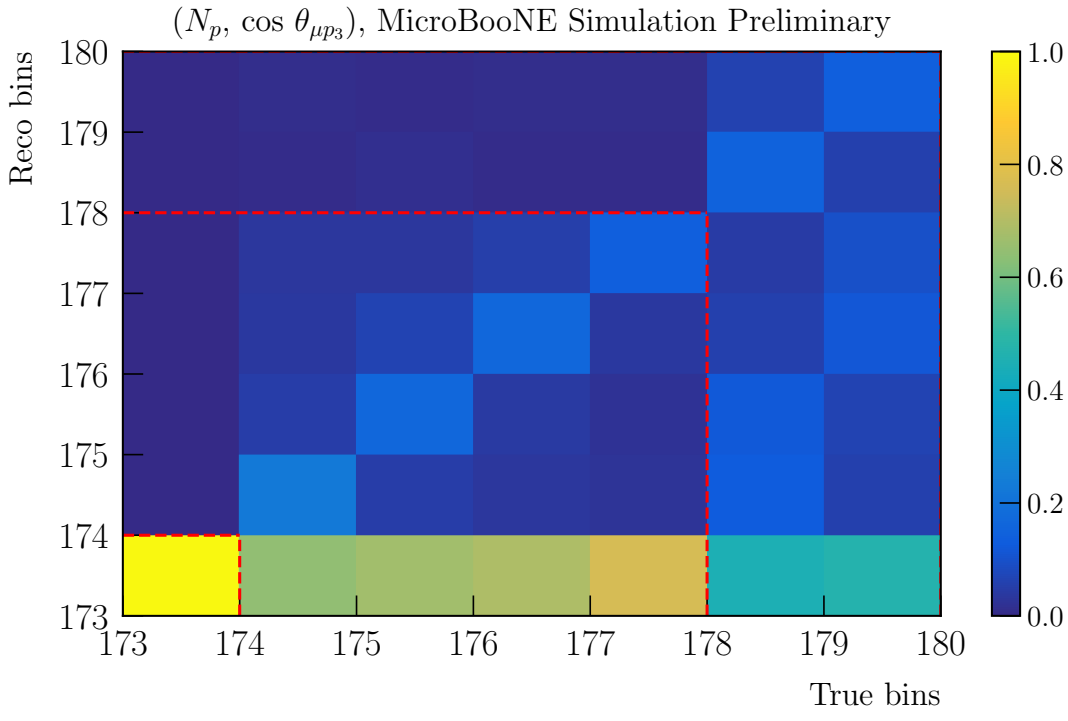

FIG. 20. Migration matrix for block 10, used for the double-differential (N_p, $\cos\theta_{\mu p_3}$) measurement. Dashed red lines indicate the slice boundaries.

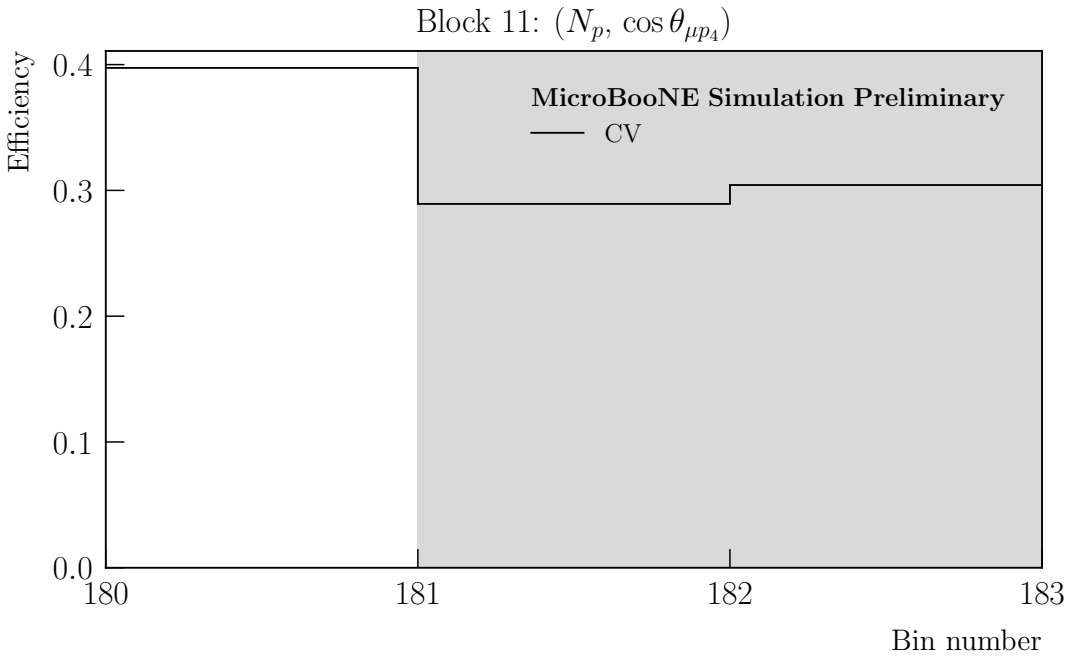

FIG. 21. Selection efficiency for the true bins in block 11, used for the double-differential (N_p, $\cos\theta_{\mu p_4}$) measurement.

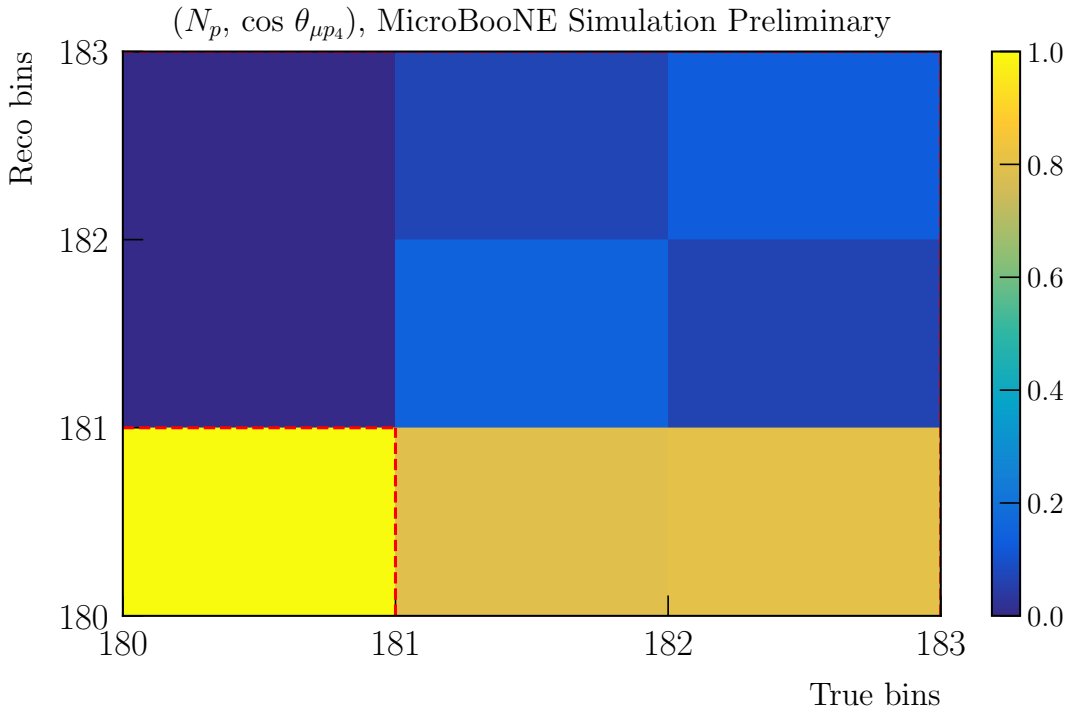

FIG. 22. Migration matrix for block 11, used for the double-differential (N_p, $\cos\theta_{\mu p_4}$) measurement. Dashed red lines indicate the slice boundaries.

II. VALIDATION STUDIES

A. NuWro fake data study

Figures 23 through 27 show the unfolded cross sections extracted from the NuWro fake data study described in Sec. III F of the main text.

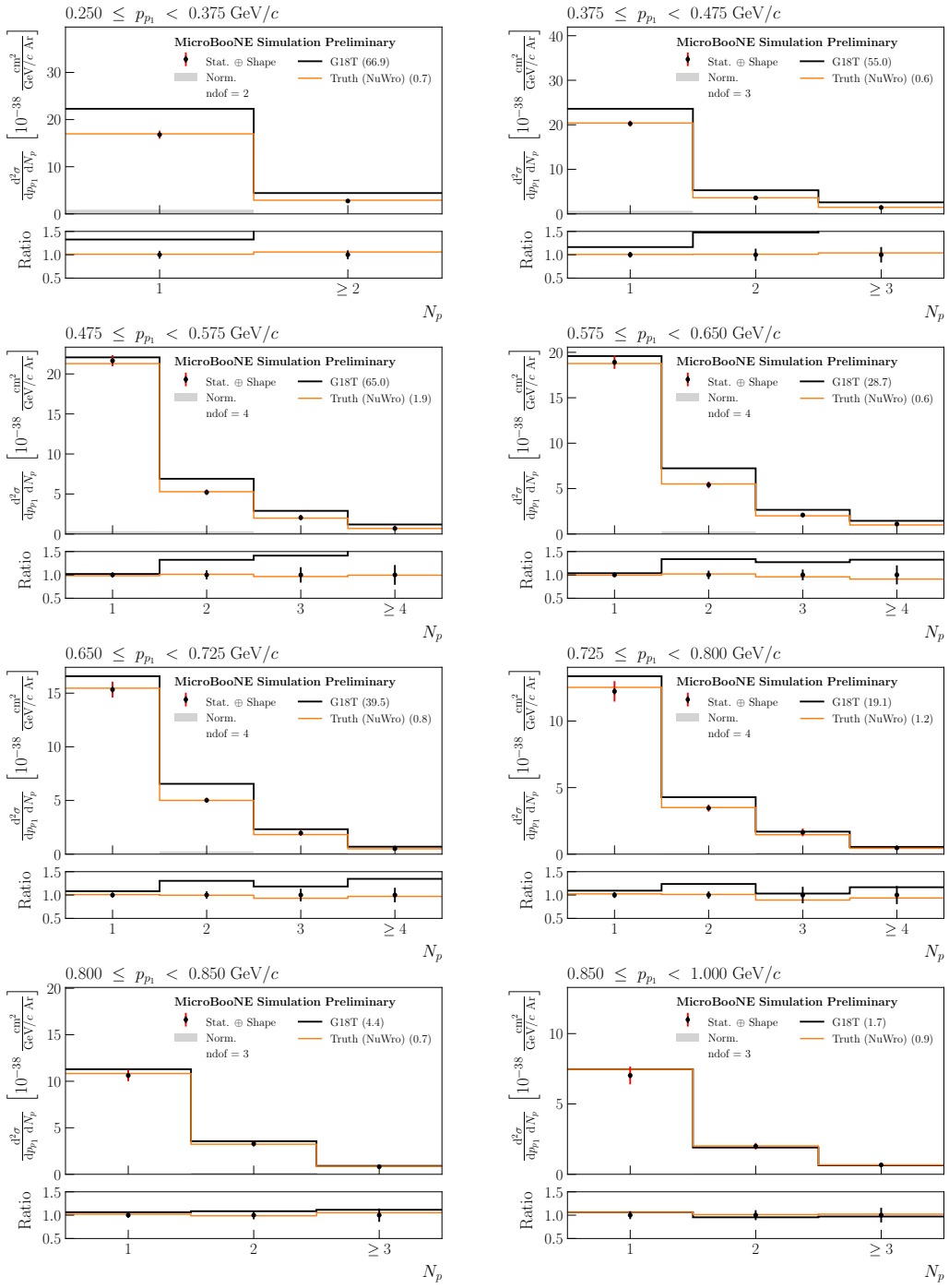

FIG. 23. Unfolded cross sections extracted from NuWro fake data for block 1, corresponding to the double-differential measurement (p_{p_1}, N_p) (black data points), with the corresponding MicroBooNE GENIE tune (black lines) and NuWro (orange lines) predictions.

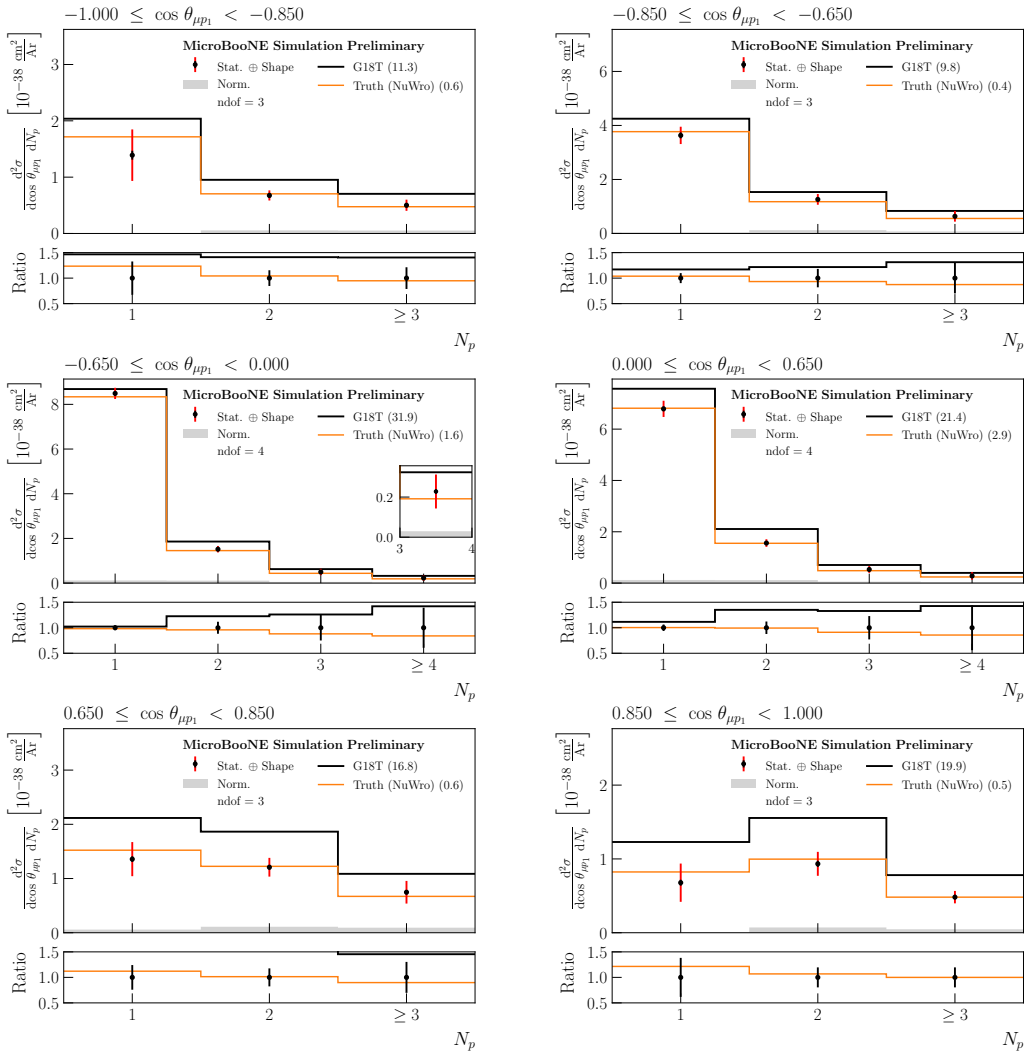

FIG. 24. Unfolded cross sections extracted from NuWro fake data for block 2, corresponding to the double-differential measurement ($\cos\theta_{\mu p_1}$, N_p) (black data points), with the corresponding MicroBooNE GENIE tune (black lines) and NuWro (orange lines) predictions.

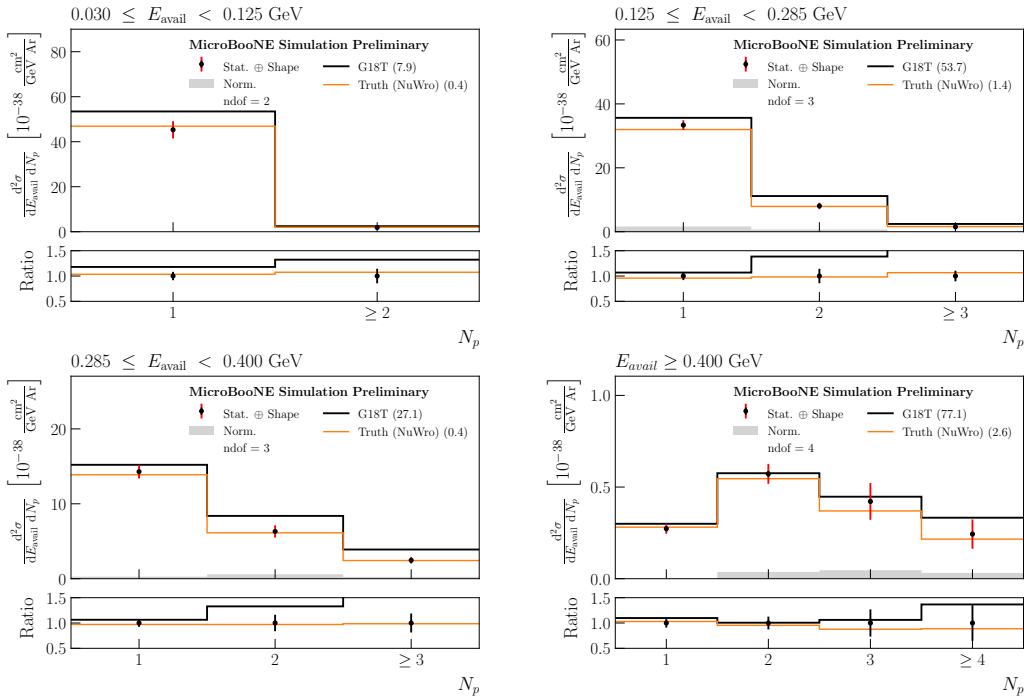

FIG. 25. Unfolded cross sections extracted from NuWro fake data for block 3, corresponding to the double-differential measurement (E_{avail}, N_p) (black data points), with the corresponding MicroBooNE GENIE tune (black lines) and NuWro (orange lines) predictions.

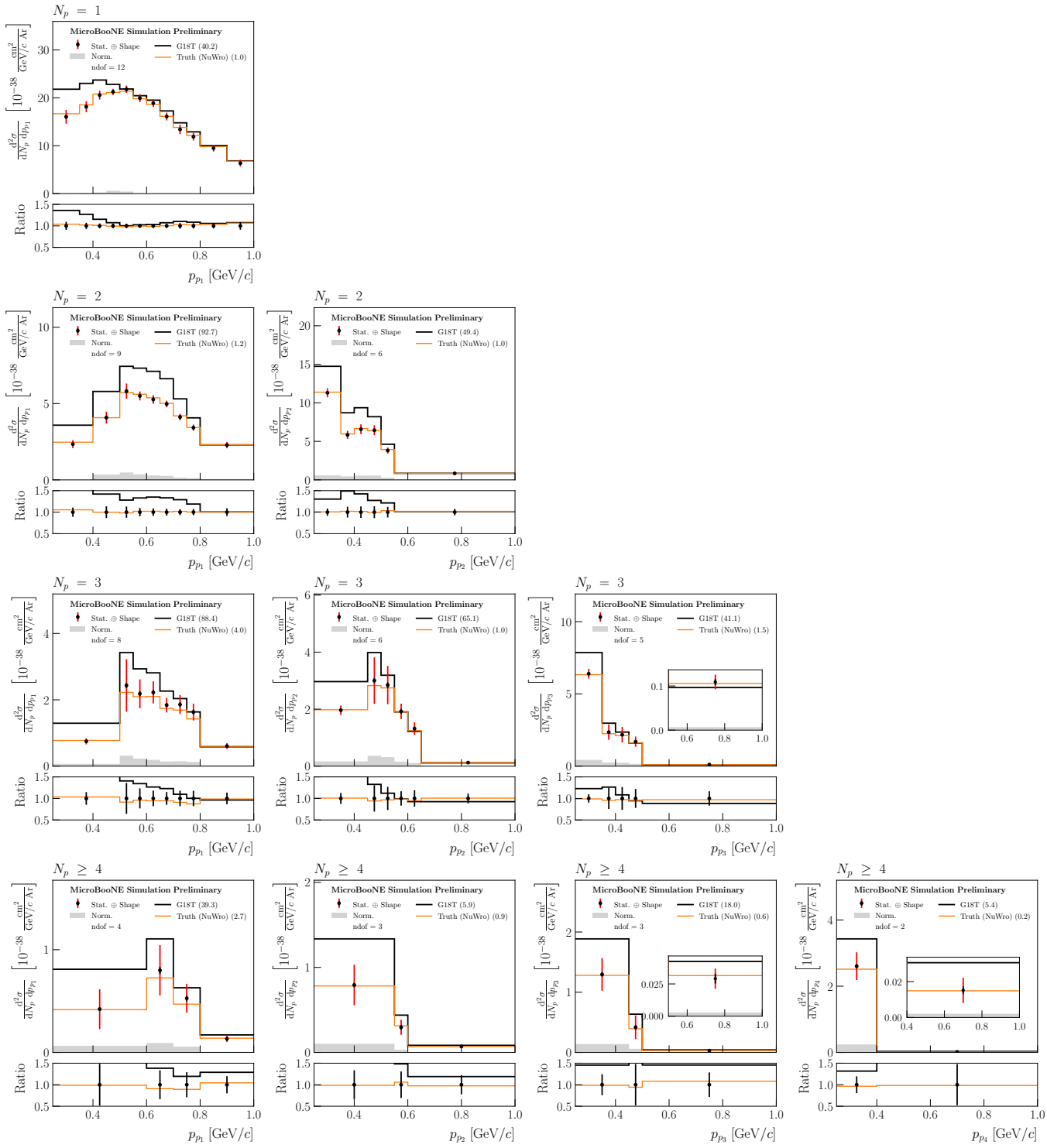

FIG. 26. Unfolded cross sections extracted from NuWro fake data for blocks 4, 5, 6, and 7, corresponding to the double-differential measurements (N_p, p_{p_i}) (black data points), with the corresponding MicroBooNE GENIE tune (black lines) and NuWro (orange lines) predictions.

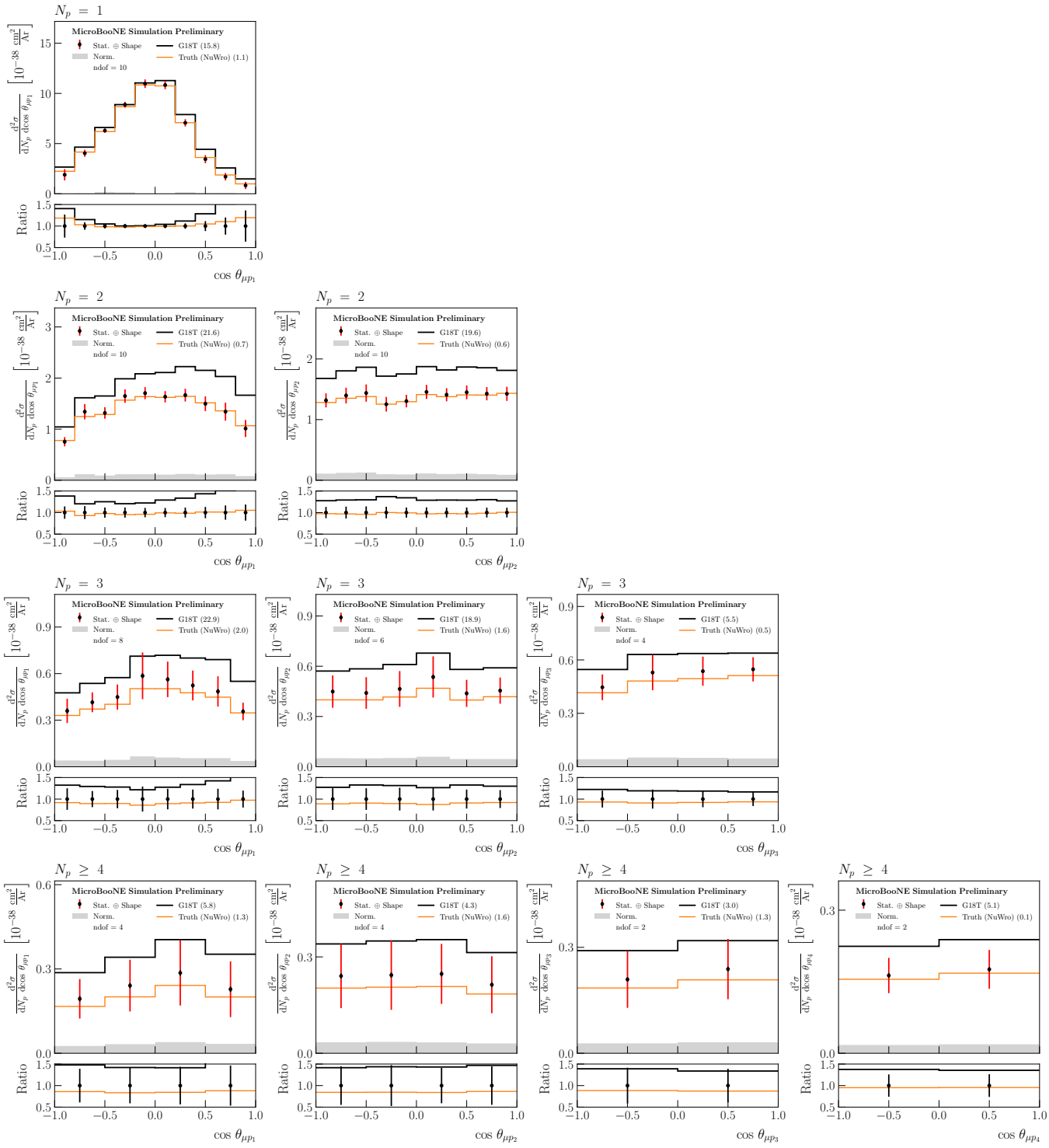

FIG. 27. Unfolded cross sections extracted from NuWro fake data for blocks 8, 9, 10, and 11, corresponding to the double-differential measurements (N_p, $\cos\theta_{\mu p_i}$) (black data points), with the corresponding MicroBooNE GENIE tune (black lines) and NuWro (orange lines) predictions.

B. Data-driven validation

Figures 28 through 32 show the unfolded event counts obtained using the re-simulated data and MC response matrices, as described in Sec. III F and Appendix D of the main text.

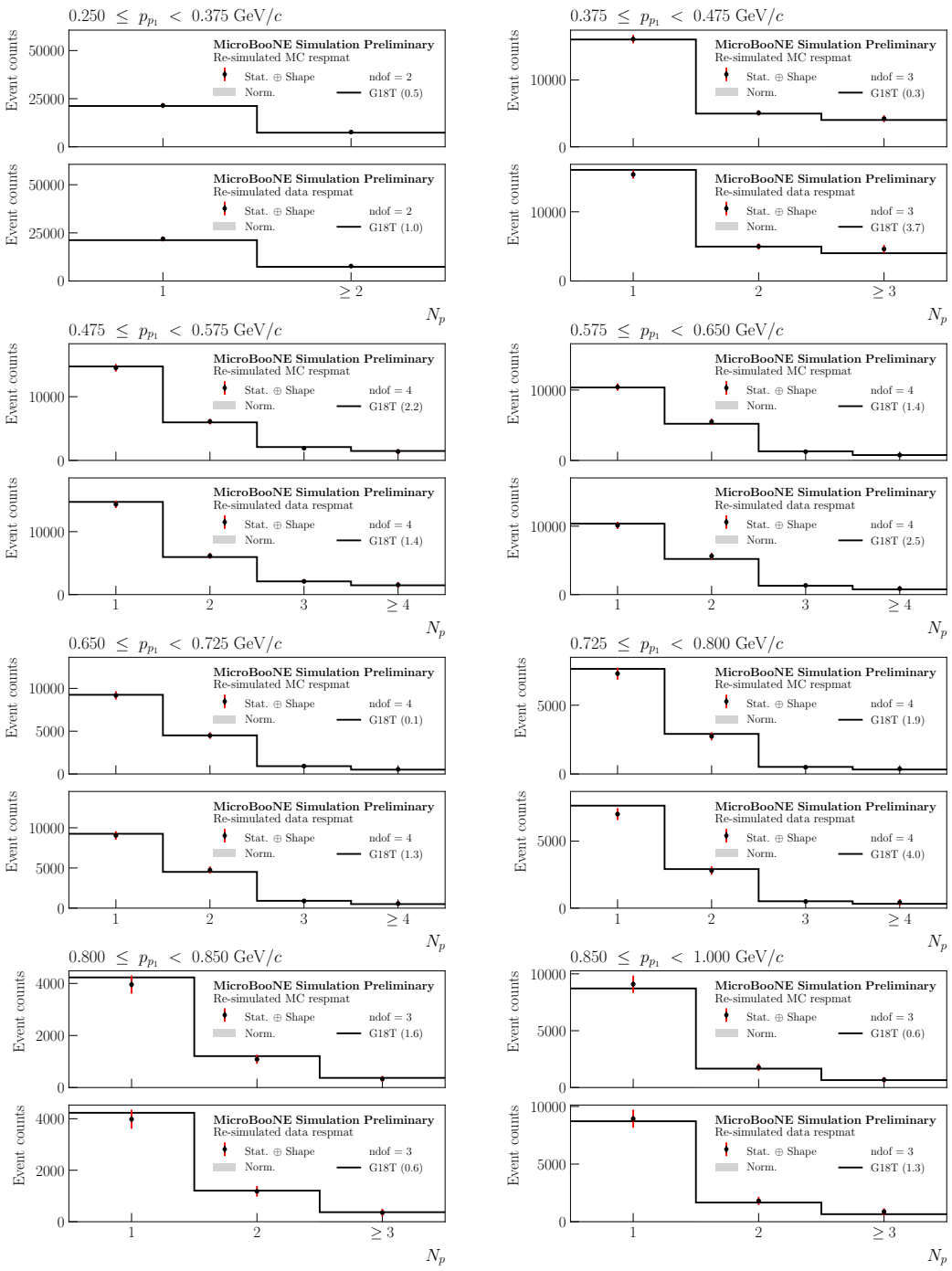

FIG. 28. Unfolded event counts extracted from GENIE fake data for block 1 (black data points), with the corresponding MicroBooNE GENIE tune predictions (black lines). The top and bottom subpanels use the re-simulated data and MC response matrices, respectively.

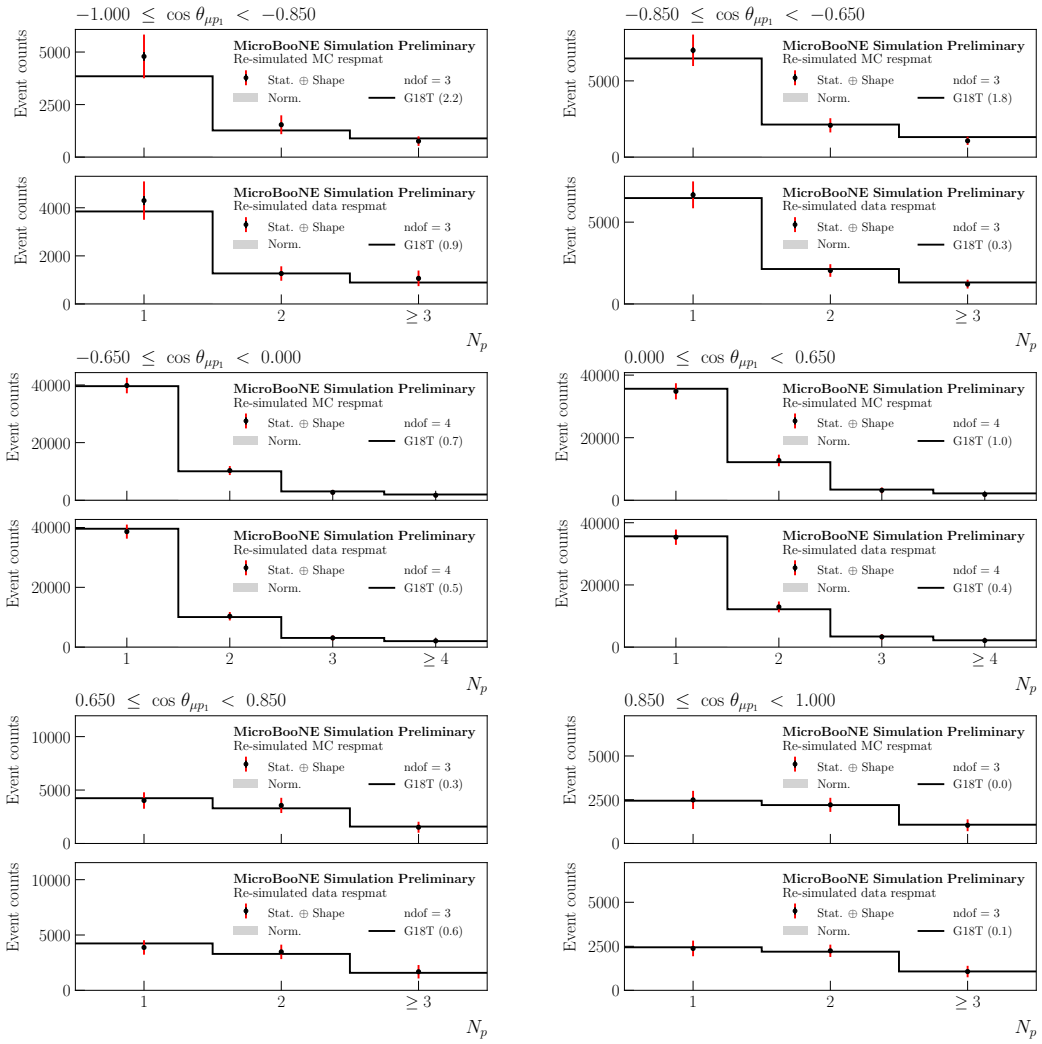

FIG. 29. Unfolded event counts extracted from GENIE fake data for block 2 (black data points), with the corresponding MicroBooNE GENIE tune predictions (black lines). The top and bottom subpanels use the re-simulated data and MC response matrices, respectively.

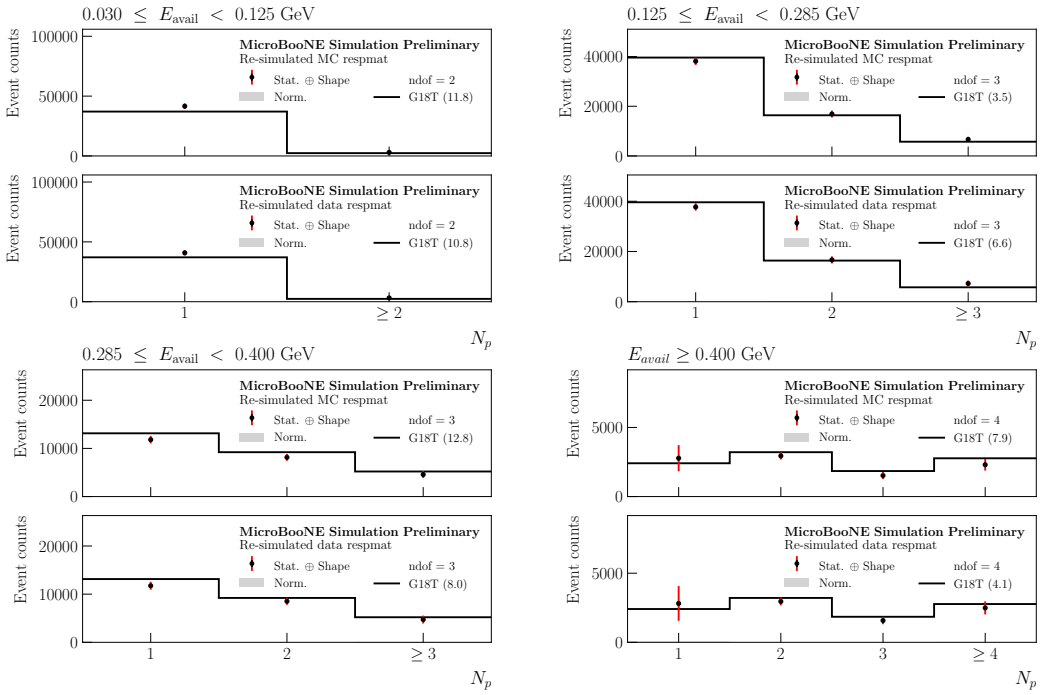

FIG. 30. Unfolded event counts extracted from GENIE fake data for block 3 (black data points), with the corresponding MicroBooNE GENIE tune predictions (black lines). The top and bottom subpanels use the re-simulated data and MC response matrices, respectively.

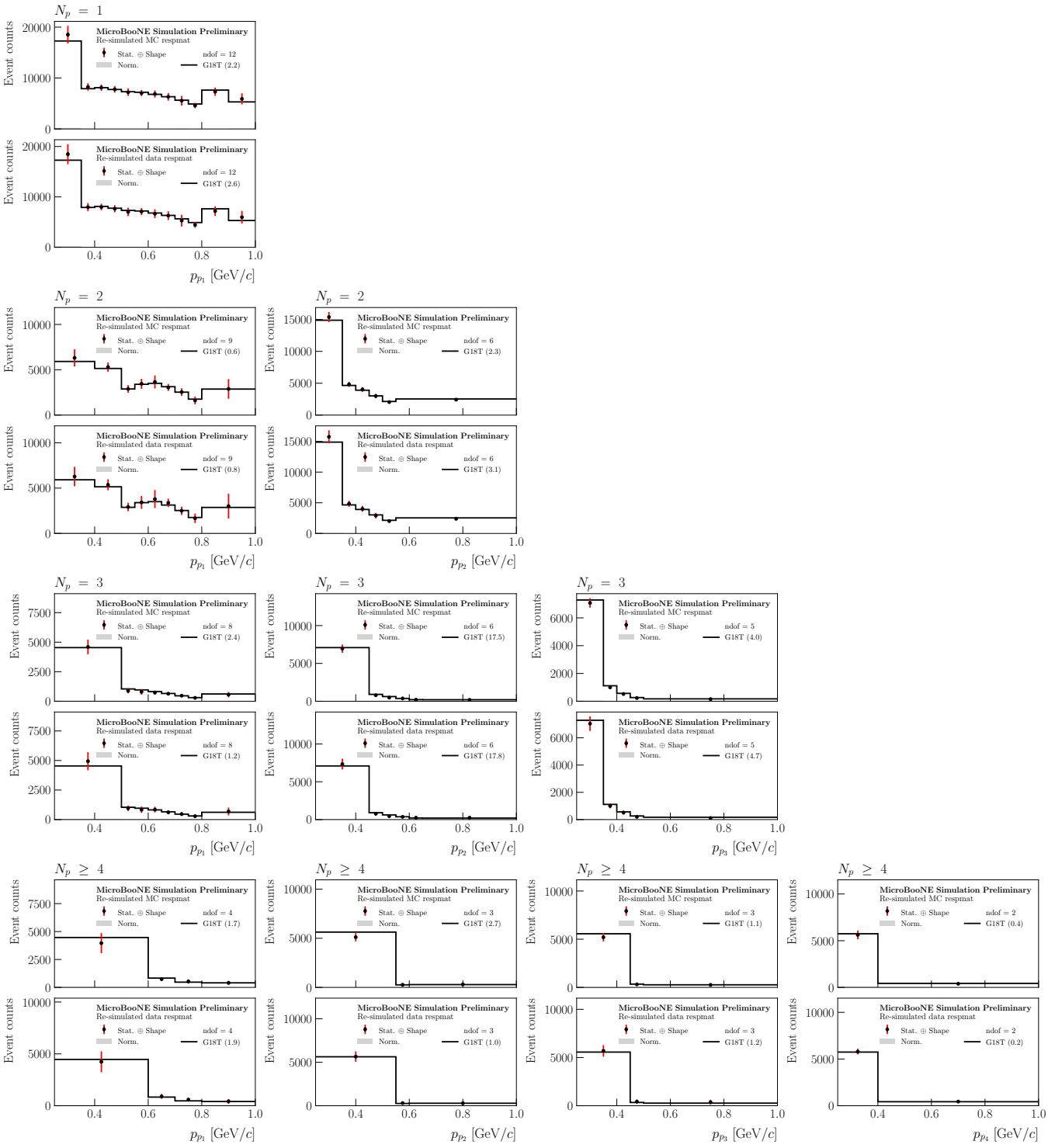

FIG. 31. Unfolded event counts extracted from GENIE fake data for blocks 4, 5, 6, and 7 (black data points), with the corresponding MicroBooNE GENIE tune predictions (black lines). The top and bottom subpanels use the re-simulated data and MC response matrices, respectively.

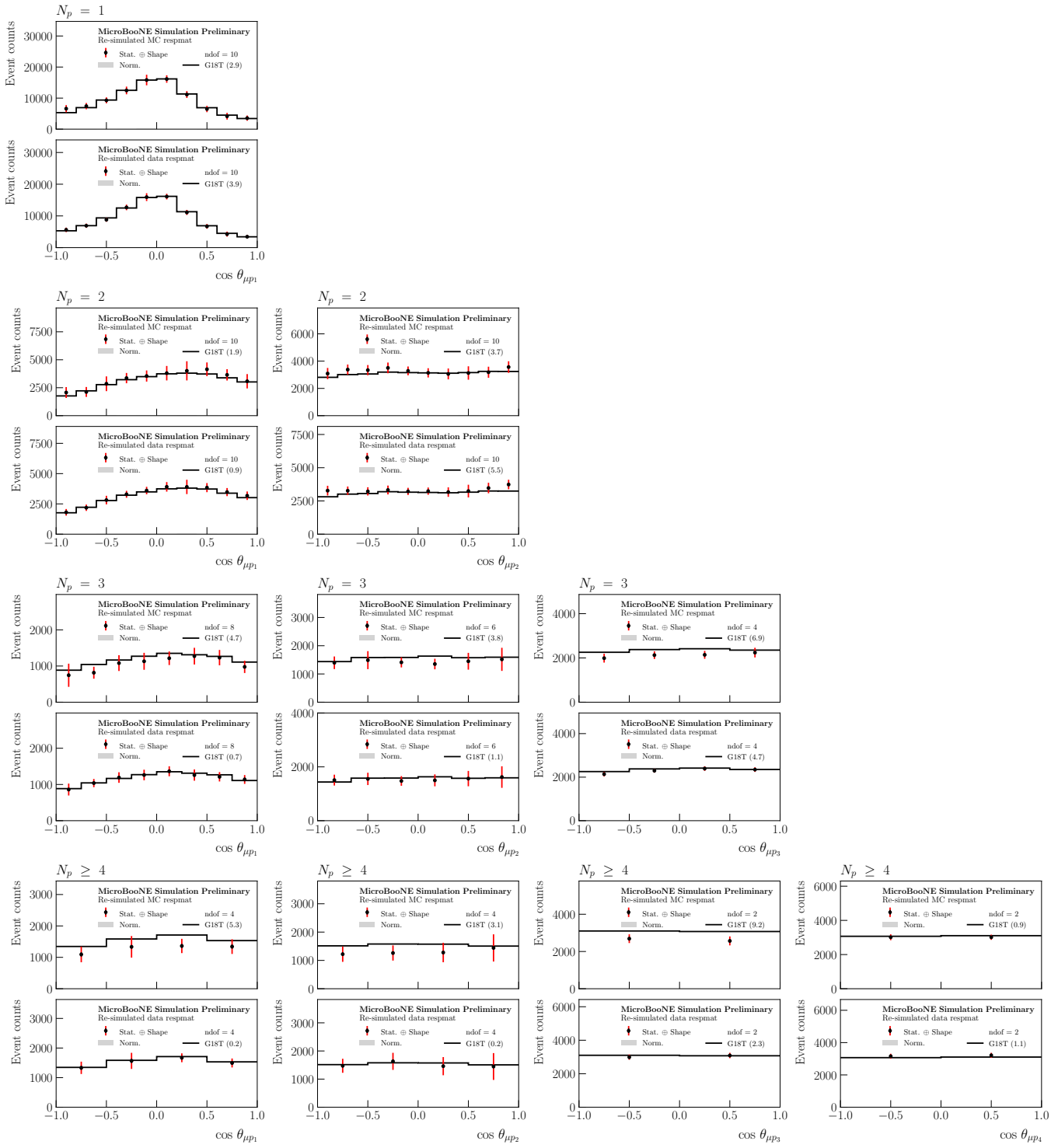

FIG. 32. Unfolded event counts extracted from GENIE fake data for blocks 8, 9, 10, and 11 (black data points), with the corresponding MicroBooNE GENIE tune predictions (black lines). The top and bottom subpanels use the re-simulated data and MC response matrices, respectively.

III. EVENT RATES BY INTERACTION MODE

Figures 33 through 37 show the reconstructed event rate distributions in the signal region decomposed by primary interaction mode (QE, MEC, and other) for each block.

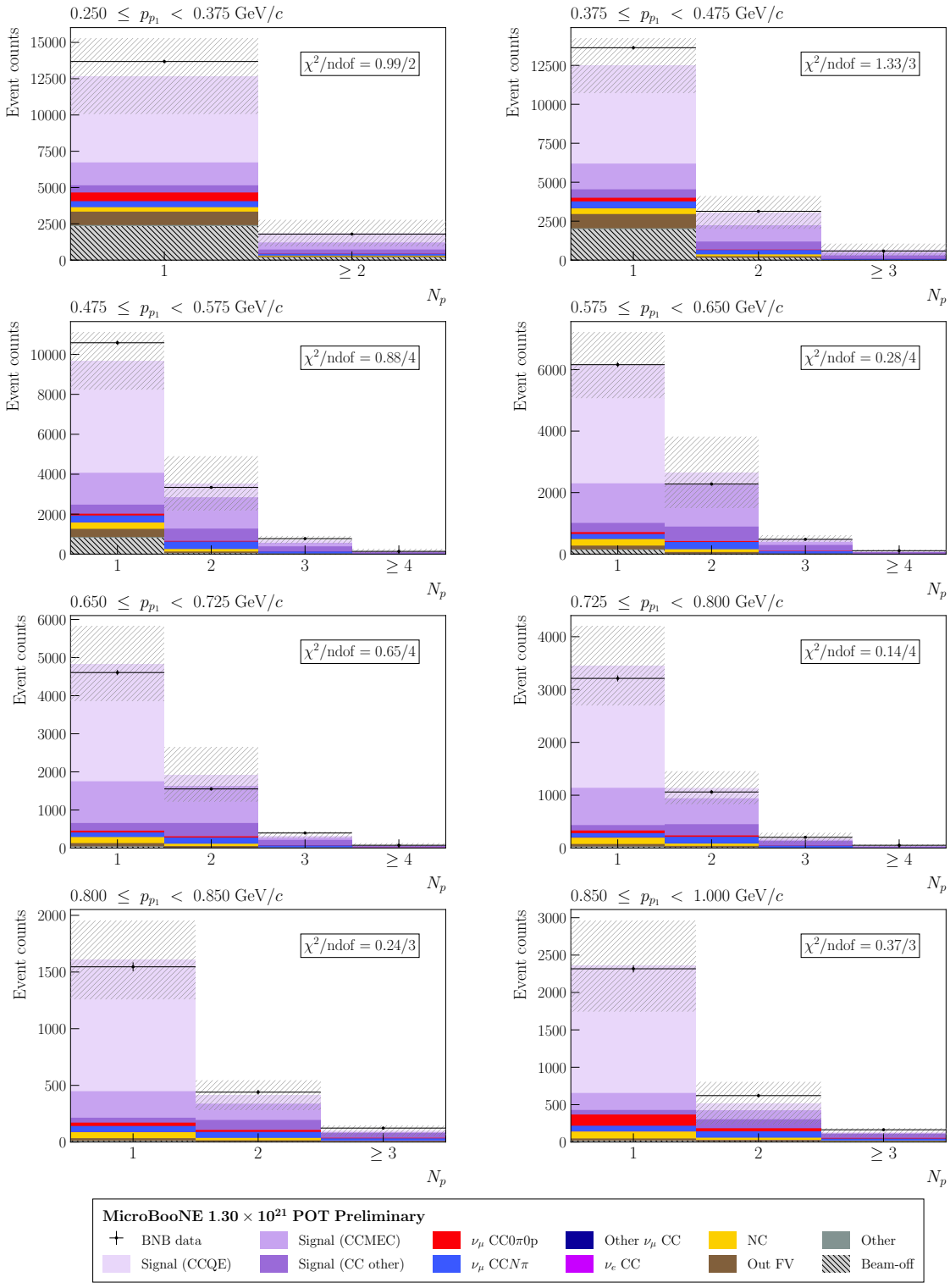

FIG. 33. Reconstructed event rate distributions for block 1, with the signal broken down by interaction mode, corresponding to the double-differential measurement (p_{p_1}, N_p). The total uncertainty on the prediction is indicated by the hatched boxes.

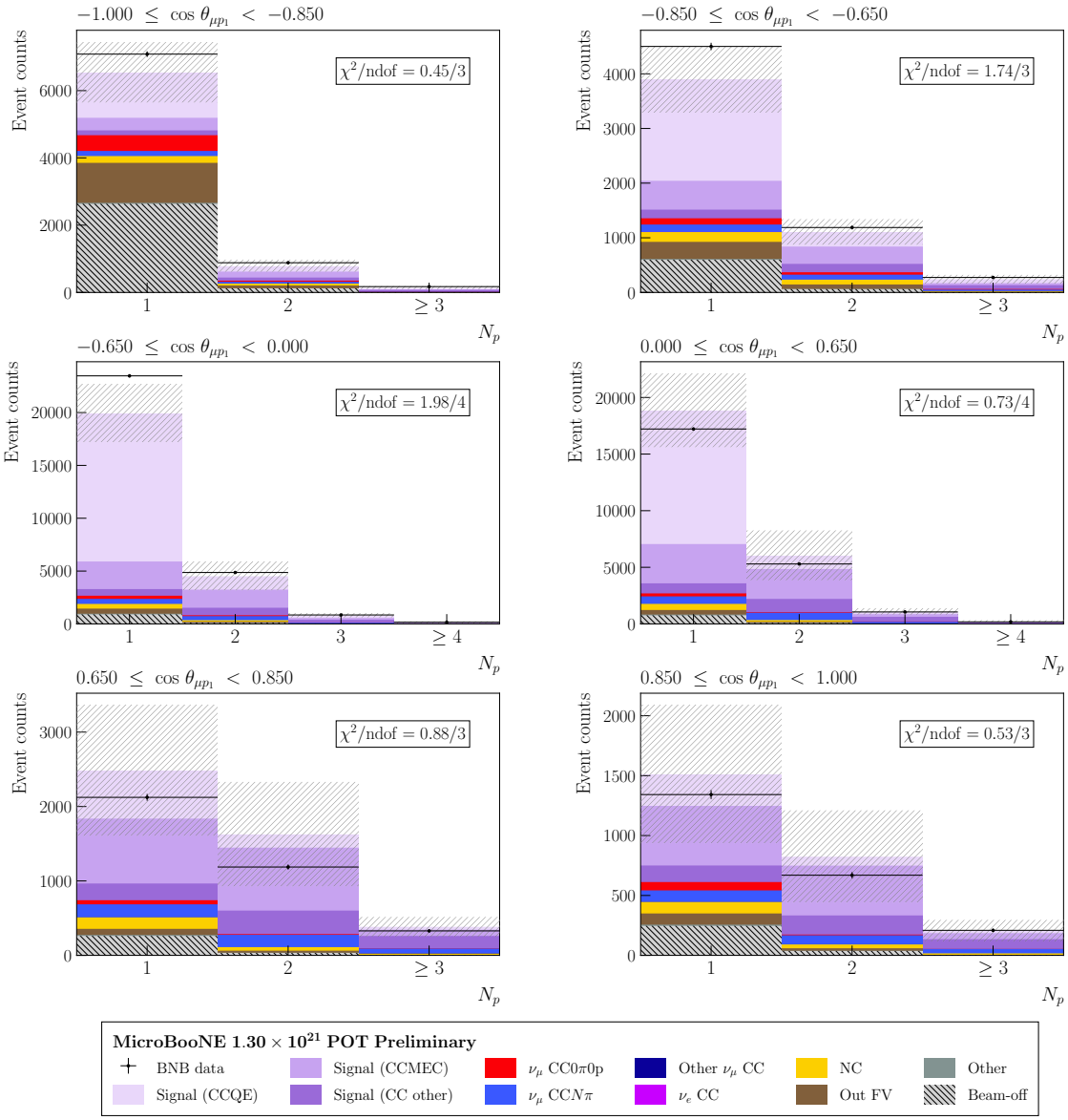

FIG. 34. Reconstructed event rate distributions for block 2, with the signal broken down by interaction mode, corresponding to the double-differential measurement $(\cos\theta_{\mu p_1}, N_p)$. The total uncertainty on the prediction is indicated by the hatched boxes.

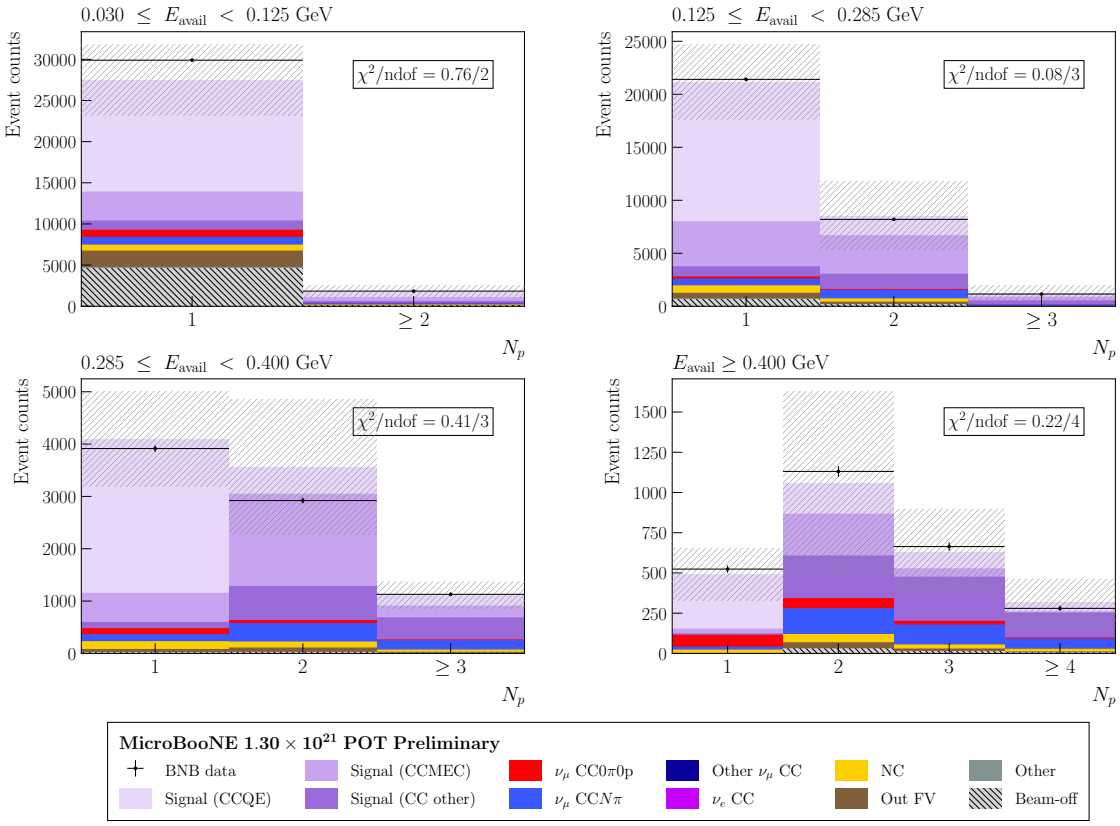

FIG. 35. Reconstructed event rate distributions for block 3, with the signal broken down by interaction mode, corresponding to the double-differential measurement (E_{avail}, N_p). The total uncertainty on the prediction is indicated by the hatched boxes.

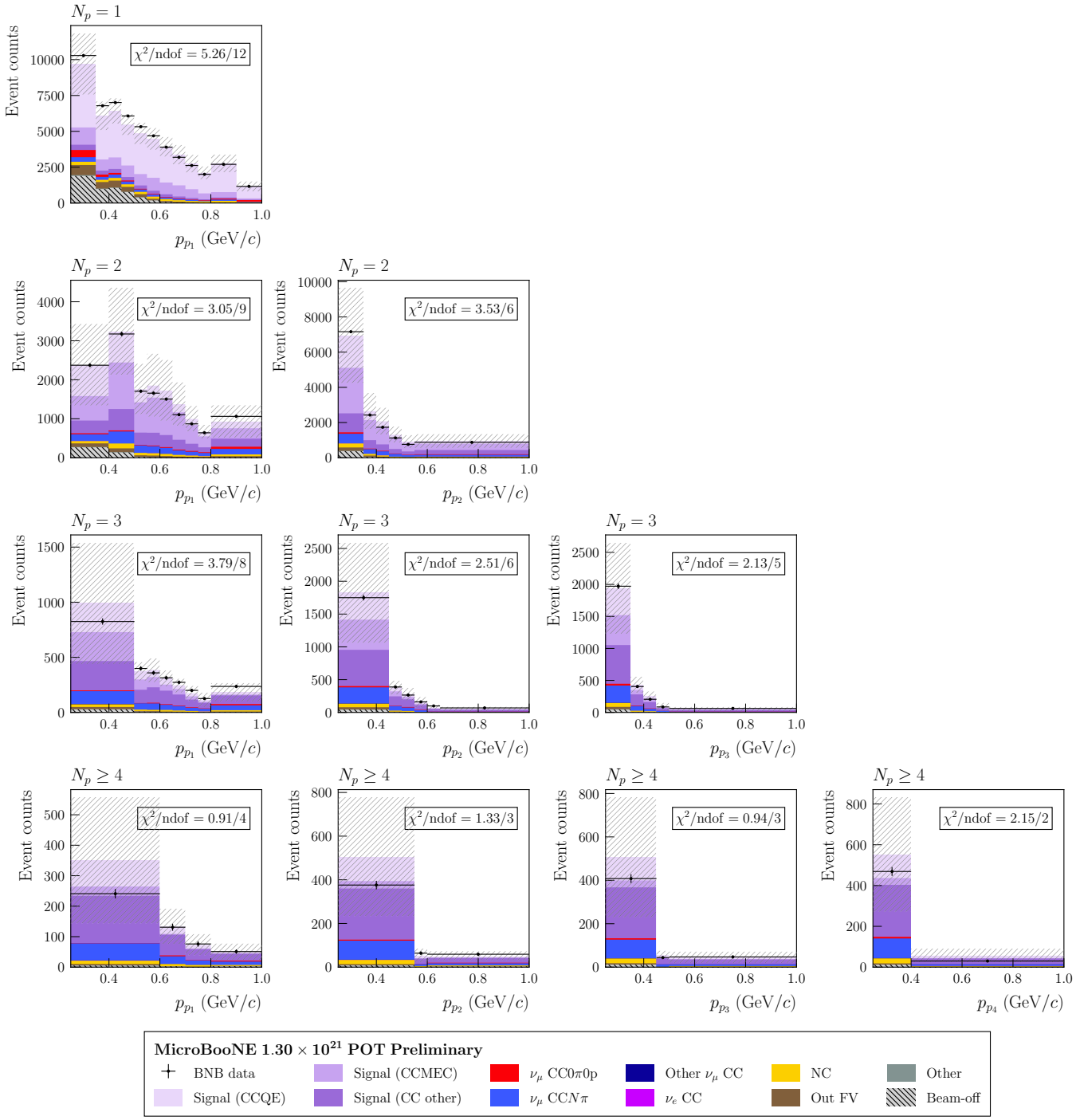

FIG. 36. Reconstructed event rate distributions for blocks 4, 5, 6, and 7, with the signal broken down by interaction mode, corresponding to the double-differential measurements (N_p, p_{p_i}). The total uncertainty on the prediction is indicated by the hatched boxes.

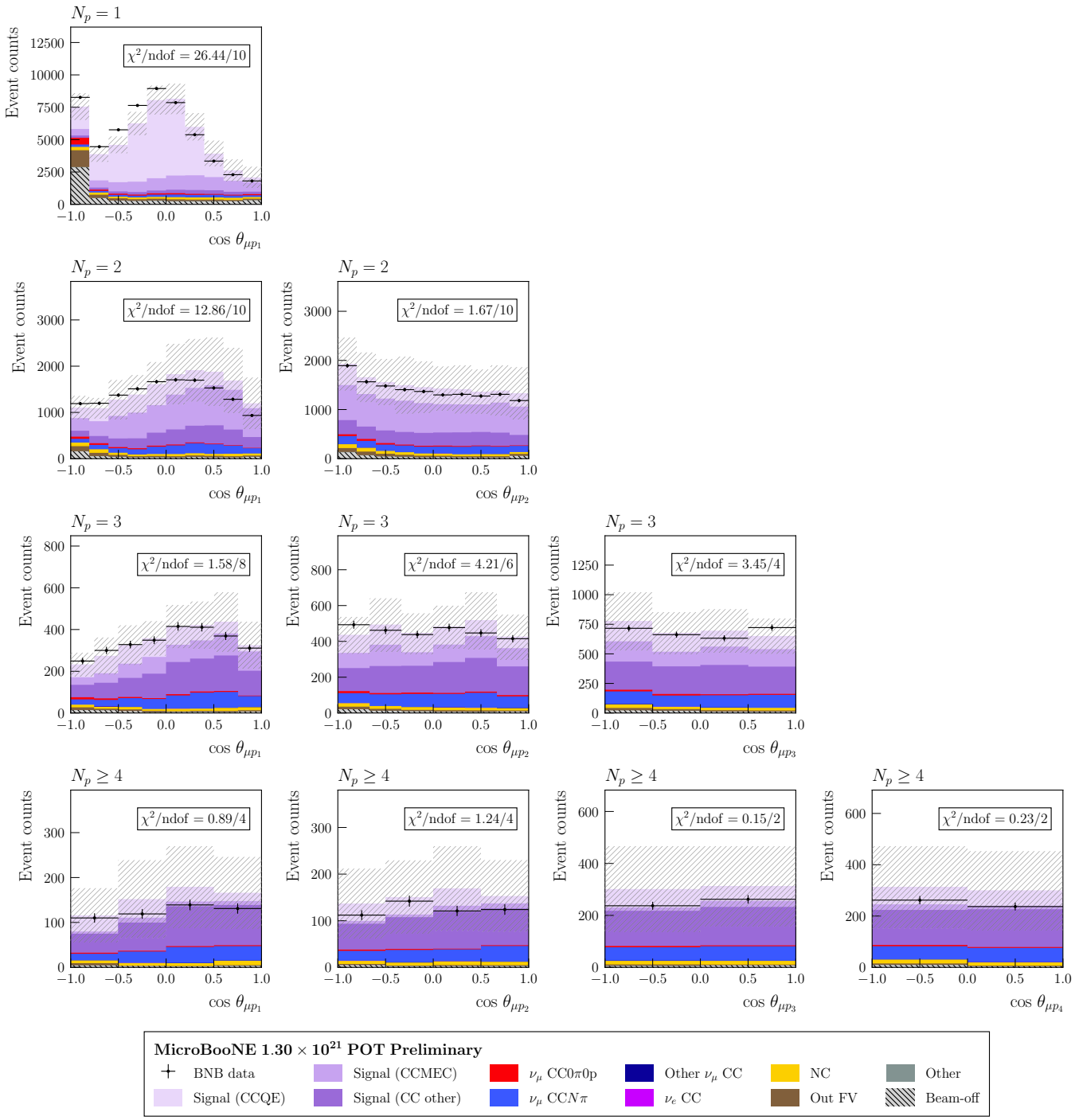

FIG. 37. Reconstructed event rate distributions for blocks 8, 9, 10, and 11, with the signal broken down by interaction mode, corresponding to the double-differential measurements (N_p, $\cos\theta_{\mu p_i}$). The total uncertainty on the prediction is indicated by the hatched boxes.

IV. SIDEBAND EVENT RATE DISTRIBUTIONS

Figures 38 through 42 show the reconstructed event rate distributions for the combined sideband selection described in Sec. IV A of the main text.

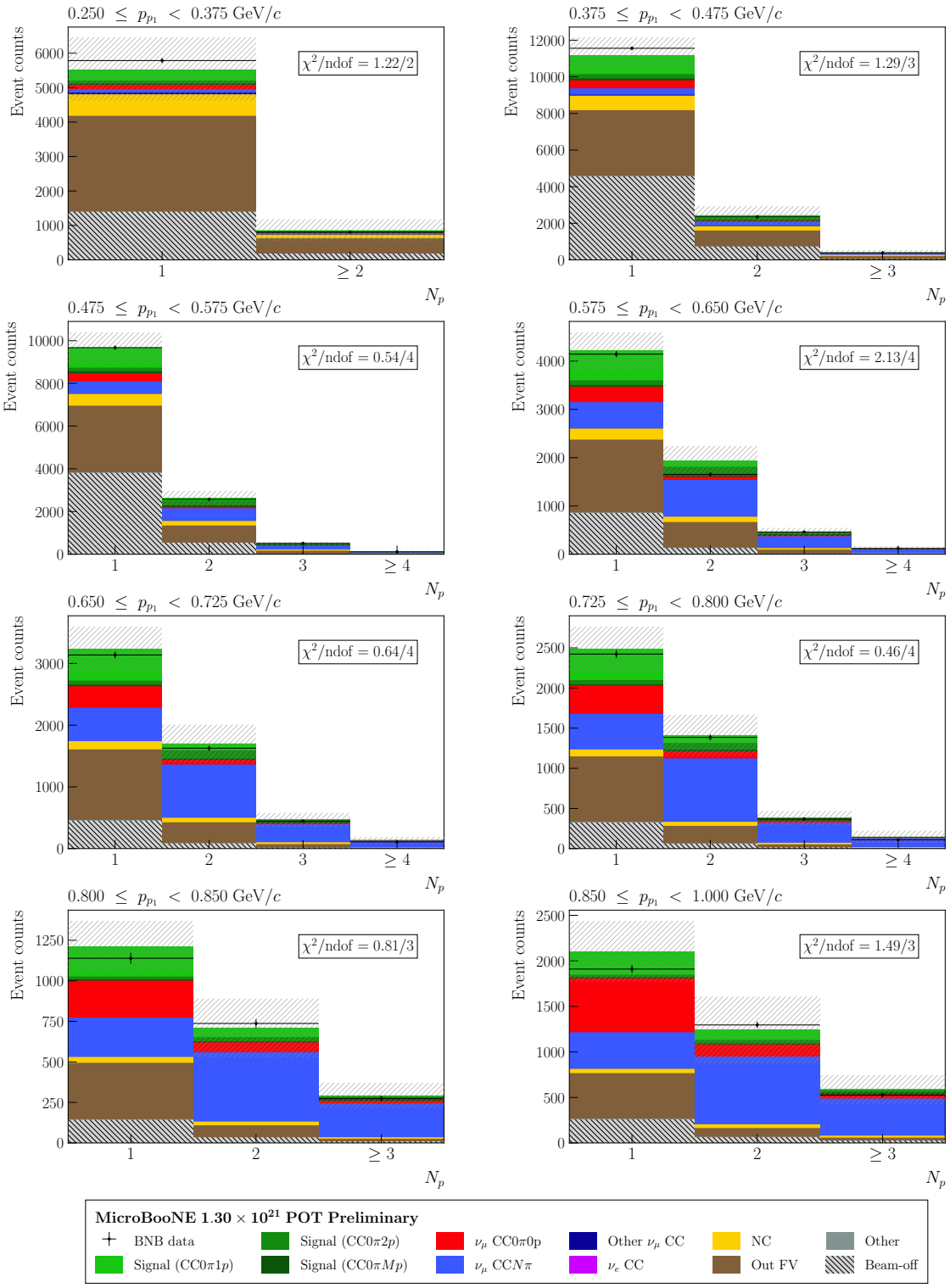

FIG. 38. Reconstructed event rate distributions for block 1, corresponding to the double-differential measurement (p_{p_1}, N_p). The total uncertainty on the prediction is indicated by the hatched boxes.

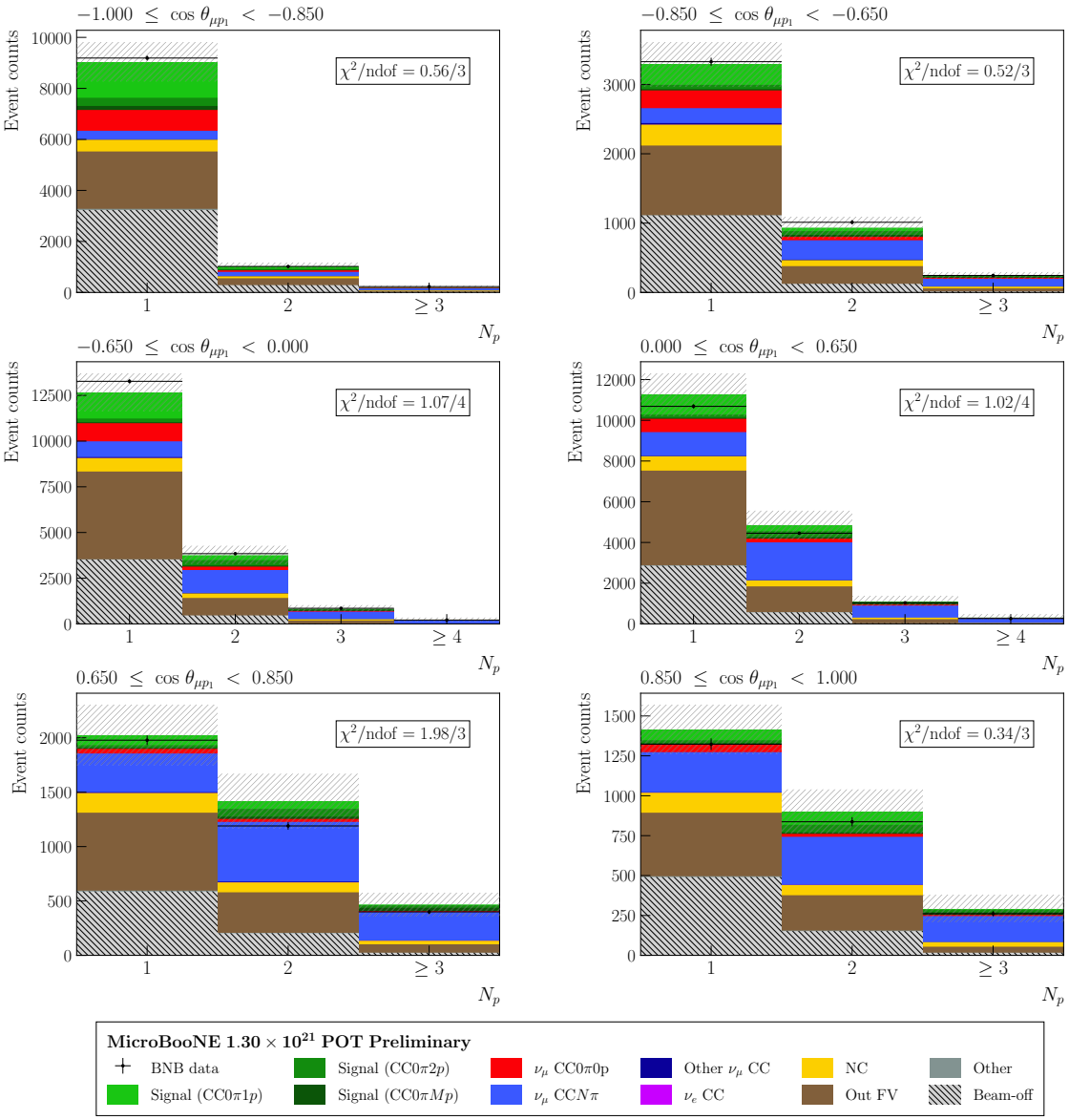

FIG. 39. Reconstructed event rate distributions for block 2, corresponding to the double-differential measurement ($\cos\theta_{\mu p_1}$, N_p). The total uncertainty on the prediction is indicated by the hatched boxes.

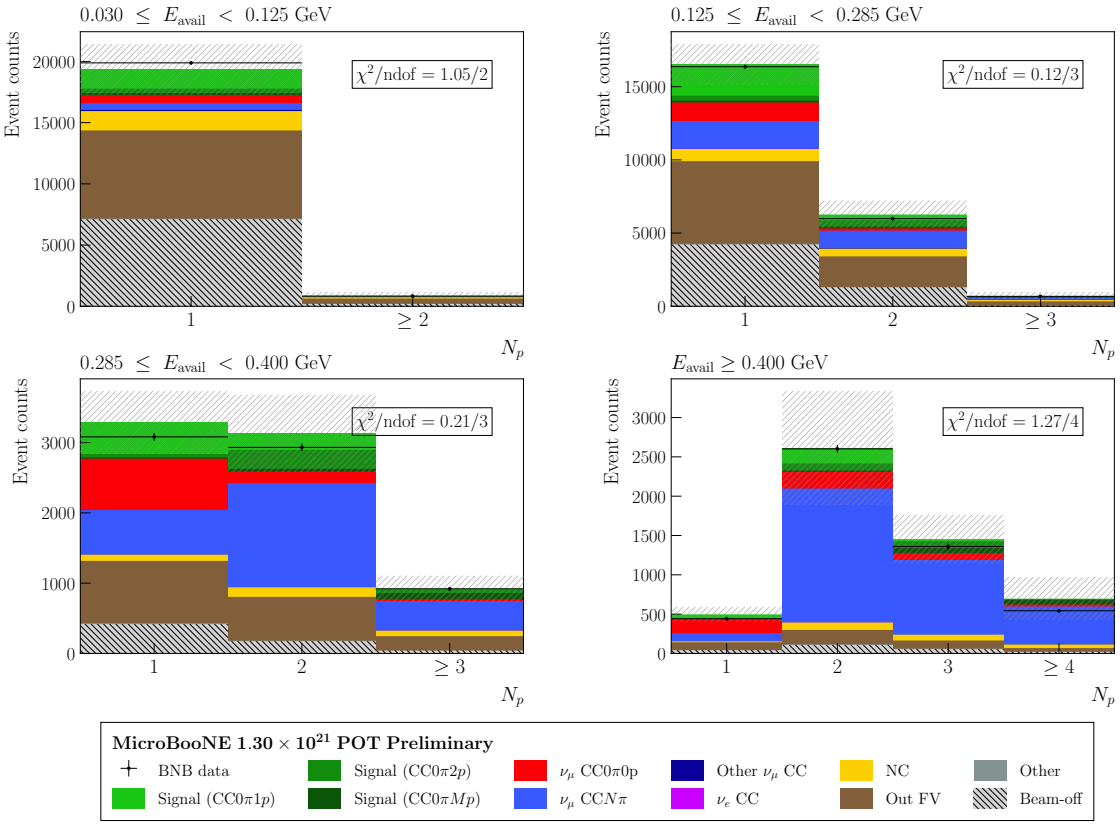

FIG. 40. Reconstructed event rate distributions for block 3, corresponding to the double-differential measurement (E_{avail}, N_p). The total uncertainty on the prediction is indicated by the hatched boxes.

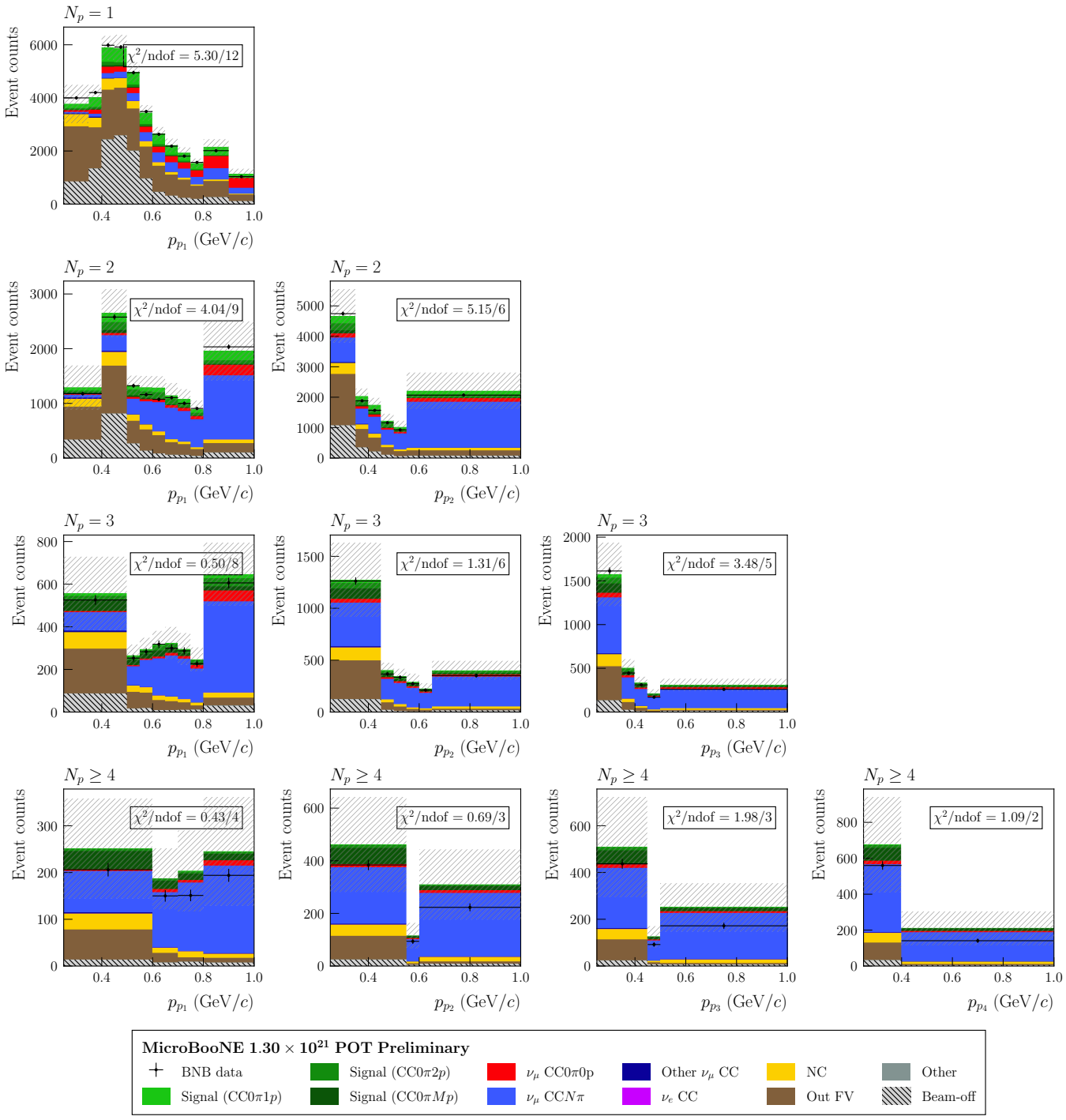

FIG. 41. Reconstructed event rate distributions for blocks 4, 5, 6, and 7, corresponding to the double-differential measurements (N_p, p_{p_i}). The total uncertainty on the prediction is indicated by the hatched boxes.

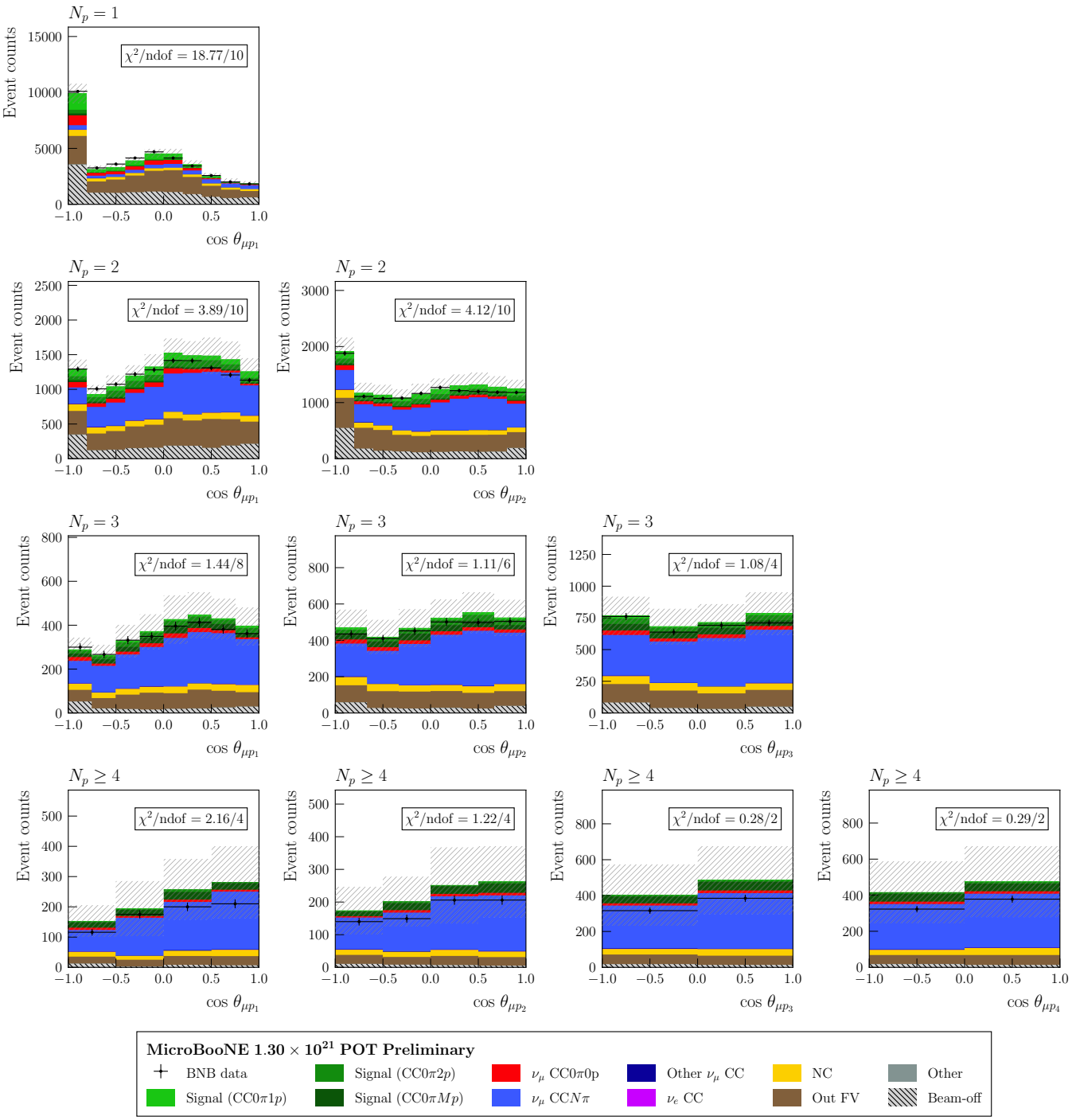

FIG. 42. Reconstructed event rate distributions for blocks 8, 9, 10, and 11, corresponding to the double-differential measurements (N_p, $\cos\theta_{p_i}$). The total uncertainty on the prediction is indicated by the hatched boxes.

V. ADDITIONAL SMEARING MATRIX

Figure 43 shows the additional smearing matrix used to account for regularization bias in the goodness-of-fit comparisons, as described in Sec. III E of the main text. Note that the elements of the additional smearing matrix are dimensionless.

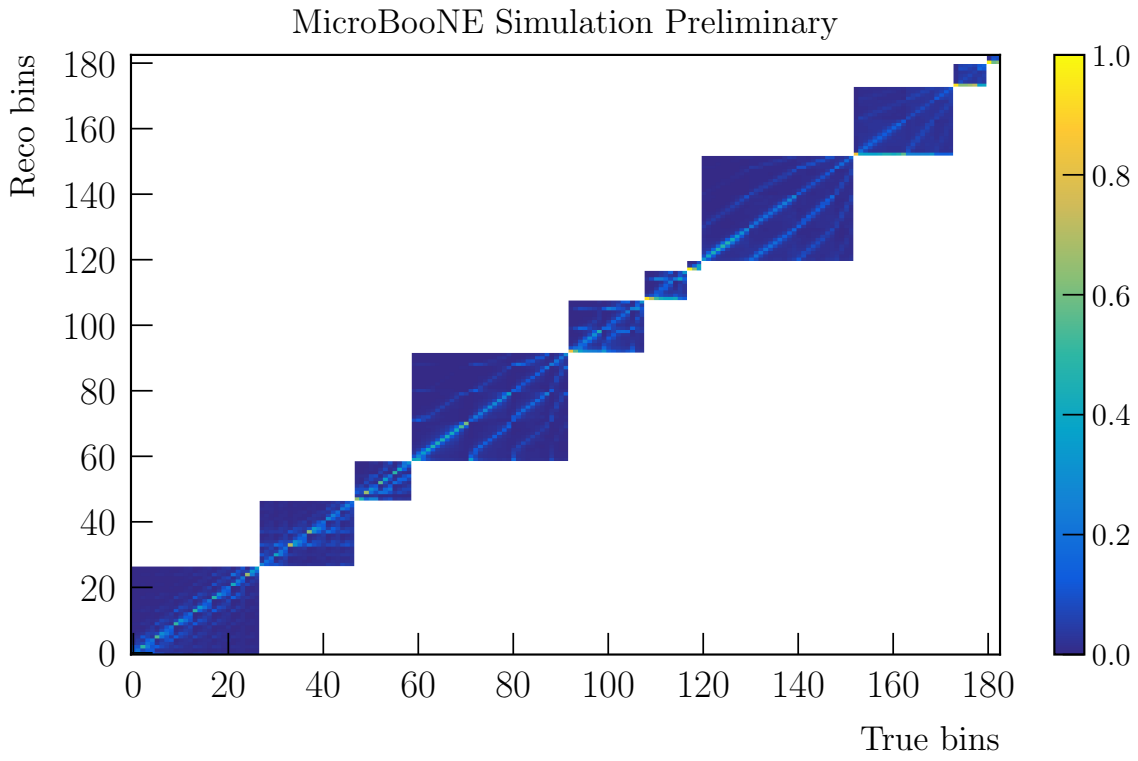

FIG. 43. Additional smearing matrix A_C for each bin block, as defined in Eq. (10) of the main text.

VI. ADDITIONAL GENERATOR COMPARISONS

This section presents comparisons of the unfolded cross section results to additional generator configurations not included in the main text. These configurations are briefly described below.

The untuned GENIE `G18_10a_02_11a` configuration, generated with `v3.6.2`, uses the same underlying physics models as the MicroBooNE tune but without the parameter adjustments [1]. The `02_11a` label denotes a preliminary version of the GENIE nucleon cross-section tune to bubble chamber data [2]. The GENIE `G21_11b_00_000` configuration, generated with `v3.2.0`, replaces the Nieves QE and Valencia 2p2h models with the SuSAv2 model [3] for both QE and MEC interactions. Additionally, the hN intranuclear cascade model is used for the treatment of FSI, instead of the effective hA model.

NuWro `v19.02.2` differs from `v25.11` in several respects. The LFG model is used for all interaction channels including QE, the MEC contribution is described by the original Valencia 2p2h model [4] which provides only inclusive cross sections, and single pion production uses a dedicated $\Delta(1232)$ resonance model [5] with PYTHIA [6] for higher resonances. The intranuclear cascade does not include the convolution scheme used in `v25.11`, but does include effective nucleon density corrections for nucleon-nucleon correlations [7]. NuWro `v25.03.1` shares the same interaction models as `v25.11` but uses the LFG model for all channels, without the spectral function or the QE convolution scheme. An alternative `v25.03.1` sample is produced using the SuSAv2 model [3] for MEC in place of the Valencia 2020 model.

Figures 44 through 48 show the unfolded cross section results compared to these configurations. Table I shows the per-block and global χ^2 values for these generator comparisons.

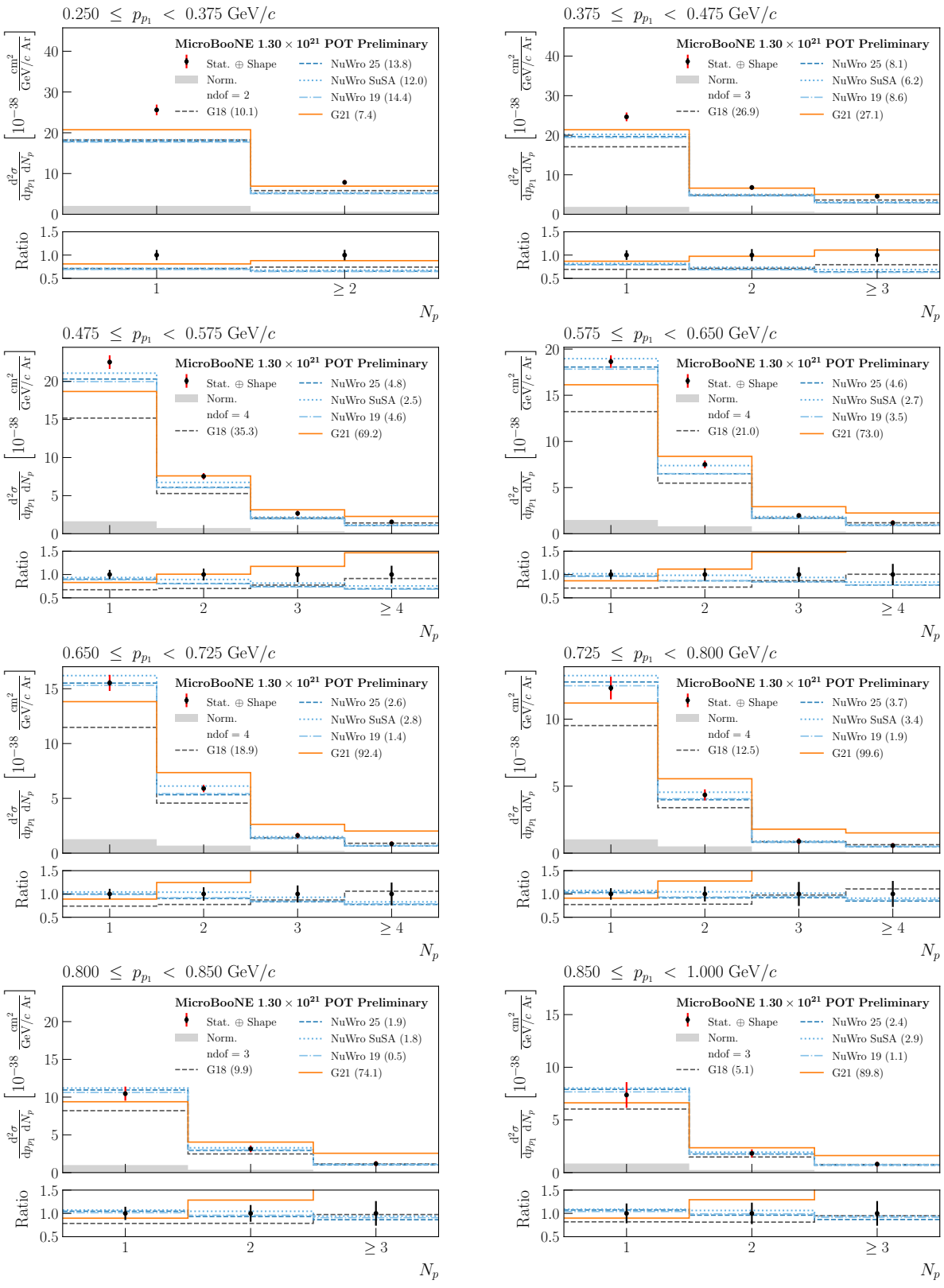

FIG. 44. Flux-integrated double-differential cross sections for block 1 (p_{p_1}, N_p), extracted from the full MicroBooNE BNB dataset (black data points). Error bars indicate statistical and shape-only uncertainties, while the gray band indicates the normalization uncertainty. Predictions from the GENIE `G18_10a_02_11a` and `G21_11b_00_000` tunes, NuWro `v19.02.2`, and NuWro `25.03.1` are overlaid as indicated in the legend. The χ^2 for each prediction is indicated in parentheses. The bottom panels show the ratio of the predictions to the unfolded data.

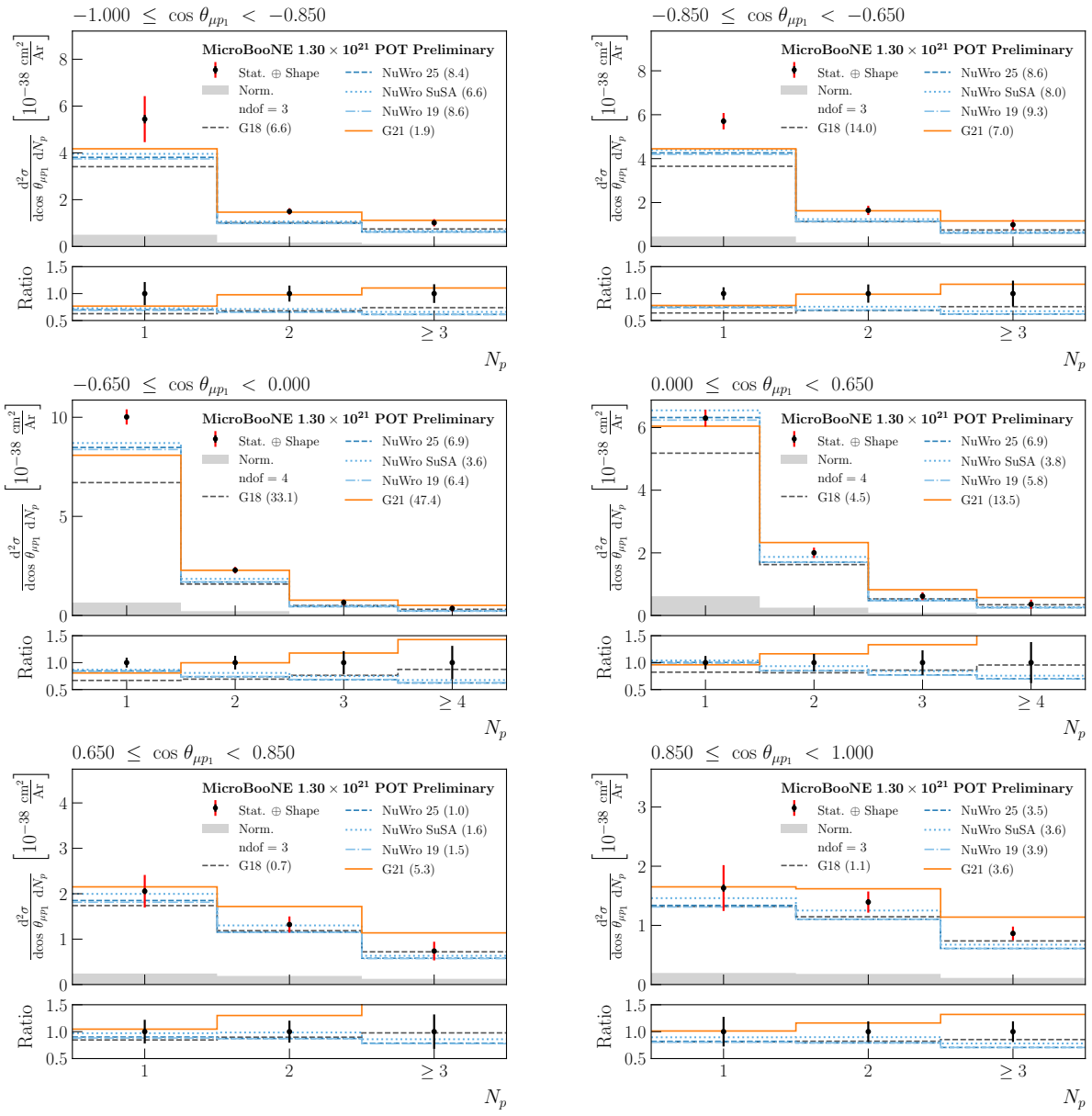

FIG. 45. Flux-integrated double-differential cross sections for block 2 ($\cos\theta_{\mu p_1}$, N_p), extracted from the full MicroBooNE BNB dataset (black data points). Error bars indicate statistical and shape-only uncertainties, while the gray band indicates the normalization uncertainty. Predictions from the GENIE `G18_10a_02_11a` and `G21_11b_00_000` tunes, NuWro `v19.02.2`, and NuWro `25.03.1` are overlaid as indicated in the legend. The χ^2 for each prediction is indicated in parentheses. The bottom panels show the ratio of the predictions to the unfolded data.

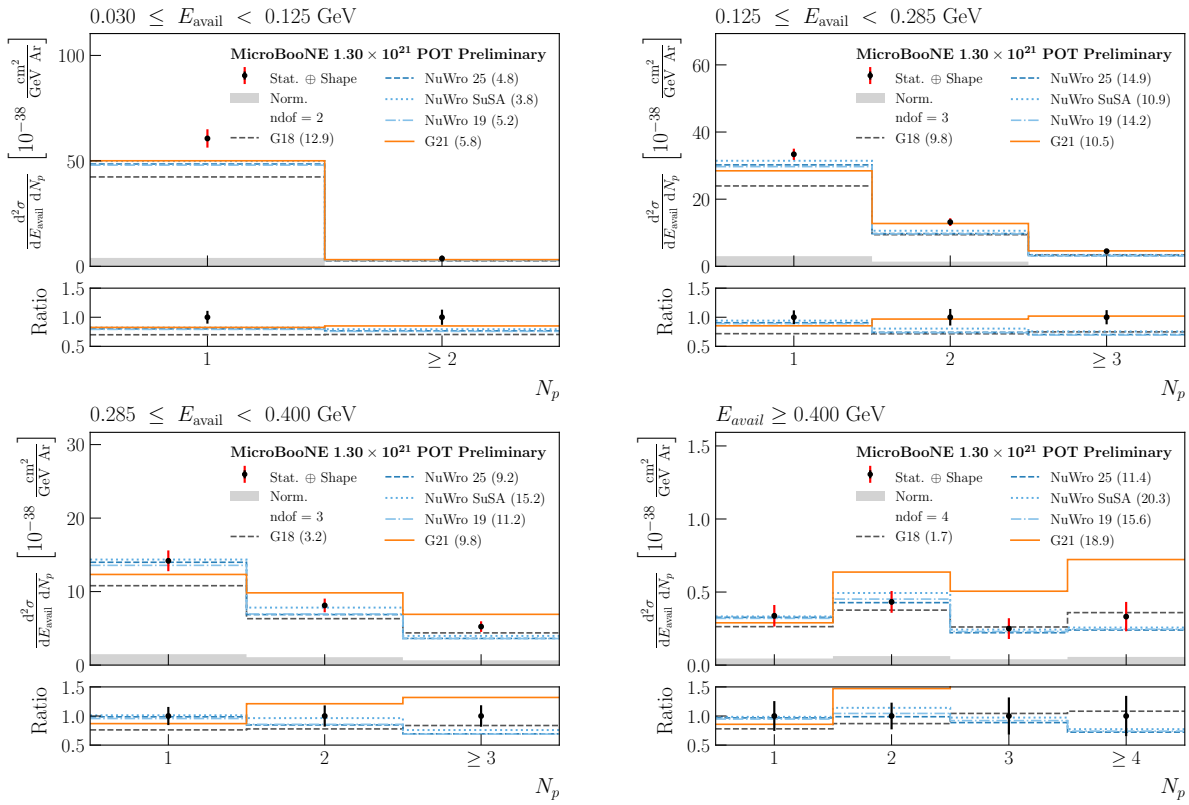

FIG. 46. Flux-integrated double-differential cross sections for block 3 (E_{avail}, N_p), extracted from the full MicroBooNE BNB dataset (black data points). Error bars indicate statistical and shape-only uncertainties, while the gray band indicates the normalization uncertainty. Predictions from the GENIE `G18_10a_02_11a` and `G21_11b_00_000` tunes, NuWro `v19.02.2`, and NuWro `25.03.1` are overlaid as indicated in the legend. The χ^2 for each prediction is indicated in parentheses. The bottom panels show the ratio of the predictions to the unfolded data.

TABLE I. Summary of the χ^2 values obtained for each bin block and globally for the GENIE `G18_10a_02_11a` and `G21_11b_00_000` tunes, NuWro `v19.02.2`, and NuWro `25.03.1` (default and SuSAv2 configurations) predictions compared to the unfolded cross section data.

Block	ndof	`G18_10a_02_11a`	`G21_11b_00_000`	NuWro `v19.02.2`	NuWro `v25.03.1` Default	NuWro `v25.03.1` SuSAv2
1: (p_{p_1}, N_p)	27	100.06	445.93	97.08	98.32	129.68
2: ($\cos\theta_{\mu p_1}$, N_p)	20	98.24	92.08	66.53	70.05	61.96
3: (E_{avail}, N_p)	12	58.09	289.64	48.80	40.69	56.99
4: (N_p, p_{p_1})	33	95.40	484.38	93.63	92.92	129.22
5: (N_p, p_{p_2})	15	52.43	263.94	112.42	95.88	129.72
6: (N_p, p_{p_3})	8	43.78	113.67	65.79	60.05	59.64
7: (N_p, p_{p_4})	2	21.69	36.27	4.57	4.03	2.56
8: (N_p, $\cos\theta_{\mu p_1}$)	32	109.31	105.67	88.90	97.76	83.29
9: (N_p, $\cos\theta_{\mu p_2}$)	20	38.74	93.08	11.42	11.89	9.80
10: (N_p, $\cos\theta_{\mu p_3}$)	6	29.14	40.64	6.27	5.80	4.39
11: (N_p, $\cos\theta_{\mu p_4}$)	2	10.46	6.69	2.71	2.47	1.61
Global	145	516.1	1582.0	828.5	817.7	919.4

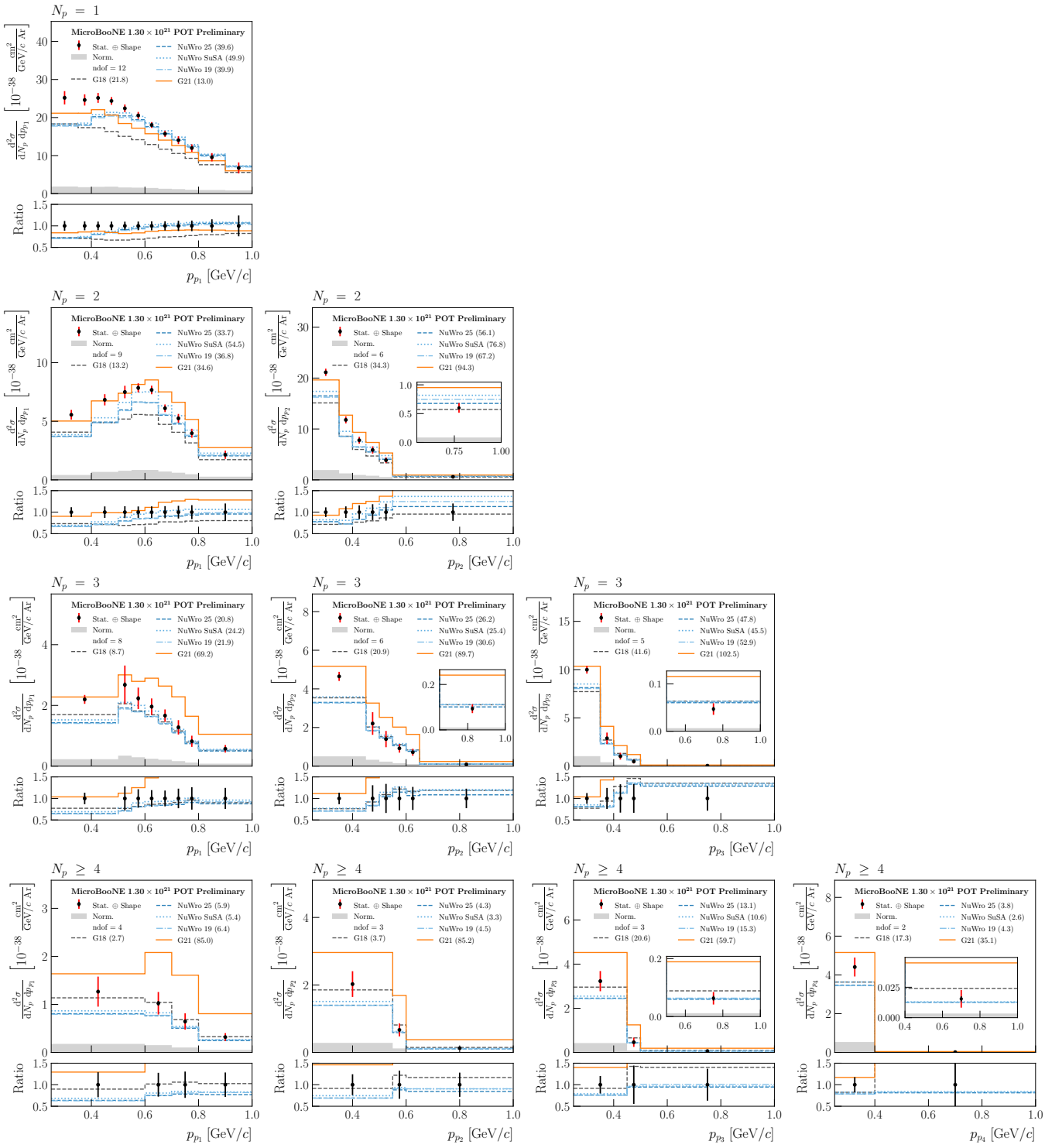

FIG. 47. Flux-integrated double-differential cross sections for blocks 4, 5, 6, and 7 (N_p, p_{p_i}), extracted from the full MicroBooNE BNB dataset (black data points). Error bars indicate statistical and shape-only uncertainties, while the gray band indicates the normalization uncertainty. Predictions from the GENIE `G18_10a_02_11a` and `G21_11b_00_000` tunes, NuWro `v19.02.2`, and NuWro `25.03.1` are overlaid as indicated in the legend. The χ^2 for each prediction is indicated in parentheses. The bottom panels show the ratio of the predictions to the unfolded data.

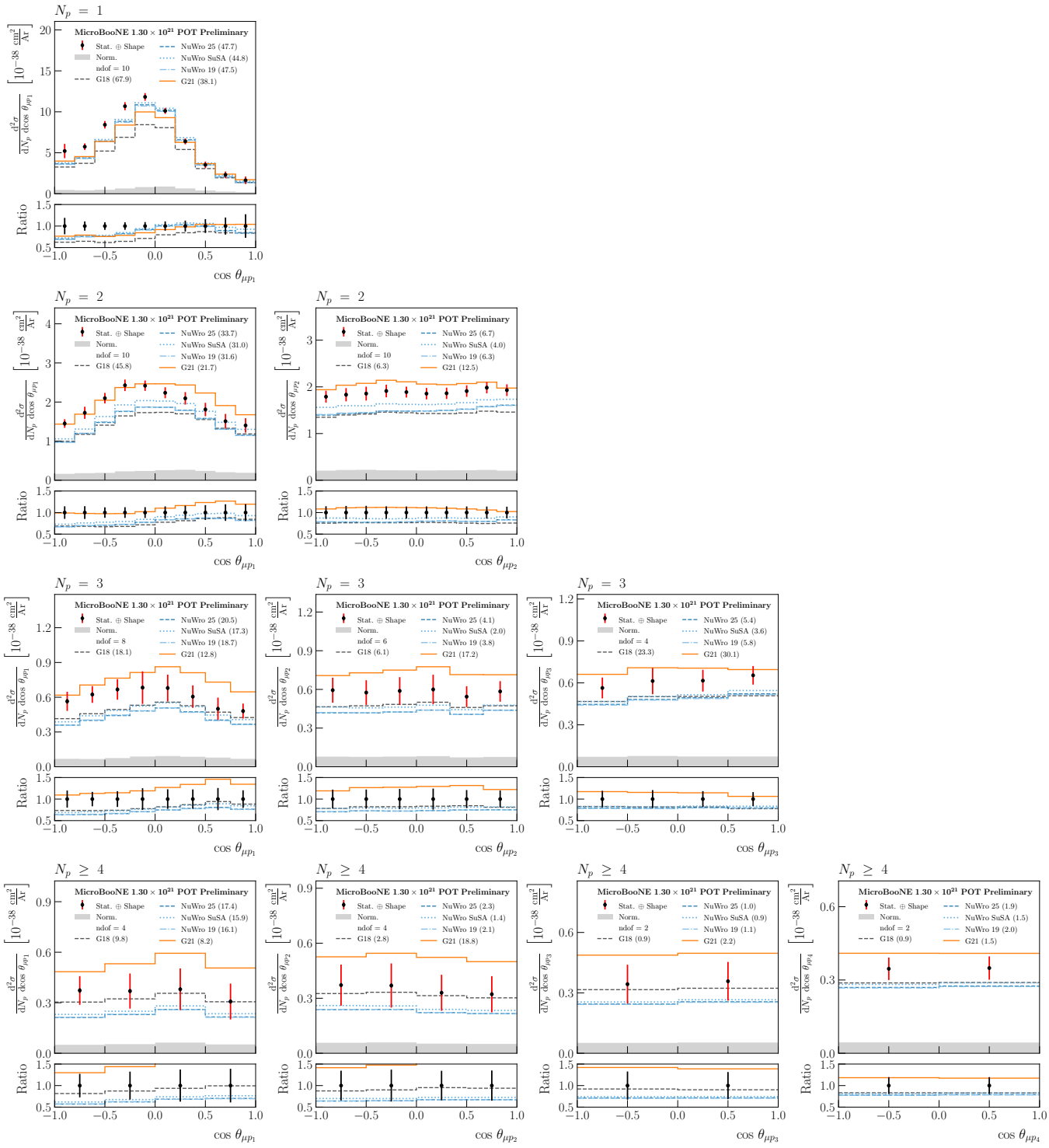

FIG. 48. Flux-integrated double-differential cross sections for blocks 8, 9, 10, and 11 (N_p, $\cos\theta_{\mu p_i}$), extracted from the full MicroBooNE BNB dataset (black data points). Error bars indicate statistical and shape-only uncertainties, while the gray band indicates the normalization uncertainty. Predictions from the GENIE `G18_10a_02_11a` and `G21_11b_00_000` tunes, NuWro `v19.02.2`, and NuWro `25.03.1` are overlaid as indicated in the legend. The χ^2 for each prediction is indicated in parentheses. The bottom panels show the ratio of the predictions to the unfolded data.

VII. UNCERTAINTY BREAKDOWN

Figures 49 through 53 show the fractional uncertainty on the unfolded cross section from each systematic source for all bin blocks in the analysis. The individual contributions shown are described in Sec. III D of the main text.

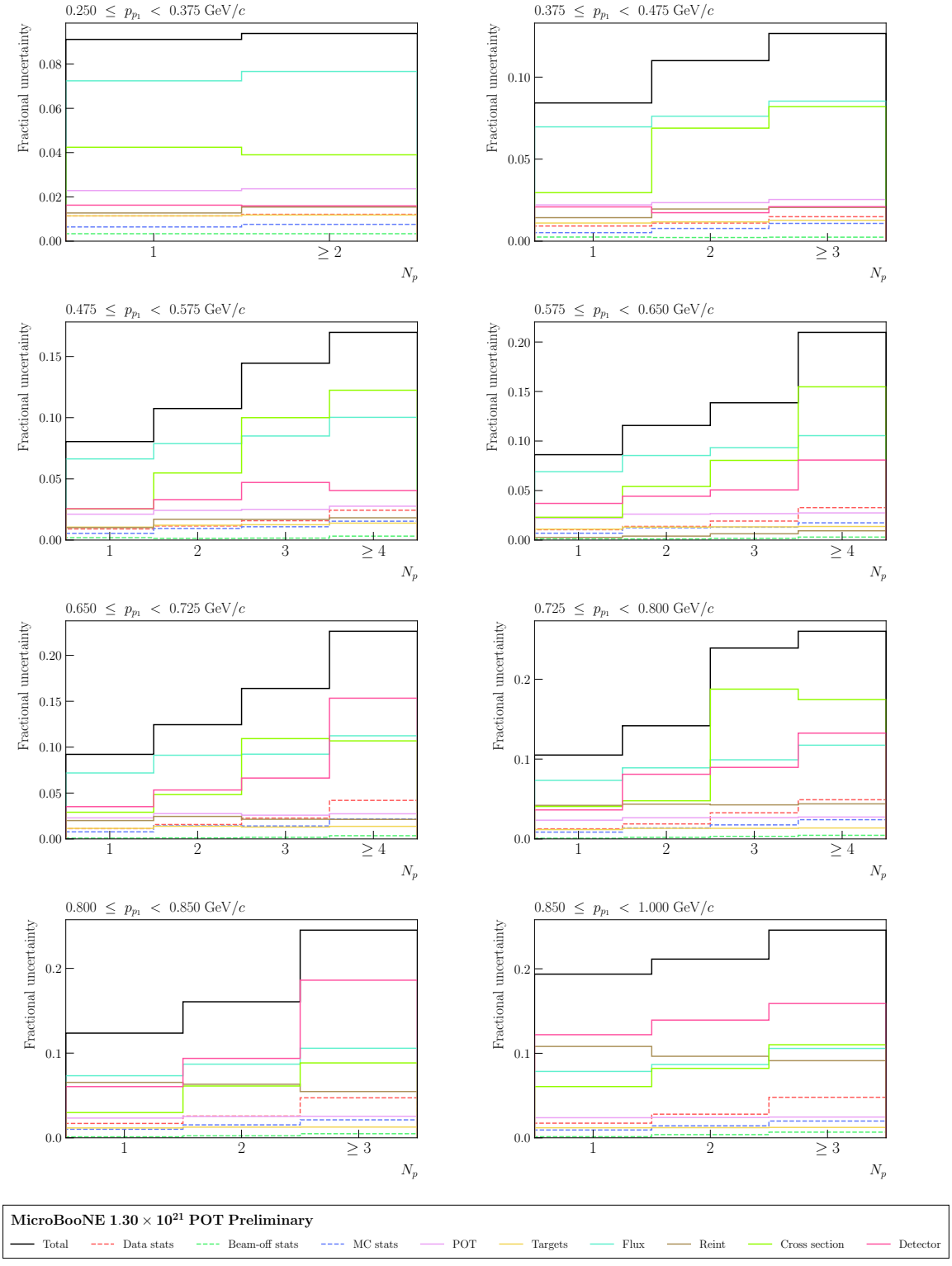

FIG. 49. Fractional uncertainties on the unfolded cross section for block 1, corresponding to the double-differential measurement (p_{p_1}, N_p).

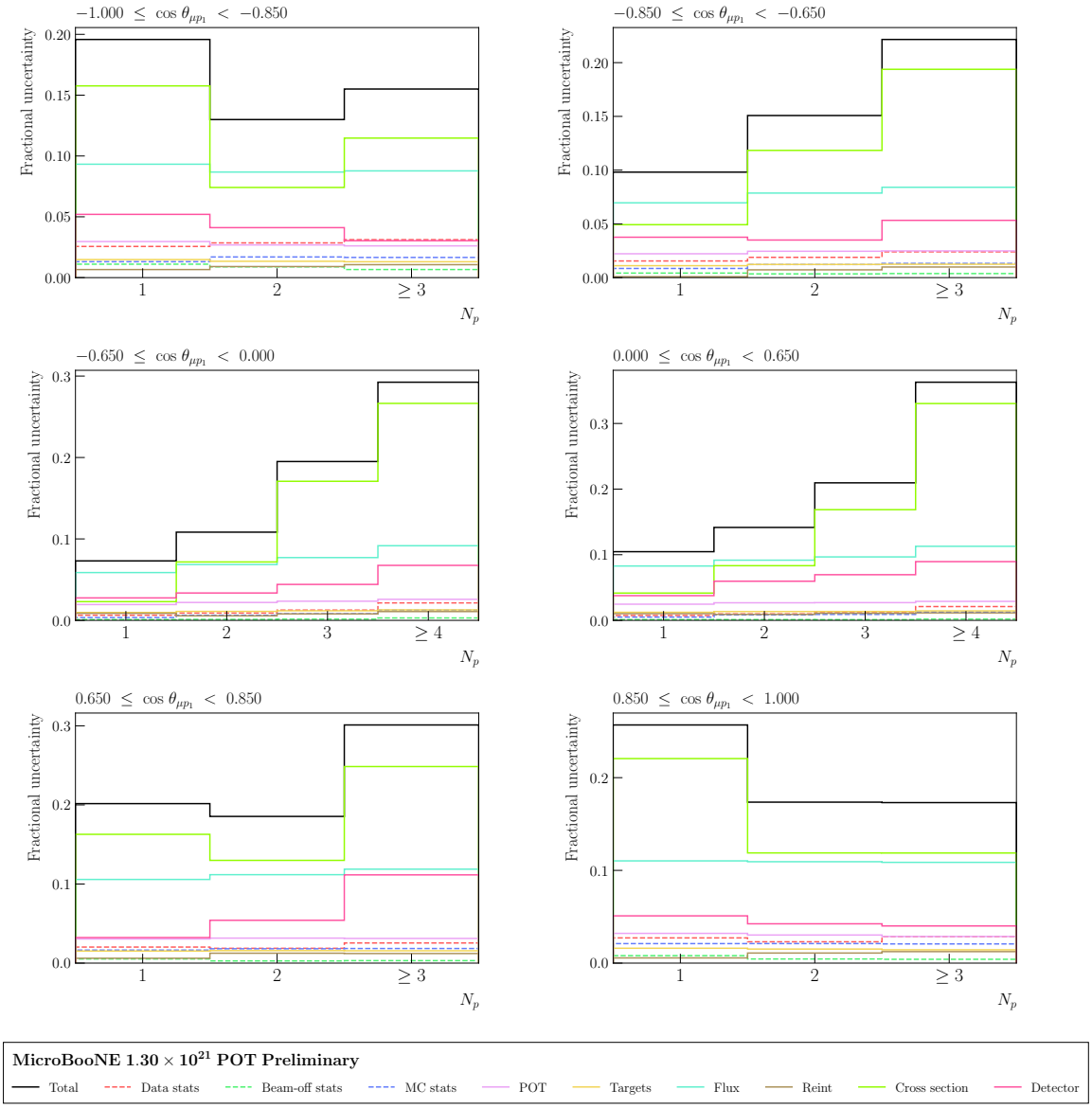

FIG. 50. Fractional uncertainties on the unfolded cross section for block 2, corresponding to the double-differential measurement $(\cos\theta_{\mu p_1},\, N_p)$.

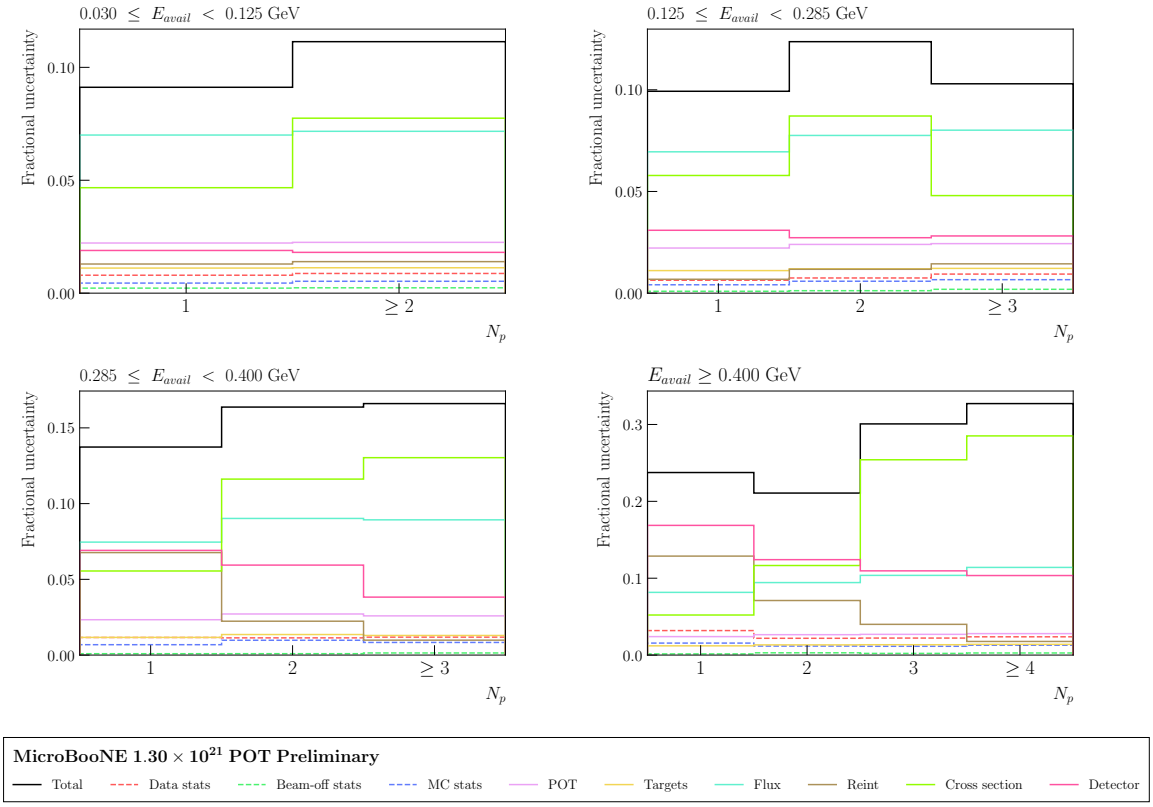

FIG. 51. Fractional uncertainties on the unfolded cross section for block 3, corresponding to the double-differential measurement (E_{avail}, N_p).

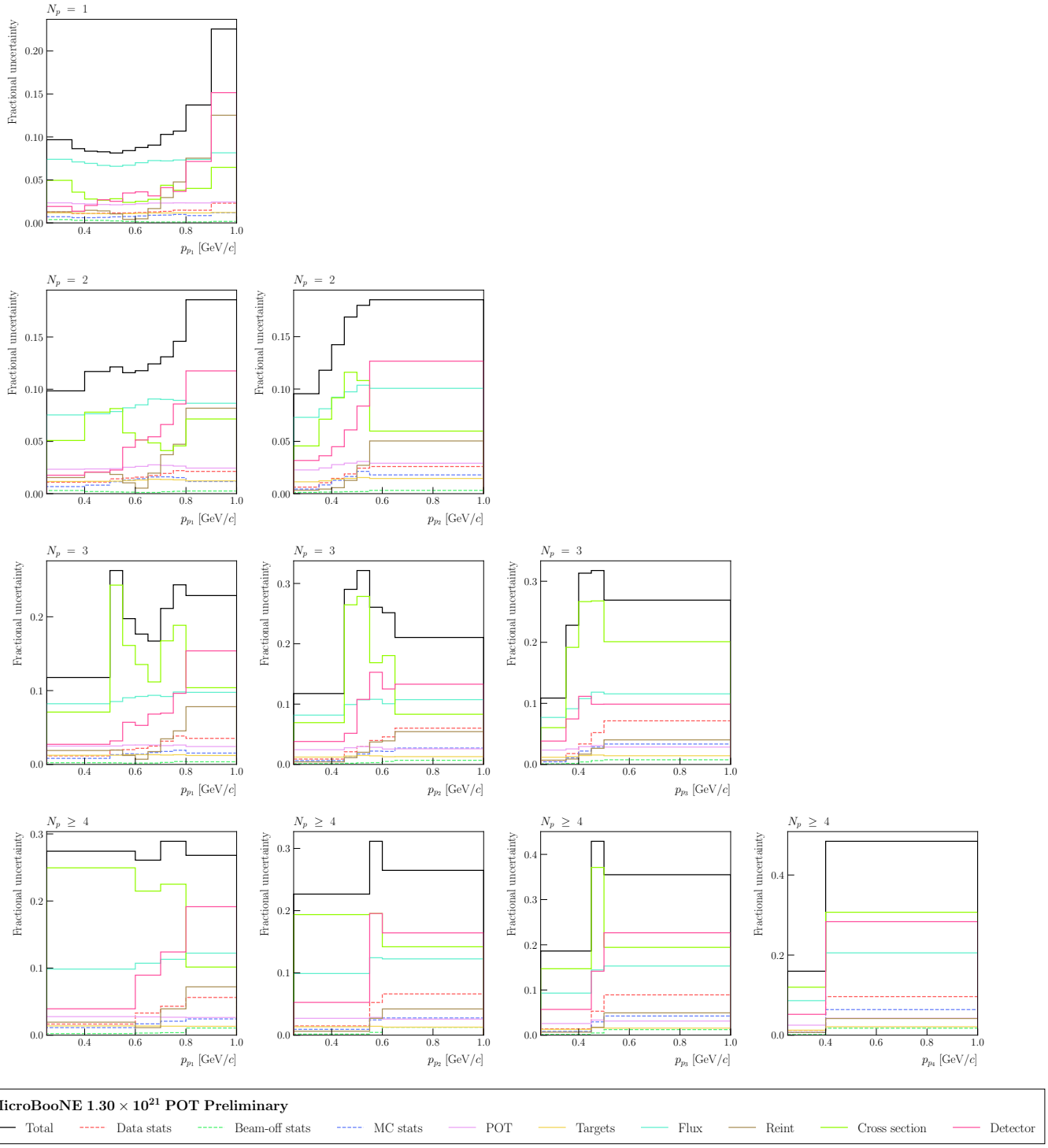

FIG. 52. Fractional uncertainties on the unfolded cross section for blocks 4, 5, 6, and 7, corresponding to the double-differential measurements (N_p, p_{p_i}).

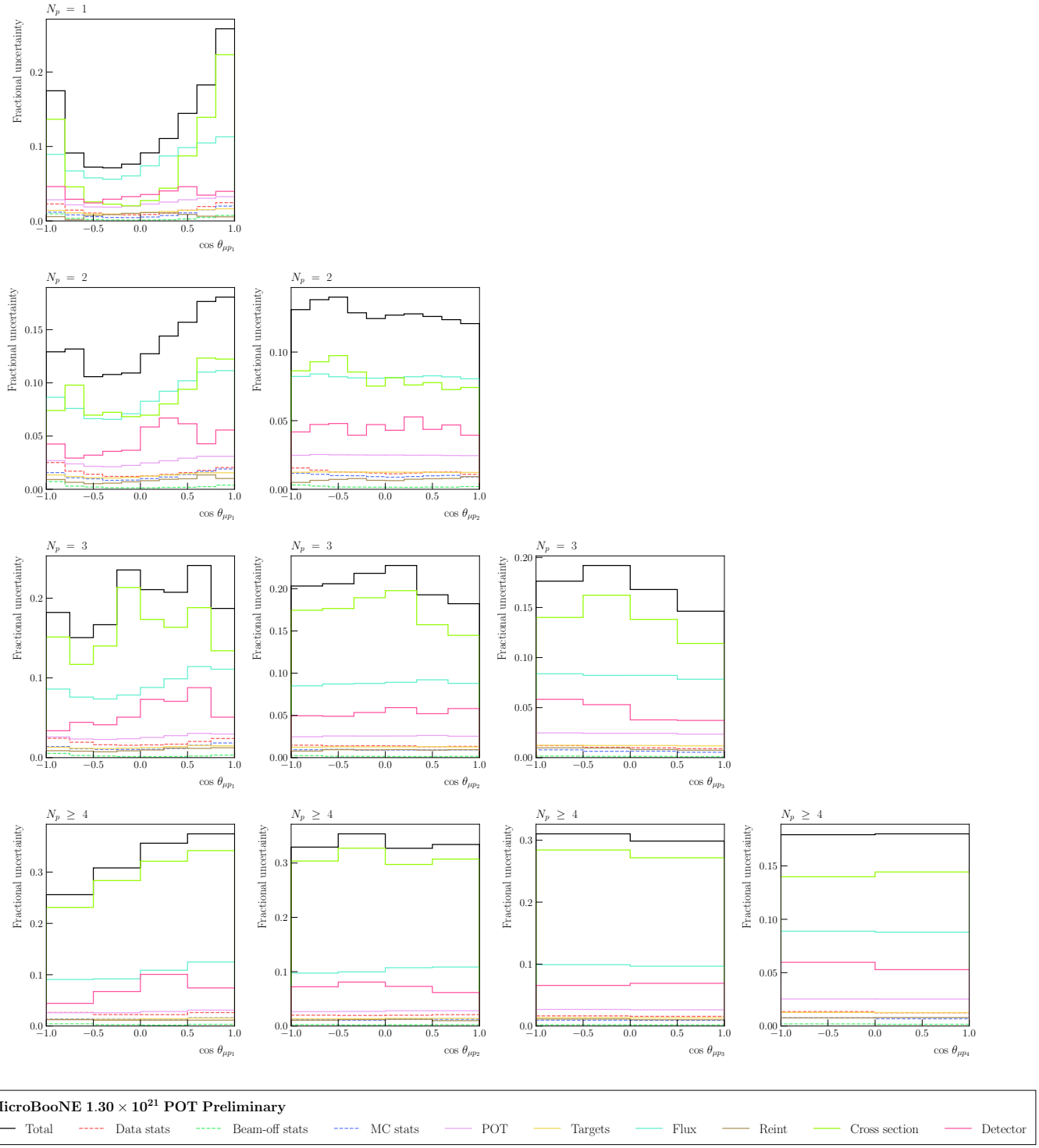

FIG. 53. Fractional uncertainties on the unfolded cross section for blocks 8, 9, 10, and 11, corresponding to the double-differential measurements (N_p, $\cos\theta_{\mu p_i}$).

[1] P. Abratenko *et al.* (MicroBooNE Collaboration), New CC0π GENIE model tune for MicroBooNE, Phys. Rev. D **105**, 072001 (2022), arXiv:2110.14028 [hep-ex].

[2] J. Tena-Vidal *et al.* (GENIE Collaboration), Neutrino-nucleon cross-section model tuning in GENIE v3, Phys. Rev. D **104**, 072009 (2021), arXiv:2104.09179 [hep-ph].

[3] R. Gonzaléz-Jiménez, G. D. Megias, M. B. Barbaro, J. A. Caballero, and T. W. Donnelly, Extensions of Superscaling from Relativistic Mean Field Theory: the SuSAv2 Model, Phys. Rev. C **90**, 035501 (2014), arXiv:1407.8346 [nucl-th].

[4] J. Nieves, I. Ruiz Simo, and M. J. Vicente Vacas, Inclusive Charged–Current Neutrino–Nucleus Reactions, Phys. Rev. C **83**, 045501 (2011), arXiv:1102.2777 [hep-ph].

[5] K. M. Graczyk, D. Kielczewska, P. Przewlocki, and J. T. Sobczyk, C_5^A axial form factor from bubble chamber experiments, Phys. Rev. D **80**, 093001 (2009), arXiv:0908.2175 [hep-ph].

[6] T. Sjostrand, S. Mrenna, and P. Z. Skands, PYTHIA 6.4 Physics and Manual, J. High Energy Phys. **05**, 026 (2006), arXiv:hep-ph/0603175.

[7] K. Niewczas and J. T. Sobczyk, Nuclear Transparency in Monte Carlo Neutrino Event Generators, Phys. Rev. C **100**, 015505 (2019), arXiv:1902.05618 [hep-ex].